Molecular Dynamics Simulations of Biological Molecules on the Natively Oxidized Titanium Surface

Vom Fachbereich Produktionstechnik

der

universität bremen

zur Erlangung des Grades

Doktor-Ingenieur

Genehmigte

Dissertation

von

Dipl. Phys. Julian Schneider

Gutachter:

Prof. Dr.-Ing. Lucio Colombi Ciacchi

Prof. Dr. Tiffany R. Walsh (University of Warwick, UK)

Tag der mündlichen Prüfung: 11.11.2011

Contents

List of Tables

List of Figures

Preface

This dissertation describes the results obtained during my time as a PhD-student from January 2008 until September 2011 at the University of Bremen and the University of Karlsruhe under the supervision of Prof. Lucio Colombi Ciacchi.
Apart from chapter 2 which provides an overview of the current state of knowledge, and chapter 3 which gives a summary of the methods used in the work, the dissertation contains only my own research, if not explicitly stated otherwise.
Parts of this thesis have been published as follows:

Chapter 4:
Julian Schneider and Lucio Colombi Ciacchi, "First principles and classical modeling of the oxidized titanium (0001) surface",
Surf. Sci., **604**, 1105 (2010).

Chapter 5:
Julian Schneider and Lucio Colombi Ciacchi, "A Classical Potential to Model the Adsorption of Biological Molecules on Oxidized Titanium Surface",
J. Chem Theor. Comput., **7**, 473 (2011).

A publication of the results of Chapter 6 is currently in preparation.

Zusammenfassung

Das Ziel dieser Arbeit war, ein Modell einer oxidierten Titan-Oberfläche zur Anwendung in klassischen Molekulardynamik-Simulationen zu erstellen und dieses zur Untersuchung der Adsorption biologischer Molküle zu verwenden.
Neben einer Vielzahl anderer Anwendungsbereiche ist Titan besonders als Biomaterial, z.B. für orthopädische Implantate, von größter Bedeutung. Im Hinblick auf die Verträglichkeit im menschlichen Körper, aber auch in anderen technischen Anwendungen, z.B in Solarzellen oder Sensoren, sind die Eigenschaften der Titan-Oberflächen von atomistischen Prozessen bestimmt. Simulationen zur Untersuchung dieser Mechanismen basieren oft auf idealisierten Modellsystemen, wie perfekten Kristalloberflächen, welche nicht die Komplexität der experimentellen Systeme wiederspiegeln können. Es ist daher wünschenswert, genauere Oberflächenmodelle zu betrachten, um die realistischen Gegebenheiten, wie z.B Rauheit oder chemische Heterogeneität, besser berücksichtigen zu können.

Beginnend mit der Simulation der Oxidation einer Titan(0001)-Oberfläche mithilfe quantenmechanischer Dichtefunktionlatheorie (DFT) wurde ein Strukturmodell einer trockenen, oxidierten Oberfläche erstellt, welches im weiteren Verlauf als Referenz für die Entwicklung eines klassischen Kraftfeldmodells diente. Im nächsten Schritt wurden die Wechselwirkungen zwischen Titanoxid-Oberflächen und Wasser-Molekülen parametrisiert, basierend auf DFT-MD-Simulationen und DFT-Energie-Berechnungen. Das resultierende Modell erwies sich als übertragbar nicht nur auf die oxidierte Oberfläche, sondern, in Kombination mit dem etablierten AMBER-Kraftfeld, auf verschiedene kleine organische Moleküle. Neben der Validierung bezüglich DFT-Energien, wurden auch einige Simulationsergebnisse mit den verfügbaren experimentellen Werten verglichen, z.B. die Immersionswärme und die Adhäsionskraft eines einzelnen Tyrosin-Moleküls aus Atomic-Force-Microscopy (AFM), entnommen aus der Literatur. In beiden Fällen stimmten die Simulationsergebnisse sehr gut mit den Experimenten überein, was die Verlässlichkeit des Modells bestätigte.

Das fertige Modell wurde verwendet, um die spezifische Adsorption des Titaniumbinding-Motifs (minTBP-1), ein Hexapeptid bestehend aus der Sequenz RKLPDA, auf Titan- und Siliziumsubstraten zu untersuchen. Im Vergleich mit Experimenten zeigte sich, dass das entwickelte Modell sowohl makroskopische Größen, wie die Freie Energie

der Adsorption, als auch mikroskopische Größen, wie die Adhäsionskräfte des Moleküls auf der Oberfläche, exakt wiedergeben konnte. Die genaue Analyse der Trajektorien erlaubte es nun, die Adhäsionskrafte direkt mit den zugrundeliegenden atomistischen Mechanismen in Verbindung zu bringen und insbesondere die individuelle Rolle der beteiligten Residuen zu untersuchen. Als Vergleichs dienten hier Simulationen auf einer oxidierte Silizium-Oberfläche, auf welcher das Molekül mit etwas geringeren Kräften haftete. Bemerkenswert in diesem Zusammenhang war, dass die maximalen Adhäsionskräfte auf beiden Substraten durch die positiv geladenen Arginin und Lysin Residuen hervorgerufen wurden. Dieser Aspekt spricht gegen eine selektive Adsorption verschiedener Aminosäuren als Ursache für das spezifische Verhalten. Die Simulationen rücken vielmehr ein komplexes Wechselspiel zwischen adsorbierten Residuen und der lokalen Wasserstruktur über der Oberfläche in den Mittelpunkt. Hydrophile Endgruppen können sich dabei in lokalisierten Wasserdichte-Maxima verankern, was insbesondere auf Titan stark zum tragen kommt, während sich hydrophobe Teile der Seitenketten um diese Maxima herum in Regionen mit geringer Wasserdichte anordnen.

Um die Anwendbarkeit des Modells über biologische Systeme hinaus zu demonstrieren, wurden zudem die Kohäsionskräfte zwischen Titandioxid-Nanopartikeln simuliert. Die resultierenden maximalen Kräfte lagen zwischen 2 und 6 nN, je nach Wasserbedeckung der Oberfläche, in guter Übereinstimmung mit experimentell gemessenen Kräften für die Kohäsion innerhalb eines Films aus Nanopartikel-Agglomeraten (3 nN). Diese Ergebnis lässt darauf schließen, dass es sich bei den gemessenen Kräften tatsächlich um das Brechen einzelner Partikel-Partikel-Kontakte handelt.

Chapter 1

Introduction

The outstanding mechanical and chemical properties of titanium have attracted the attention of materials scientists for decades, leading to the development of Ti-based alloys for a broad range of applications. Beside its wide use in the aerospace and marine industries, its corrosion resistance and biocompatibility make titanium a material of choice for medical and dental implants. In this case, a thorough knowledge of the physical and chemical details of the interface between the implant and the physiological environment is desired for tailoring the surface properties and optimizing the adhesion of cells within the body tissues.

Since these processes are governed in a fundamental way by the adsorption of biological macromolecules, an atomic-scale understanding of the interaction between proteins and the metal surface is often sought, yet still lacking. Complementary to experiments, atomistic molecular dynamics (MD) simulations, based on either quantum mechanical or classical formalisms, may provide a powerful method to gain insight into the microscopic mechanisms involved in protein adhesion. However, realistic simulations of the interface between titanium and a physiological environment have to face the rich chemical complexity of the system. In contact with water and oxygen, the metallic Ti surface is covered by an oxide layer whose composition, structure and thickness strongly depends on the oxidation conditions. Thin oxide layers for example which form at room temperature, exhibit an amorphous structure and a broad spectrum of stoichiometric compositions.

Although providing valuable generic understanding of the atomistic mechanisms, the widely used approach of considering perfect TiO_2 crystal surfaces as idealized model substrates might in the end not be capable to capture all aspects of the adsorption behavior.

This sets the need for more realistic models.
Hence, the central topic of this thesis is the development of a realistic surface model by atomistic simulations and its application to biomolecular adsorption. This challenge inherently comprises multiple length and time scales: The elementary oxidation reactions at the bare metal surface crucially require to take into account the quantum mechanical details of the electronic wavefunctions which drastically limits the time and length scale of the model. On the contrary, when modeling biomolecular adsorption the mere size of the molecule demands large length scales. In addition, the increased number of internal degrees of freedom due to the flexibility of the molecule moves the emphasis from purely energetic aspects towards statistical mechanics, or, in terms of thermodynamics, from potential energies towards free energies which generally requires long simulation times. Both points of view can hardly be combined in a unified model, thus a hierarchical approach has been chosen in this work.
In detail, I have created a structural model of the charged, natively oxidized titanium surface based on quantum mechanical calculations, for which a novel empirical force field has been developed. This interaction model enables the simulation of the adsorption of large molecules in very good agreement with experiments and ab initio calculations. Using advanced simulation methods, in particular state-of-the-art sampling techniques which have been combined in a novel way, the specificity of titanium binding peptides has been investigated on a realistic system for the first time by quantifying the involved adhesion mechanisms. Additionally, as an example beyond biotechnological applications, the potential is used to simulate the contact forces between titania nanoparticles and their agglomerates.

The dissertation is structured as follows:
In chapter 2 the current knowledge regarding biomaterials, in particular the properties of the oxidized titanium surface and the adsoprtion behaviour of peptides and proteins on Ti is summarized. Chapter 3 provides an overview of the simulation methods used in this work. In chapter 4 the development of the structural and interaction model for the dry oxidized titanium surface is explained and the generation of a large scale oxidized surface by purely classical methods is presented as an first application. Chapter 5 introduces the interaction of the oxidized surface with water, investigated at first by ab initio molecular dynamics simulations and then extended to the classical force field. The resulting potential model is tested for small organic molecules against DFT and experimental

results and its applicability to biologically relevant systems, such as the RGD peptide is demonstrated. In chapter 6 I investigate the adsorption of the titanium binding motif, the RKLPDA peptide, and compare the adhesion forces, the free energy and the microscopic mechanisms on titanium and on the oxidized silicon surface. As an application from a different field of engineering, chapter 7 presents simulations of the contact forces among TiO_2 nanoparticles and their agglomerates compared to experimental atomic force microscopy results. Finally, in chapter 8 all results are summarized and an outlook towards future work is given.

Chapter 2

Solid Surfaces in Physiological Environment

Progress in medicine in the last decades has been facilitated to a great extent by the introduction of medical implants which replace parts of the human skeleton and teeth, prevent blood vessels from being plugged, or, such as pacemakers, support the body in its vital functions, to name just a few. The success of this technique is coupled to the continuous improvement of both the surgical methods and the properties of the employed implant materials and devices. The basis of this improvement is a growing understanding of the behavior of these biomaterials within a living organism which is due to the concerted effort of engineers, biologists, chemists and physicists. The ambitious goal is to combine enhanced cell and bone adhesion and growth at the implant surface with controlled antibacterial properties to prevent infections, while at the same time retaining the mechanical properties of the material itself. An equally important prerequisite is that no toxic substances are released into the body by dissolution of the material or its coating. The aggressive environment, i.e. the exposure to oxygen, water, ions and all kinds of small and large organic molecules combined with mechanical load provide additional challenges which have to be taken into account. All of these requirements have put titanium, i.e. commercially pure (cp) Ti or titanium based alloys, e.g. Ti6Al4V or TiNi, into the focus of biomaterials engineering, as this metal fulfills most of the criteria already in its native state.

Engineering of biomaterials is by far not the only field which depends in a crucial way on the interfacial properties between solid surfaces and a wet or physiological environment. Considering for example pharmaceutical applications, the use of nanoparticles

as drug carriers has emerged as a promising technique. On the contrary, it is desirable to prevent adhesion of drug molecules onto container walls while storing them, as these effects can reduce their concentration or even alter their functionality in an uncontrolled way. Furthermore, surface recognition exploiting the specific adhesion behavior of specially tailored peptides has become a field of highest interest, as it provides promising new techniques in controlling biomineralization and bionanotechnology. Even the cohesion forces between agglomerates of nanoparticles which can be used as catalysts, gas sensing films or reinforcement in composite materials, are mediated to a great extend by the water layer which forms at the surface under atmospheric conditions.

Fig. 2.1 provides a schematic overview of the complex picture and processes involved at a metal surface in physiological environment. The key aspects are:

- The superficial oxide layer that passivates the surface and governs the interactions with its environment.
- The reactivity towards water, defining the degree of hydroxylation as well as the surface charge and electrostatic potential.
- The adsorption and immobilization of molecules like peptides and proteins.

The individual role of these points shall be explained briefly in the following sections.

2.1 Oxidation of Titanium

The corrosion resistance of metallic Ti [168], its electrical behavior as an electrode material [120] and its biocompatibility in medical implants [74, 9] are governed by the structure and composition of the passivating oxide layer which spontaneously grows on its surface. The oxidation of metallic surfaces in general has been investigated both experimentally and theoretically. Theoretical approaches exist to describe the kinetics of oxide growth under various conditions. For thick oxide layers of about 0.5-1 μm width which are known to form at high temperatures, the diffusion of atoms and electrons through the oxide region is the rate determining process. Based on this assumption, the Wagner theory [185] describes oxide growth at high temperature as an activated process with a parabolic growth $L(t) \sim \sqrt{\kappa t}$. The formation of ultrathin superficial layers which is the dominant channel

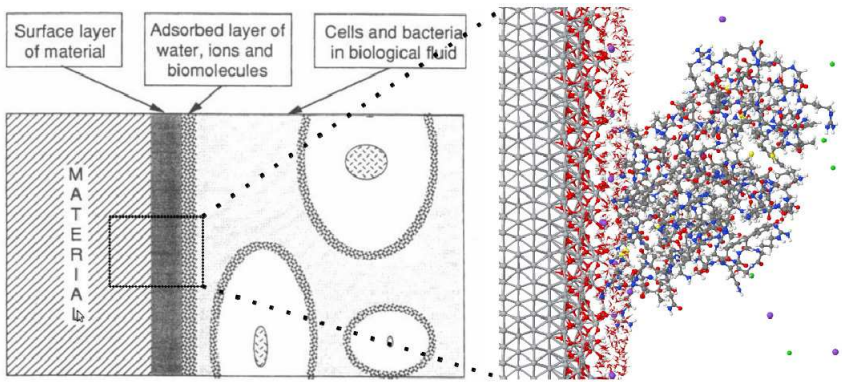

Figure 2.1: Schematic picture of a metal surface in a physiological environment ((*left*), taken from Ref. [91]). Zoom into the atomistic structure of an adsorbed biomolecule, in this case a lysozyme protein, on the oxidized titanium surface from our simulations (*right*). For clarity only surface water molecules are displayed.

at low temperatures, takes place in a different way, though, as the initial stage of oxygen chemisorption is associated with very small or even zero activation barrier. A description of the growth of thin films is given for instance by the Cabrera-Mott model [31], assuming the presence of a strong electric field due to the electron transfer, a non-equilibrium reaction at the metal/oxide interface, and the transport of metal cations into the oxide phase being the rate determining process. The Cabrera-Mott model predicts that below a critical temperature the oxide growth asymptotically reaches a limiting thickness whereas for higher temperatures film extends infinitely. However, as atomistic mechanisms play an important role in particular in the initial stage, this continuum based model must be assigned a rather qualitative than quantitative character.

Such microscopic insights in oxidation processes can be provided by quantum mechanical simulations of the chemisorption of oxygen molecules at metal or semiconductor surfaces, proposing a so-called *hot-atom* dissociation [43, 44, 41]. As depicted in Fig. 2.2, electron donation into the partially filled anti-bonding π^* orbital of the oxygen molecule effects a Pauli repulsion of these molecular orbitals, and a sudden separation of both oxygen atoms associated with a release of high kinetic energy.

Considering the titanium surface in particular, it is known from experiments that thin oxide layers on Ti exhibit a rather amorphous structure and a broad spectrum of stoichiometric compositions [135, 167, 28, 115, 10, 181]. The reactions of molecular oxygen

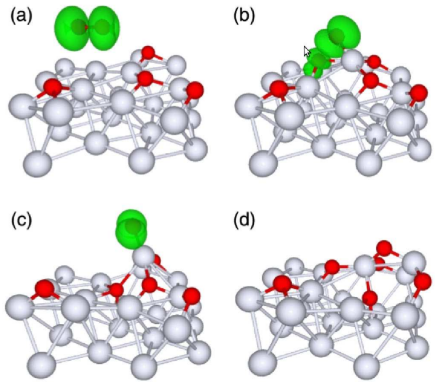

Figure 2.2: Snapshots of the initial stages of the oxidation reaction at the aluminum surface. The spin density is depicted by the green isosurface. (Taken from Ref. [43])

with Ti surfaces have been investigated extensively in the last decades by means of X-ray photoelectron spectroscopy (XPS), Auger electron spectroscopy (AES), direct recoil spectrometry (DRS) and electron diffraction methods like RHEED and LEED. Electron spectroscopic methods generally reveal the appearance of a wide range of Ti oxidation states (from Ti_2O to TiO_2) and indicate that oxidation processes go through various stages at different temperatures [10, 135, 28, 167, 166]. Recent studies suggest that at low temperature the initial oxidation reaction yields predominantly lower oxides like Ti_2O and TiO which become further oxidized to TiO_2 upon increasing exposure to oxygen [167]. Based on DRS and RHEED experiments as well as on work function measurements, it is agreed that oxygen molecules adsorb above the surface layer at low temperatures [167, 3], while O atoms can diffuse underneath the surface layers at elevated temperatures, retaining a top layer of metal atoms [181, 166, 22].

Besides these experimental observations, very few ab initio studies of the oxidation of Ti surfaces have been reported, yet, they are limited to static energetic analysis of O atoms adsorbed in different surface and subsurface sites [115]. In contrast, the properties of TiO_2 crystals and surfaces have been investigated widely both via quantum mechanical [4, 184, 36, 102] and classical simulations. The development and application of classical potentials for titanium oxide have diverged in two main directions. On the one hand rather simple force fields employing fixed point charges and two-body potentials are commonly employed. A widely used potential form in this context is the one proposed by Matsui and Akaogi [119]. This force field has been successfully adopted to simulate

bulk amorphous TiO_2 [79], TiO_2 nanoparticles [96, 5], as well as crystalline TiO_2 surfaces and TiO_2/water interfaces [13, 139]. Despite its deficiencies in reproducing exact cohesive energies, the advantages of the model are the simplicity and the robustness, which allow reliable simulations of a variety of systems, including in particular simulation cells with large numbers of atoms. On the other hand, in order to increase the transferability between different crystal polymorphs, more sophisticated classical potential models have emerged. These approaches take into account for example the charge transfer between metal and oxide atoms [162, 175, 69] and recently also the partially covalent character of the titanium-oxygen bonds [174], or they include a description of the atomic polarizability [73]. However, larger heterogeneous systems such as amorphous titanium oxides or thin superficial oxide layers, and, more importantly, interfaces between oxide surfaces and water, are still outside the scope of these potentials, at least in their present form.

2.2 Reactivity towards Water

Exposed to a physiological environment or even at ambient conditions one expects not only reactions with oxygen but also with water molecules to take place. These play an equally important role, as they determine the surface termination and the surface charge. While e.g. on silicon water always dissociates upon adsorption forming hydroxyl groups on the surface [39, 42], the dominant channel on oxidized titanium and crystalline titania is rather ambiguous and has been the subject of controversial discussions for decades [53]. As investigations of water adsorption are also part of this work, I shall refer to chapter 5 for a detailed discussion of this issue.

Experimentally, the reactions with water molecules on different titania surfaces have been investigated by spectroscopic techniques, such as XPS, DRS, AES and HREELS [11, 77], as well as temperature programmed desorption (TPD) [78, 106] and scanning tunneling microscopy (STM) [190]. The point of zero charge (PZC) of titanium has been measured to be around 5.5 [26] which is in consistence with an isoelectric point (IEP) of 5.0 as determined from XPS experiments [121], indicating that both basic as well as acidic surface terminations exist. The apparent surface charge of titanium has been measured to be about -0.13 C/m^2 at neutral pH-value [165].

From the modeling point of view, water adsorption on almost all possible TiO_2 crystal surfaces has been extensively investigated by means of density functional theory. An

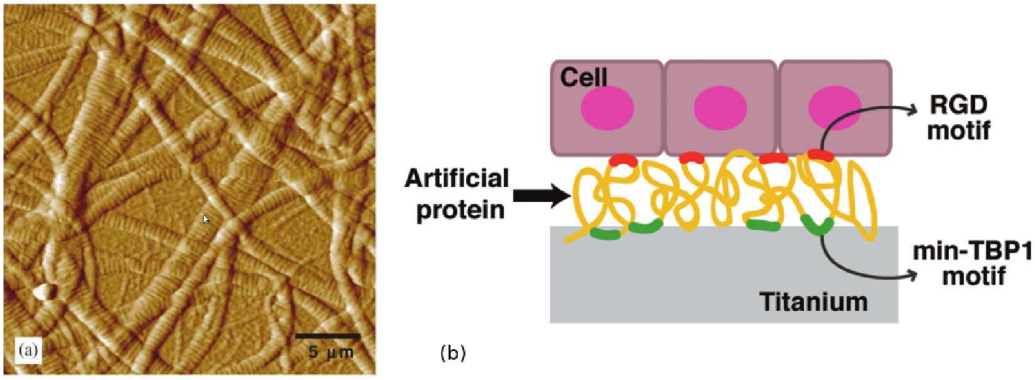

Figure 2.3: AFM picture of collagen fibrils immobilized on titanium ((*a*), taken from Ref. [141]). Scheme of an artificial, motif-programmed protein which combines specificity to titanium with enhanced cell adhesion ((*b*), taken from Ref. [95]).

excellent overview of these studies can be found in [161]. Empirical force field models of the interactions of water with TiO_2 crystals have been proposed as well, considering both neutral [13, 155] and charged surfaces [139, 97].

2.3 Biomolecular Adsorption

Successful cell adhesion at titanium based implants depends to a great extent on the adsorption and immobilization of proteins of the extracelluar matrix (ECM), such as collagen and fibronectin [141]. Most of these contain the arginine-glycine-aspartic acid (RGD) amino acid sequence which can be recognized by the integrin receptors at the cell membrane [144]. Enhancement of cell and bone adhesion upon implant surfaces has been achieved by coating the surface with ECM proteins or with small synthetic peptides enriched with the RGD-motif [141, 20] which have been immobilized electrochemically on the surface. In another study the cell adhesion could be controlled by the attachment of peptides to saccharide polymer brushes covalently immobilized on Ti [142]. Plasma treatment of the surface has also been found to facilitate protein adsorption [194], presumably as it increases the surface hydrophilicity [72].

An alternative approach to chemical or radiation treatment involves specific-binding-peptides [148, 152]. Extending the concept of molecular recognition to a surface being the host, these molecules exhibit a binding affinity only to a small range of substrates,

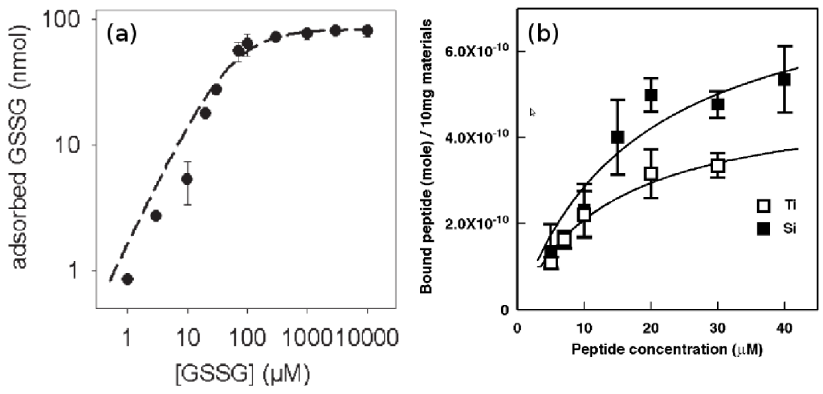

Figure 2.4: Adsorption isotherm and Langmuir fit of glutathione disulfide (GSSG) on α-Al_2O_3 nanoparticles (*a*, taken from Ref. [54]) and of the titanium-binding-peptide (TBP) RKLPDAPGMHTW on titanium and silicon particles (*b*, taken from Ref. [146]).

whereas they hardly adhere to other materials. Such peptide sequences have been identified for various kinds of materials including metals, metal oxides, compounds, carbon based materials and polymers [152, 57]. Considering titanium, for example, a motif built by the sequence RKLPDA has been found to exhibit strong specificity towards this material, but not to other substrates such as gold or iron [147, 76]. It is thus a consequent approach to utilize these molecules for immobilization of other molecules, such as specially tailored peptides, proteins and synthetic polymers on titanium surfaces in order to achieve the desired functionalization. This concept has been successfully applied not only to enhance cell adhesion [95], but also in the reverse way by coating the surface with poly (ethylene glycol) (PEG) to prevent further biomolecular adsorption as desired for anti-fouling surfaces [92]. Apart from medical purposes, the specificity seems to play an important role in biomineralization processes and can generally be employed in several bionanotechnological applications, e.g. the assembly of functional nano-devices [148, 152].

In spite of this progress, scientists are still at the verge of understanding the exact underlying atomistic mechanisms of molecular adsorption and surface recognition. Different theoretical models have been established to characterize the adsorption of molecules onto a substrate out of solution in general. The most widely used approach in this field is due to Langmuir [105] which assumes the presence of a certain density of equivalent adsorption sites [S_0], a coverage below one monolayer and no interactions between adsorbate

molecules. Its basic result is the formulation of the adsorption isotherm which quantifies the coverage $\Gamma = [A_{ads}]/[S_0]$ in dependence of the solution concentration $c = [A_{bulk}]$ or partial pressure p of the adsorbate

$$\Gamma = \frac{\Gamma_{max} c}{K_L^{-1} + c} \,. \tag{2.1}$$

When $[A_{ads}]$ is the surface density of adsorbed molecules and $[S]$ the density of unoccupied sites, $K_L = [A_{ads}]/(c[S])$ is the equilibrium constant of the adsorption reaction which is is this case referred to as the *Langmuir constant*. Fig. 2.4 shows two examples of experimentally measured adsorption isotherms along with the respective Langmuir fit of Eq. 2.1. Generally, the adsorption constant can be related to the free energy change upon adsorption via [64, 54]

$$\Delta G_{ads} = -k_B T \ln[K_L c_{solv}] \tag{2.2}$$

where c_{solv} is the solvent concentration, e.g. for water $c_{solv} = 55.5$ mol/l. Several modifications of the Langmuir theory have been proposed to describe the adsorption under different circumstances, such as the Freundlich adsorption isotherm [60], the Temkin isotherm [170] and the Brunauer-Emmet-Teller (BET) equation [27], where in particular the last model also applies to multilayer adsorption.

While standard experimental techniques to investigate adsorption, such as quartz-crystal microbalance (QCM) [92], surface-plasmon resonance (SPR) [169, 188] and light-extinction measurements [146] yield adsorption isotherms and the corresponding equilibrium constants, more advanced methods, e.g. nuclear magnetic resonance (NMR) and circular dichroism (CD), have recently been adapted to investigate the structure of adsorbed biomolecules [32, 66, 55, 156]. Moreover, atomic force microscopy (AFM) experiments nowadays can not only visualize patterns of adsorbed molecules on the surface, but also measure molecular adhesion forces, when the tip is functionalized with the respective molecules [108, 76]. The forces obtained this way quantify the adhesion strength and thus can be used to characterize the type of surface-molecule binding. Complementary to adsorption free energy databases [189], these values also provide important benchmarks to asses the accuracy of simulation models, as, in principle, they can be compared directly to the results of molecular dynamics simulations [82].

Since modeling of biomolecular adsorption on solid surfaces in principle gives exhaustive insights into the involved atomistic mechanisms, this field has received increasing attention. These simulations range from electronic structure calculations of small organic

molecules in vacuum [65, 110] over molecular dynamics simulations of peptides and small proteins [98, 154, 126, 133] to coarse-grained Brownian dynamics simulations of entire proteins [94].

2.4 Challenges in the Simulation of Interfaces

Although simulations have already contributed significantly to the understanding of phenomena at the interface between solid surfaces and physiological environment, a large number of questions and challenges remains open, with respect to the interpretation of the experimental results on the one hand and the reliability of the simulation results on the other hand [52].
Considering surface recognition and surface functionalization, the following aspects are of primary interest:

- The surface properties which dominate the selective adsorption.
- The role that the individual amino acids and the structure of the peptides play with respect to the specificity.
- The changes in the functionality of immobilized molecules after adsorption.

A deeper understanding of these points might ultimately enable scientists to propose new ways of tailoring the molecules and the surfaces to enhance the desired properties, e.g increase the selectivity of specific binding peptides.

The reliability of the simulation results depends basically on the following three factors:

- Accuracy of the force fields.
- Realistic surface models.
- Advanced sampling methods.

The simulations of solid-liquid interfaces usually employ a combined approach of biomolecular force fields and potentials to model the solid phase. As both sides are often developed independent of each other based on different concepts, they may not necessarily be compatible with each other. Hence, their combination must be carried out carefully and in a consistent way.

In adsorption simulations it has become a common approach, to consider idealized substrates, such as perfect crystal surfaces. Although these models provide valuable generic insights, important aspect of experimentally used substrates particularly in bio-engineering applications may not be captured. Features present on realistic surfaces can be of topological nature, such as steps, islands, ridges or valleys, or of chemical nature, such as charged terminations, different oxidation states of surface atoms or different surface compositions. The latter aspects govern e.g. the local hydrophilicity [1]. On the contrary, increased local heterogeneity makes it more difficult to derive converged quantitative results which can be considered representative for the respective surface.
Finally, in order to relate the microscopic simulation results to macroscopic observables such as free energies, it is crucial to take into account all possible microstates in a reasonable way. With respect to the case of biomolecules this means all relevant conformations as well as all adsorption and desorption pathways have to be included in the simulations which becomes increasingly important for larger molecules with a considerable number of internal degrees of freedom. Due to the limited accessible simulation time this can only be achieved by using advanced sampling techniques which enhance the exploration of the phase space, while keeping the computational cost as low as possible.

In this thesis I attempt to devise a multiscale based approach to tackle these challenges and to provide a way towards a more realistic description of interfaces between solid surfaces and physiological environment. Moreover, I will proceed to show that such a model can provide valuable insight into the specificity of titanium-binding-peptides.

Chapter 3

Molecular Dynamics Simulations

In nanoscience and nanotechnology effects caused by microscopic processes at the atomic length scale play a most important role. Although such effects can successfully be detected and investigated in experiments, the exact underlying microscopic mechanism often remains unclear. Attempting to retrace the motion of the involved particles, molecular dynamics (MD) simulations provide a promising way to complement and understand the experiments. MD simulations can not only reconstruct experimentally observed effects but sometimes even predict formerly unknown effects and point out the route to new experiments. However, when interpreting the simulation results one must always bear in mind that these calculations contain approximations and that their results are only as accurate as the assumptions underlying the respective simulation model.
In the following chapter the basic concepts of molecular dynamics simulations and the most common atomic interaction models, from *ab initio* techniques to empirical force fields, are summarized. Furthermore, a brief overview over thermodynamics and statistical mechanics in the context of molecular simulations is given, focusing in particular on free energy calculations and sampling methods.

3.1 Classical Equations of Motion

In classical mechanics a system consisting of N particles can be described by its configuration $\{\boldsymbol{R};\boldsymbol{P}\}$ in $6N$-dimensional phase space, where $\boldsymbol{R} = (\boldsymbol{r_1},\ldots,\boldsymbol{r_N})$ and $\boldsymbol{P} = (\boldsymbol{p_1},\ldots,\boldsymbol{p_N})$ represent the particles' positions and conjugate momenta. The motion of this system can be formulated analytically within the framework of Hamiltonian me-

chanics [70, 71]. The central quantity in this formalism is the Hamilton function, or *Hamiltonian*, which is written as

$$\mathcal{H} = T(\boldsymbol{P}) + V(\boldsymbol{R}) \,, \tag{3.1}$$

where T represents the kinetic energy and V the potential energy of the system. Relating it to the original formulation of Lagrangian mechanics, the Hamiltonian is obtained from the Lagrange function $\mathcal{L} = T - V$ via Legendre transformation. Based on the principle of stationary action the Hamilton equations can be derived as

$$\dot{\boldsymbol{p}}_i = -\frac{\partial \mathcal{H}}{\partial \boldsymbol{r}_i} \,, \; \dot{\boldsymbol{r}}_i = \frac{\partial \mathcal{H}}{\partial \boldsymbol{p}_i} \,. \tag{3.2}$$

When writing the kinetic energy as $T = \sum_i \boldsymbol{p}_i^2/(2m_i)$, Newton's second law

$$m_i \ddot{\boldsymbol{r}}_{\boldsymbol{i}} = -\nabla_i V = \boldsymbol{f}_{\boldsymbol{i}} \,, \tag{3.3}$$

is retrieved, where $\boldsymbol{f}_i$ denotes the force acting on particle i. Hence, assuming the knowledge of the potential energy $V(\boldsymbol{R})$ for each point in configuration space and the initial conditions $\{\boldsymbol{R}(t=0); \boldsymbol{P}(t=0)\}$, one can in principle integrate Eq. 3.3 and, in combination with Newton's first law, obtain the classical motion of the system for all times [63]:

$$\boldsymbol{P}(t) = \int_0^t dt' \nabla V(\boldsymbol{R}(t')) + \boldsymbol{P}(0) \tag{3.4}$$

$$\boldsymbol{R}(t) = \int_0^t dt' \frac{1}{m} \boldsymbol{P}(t') + \boldsymbol{R}(0) \tag{3.5}$$

3.2 Time Integration

The basic limitation of this ansatz is the fact that Eqs. 3.4 and 3.5 cannot be solved analytically for systems containing more than two particles. Yet, as pointed out in the following, suitable strategies for a numeric solution exist.

3.2.1 Velocity Verlet

In order to integrate the system of equations 3.4 and 3.5 the time t is discretized into small intervals δt. Assuming constant forces within each of these intervals, the trajectory in phase space can be constructed step by step [6]. In the limit $\delta t \to 0$ the schemes

should converge to the exact integrals. However, the order of convergence is an important factor, as it determines the accuracy of the integration and therefore the efficiency of the simulation.

To propagate the system from a known state at time t to the next step at $t+\delta t$ a truncated Taylor expansion can be applied:

$$\boldsymbol{R}(t+\delta t) = \boldsymbol{R}(t) + \dot{\boldsymbol{R}}(t)\delta t + \frac{1}{2}\ddot{\boldsymbol{R}}(t)\delta t^2 + \mathcal{O}(\delta t^3) \tag{3.6}$$

As the time derivatives are only known up to the second order, the error for this scheme is $\mathcal{O}(\delta t^3)$.

A more efficient and thus more popular method is the *velocity-verlet* integration algorithm [182, 163]. In contrast to Eq. 3.6 the velocities are evaluated in the middle of each timestep, $t + \delta t/2$ based on the average force associated with the embracing positions t and $t + \delta t$. Its mathematical formulation writes as

$$\boldsymbol{R}(t+\delta t) = \boldsymbol{R}(t) + \boldsymbol{V}(t)\delta t + \frac{1}{2}\frac{\boldsymbol{F}(t)}{M}\delta t^2 \tag{3.7}$$

$$\boldsymbol{V}(t+\delta t) = \boldsymbol{V}(t) + \frac{\boldsymbol{F}(t) + \boldsymbol{F}(t+\delta t)}{2M}\delta t\,, \tag{3.8}$$

where $\boldsymbol{V} = \dot{\boldsymbol{R}}$ stands for the array of particle velocities. The iterative application of these equations yields the trajectory of each particle and propagates the system in time. Compared to the truncated Taylor expansion it can be shown that the convergence of the velocity verlet algorithm is $\mathcal{O}(\delta t^4)$. It offers enhanced stability and it is time-reversible. As the total energy of the system is conserved, the velocity verlet algorithm resembles a microcanonical (NVE) ensemble.

3.2.2 Thermostats

Instead of considering a microcanonical ensemble one can as well simulate a system at constant temperature which is useful in order to mimic an experimental setup. In experiments the temperature is maintained by keeping the system in equilibrium with a heat bath. Although its macroscopic size usually forbids the inclusion of an atomistic heat bath in MD simulations, yet, several strategies have been devised to control the system temperature. When doing so, one has to make sure that the distribution of energies corresponds to a canonical ensemble.

3.2.3 Langevin Thermostat

A widely used approach is to couple the system to a continuous heat bath [179]. This can be accomplished by augmenting the equations of motion 3.3 by a friction force and a fluctuating stochastic force as if the system was immersed into a dissipative medium. By doing so one obtains the Langevin equation

$$m_i \ddot{\boldsymbol{r}}_{\boldsymbol{i}}(t) = \boldsymbol{f}_{\boldsymbol{i}}(t) - \gamma \dot{\boldsymbol{r}}_{\boldsymbol{i}}(t) + \boldsymbol{\Gamma}_{\boldsymbol{i}}(t)\,. \tag{3.9}$$

The damping constant γ is related to the magnitude of the random force via the fluctuation dissipation theorem

$$\langle \boldsymbol{\Gamma}_{\boldsymbol{i}}(t) \cdot \boldsymbol{\Gamma}_{\boldsymbol{j}}(t') \rangle = 2\gamma k_B T \delta_{i,j} \delta(t - t')\,. \tag{3.10}$$

Obeying this relation assures that the energy which is additionally introduced into the system by the random force, and the energy which is removed by dissipation, in total balance each other in order to maintain a constant temperature. An essential effect of this method is, that it couples every particle individually to the heat bath, as the forces act locally on each particle. The temperature is uniformly distributed over the system, avoiding temperature gradients. On the contrary, due to the random force this approach no longer yields time-reversibility.
In the limit of large friction $\gamma \to \infty$, inertial effects vanish completely. Instead of Langevin dynamics the system obeys Brownian dynamics in that case.

3.2.4 Berendsen Thermostat

A way to control the temperature without introducing a random force, is offered by the Berendsen thermostat. In the Berendsen approach it is assumed that the temperature development of the system obeys the following equation:

$$\frac{dT}{dt} = \frac{T_0 - T(t)}{\tau_T}\,, \tag{3.11}$$

introducing a temperature coupling time constant τ_T and a target temperature T_0. This scheme is commonly implemented into the velocity verlet algorithm by scaling all velocities after the integration by a uniform scaling factor

$$\xi = \left[1 + \frac{\delta t}{\tau_T}\left(\frac{T_0}{T(t+\delta t)} - 2\right)\right]^{1/2}\,, \tag{3.12}$$

where $T(t+\delta t) = 2E_{kin}(t+\delta t)/(fk_B)$ is the new temperature and f denotes the number of degrees of freedom of the system. Hence, the system temperature approaches the target temperature exponentially which, under normal circumstances, keeps the system rather stable even for small time constants.
Compared to the Langevin thermostat the temperature coupling is less tight, as it acts uniformly on all particles and therefore does not disturb the local dynamics of the system. Since the distribution of the velocities differs slightly from the Maxwell-Boltzmann distribution, it does not maintain an exact canonical ensemble, yet, the deviations are usually negligible.

3.2.5 Nosé-Hoover Thermostat

An exact NVT ensemble can be achieved by employing a Nosé-Hoover-thermostat [81]. In this approach the scale factor $\xi(t)$ is introduced into the equations of motion as a further equivalent degree of freedom of the system:

$$\ddot{\boldsymbol{R}}(t) = \frac{\boldsymbol{F}(t)}{M} - \xi(t)\dot{\boldsymbol{R}}(t) \tag{3.13}$$

$$\frac{d\xi(t)}{dt} = \frac{T(t) - T_0}{Q}\,. \tag{3.14}$$

$Q = T_0{\tau_T}^2$ includes the coupling time constant and can be interpreted as a mass of ξ. The integration of Eq. 3.14 is embedded into the velocity verlet scheme in which the velocities are scaled twice during one time step. As the mass Q introduces an inertial effect into the temperature dynamics, the Nosé-Hoover method has the shortcoming that particularly for small time constants the temperature can exhibit large oscillations. Therefore the system can turn out less stable in some cases, compared the Berendsen ensemble.
Apart from these methods, several other approaches have been devised to control the temperature of the system, such as the Andersen thermostat [7] or stochastic velocity rescaling [29], which might be suitable under certain conditions.

3.2.6 Barostats

Sometimes it is desired to couple the system not only to a heat bath but also to control the pressure in the system allowing for changes of the simulation cell size. The simulated system then corresponds to an NPT ensemble.

Pressure coupling is generally accomplished in a way that is similar to temperature coupling:
The pressure tensor or, for isotropic systems, the scalar pressure is evaluated and the cell size (including its interior, i.e. the particle coordinates) is scaled by a factor which is determined similarly to the temperature scale factor from the difference between the current pressure $P(t)$ and the target pressure P_0. For anisotropic systems the scale factor $\underline{\eta}$ is a tensor itself which acts on the cell vectors as $\boldsymbol{L_\alpha}' = \underline{\eta} \cdot \boldsymbol{L_\alpha}$. This changes not only the size of the cell but also its shape. It is furthermore possible to include only selected components of the pressure tensor in the coupling, e.g. for surface-liquid interfaces it is sometimes useful to control the pressure only along the direction of the surface normal, while the lateral dimensions of the cell which are determined by the crystal structure of the substrate remain constant.
Two of the most common schemes are the Berendsen barostat and the Nosé-Hoover barostat. In both approaches the scale factor is determined in analogy to the respective thermostat. Accordingly, the Berendsen barostat offers better stability compared to the Nosé-Hoover barostat, as it does not cause pressure oscillations. On the contrary, only the Nosé-Hoover scheme yields an accurate NPT ensemble.

3.2.7 Periodic Boundary Conditions

The number of particles that can be treated in molecular dynamics ranges from a few atoms to about a million particles, depending on how elaborate the computation of the interactions is. Even at the upper boundary of this range, the corresponding system size is usually still small compared to macroscopic systems which means that artificial boundary effects can contribute considerably to the systems' properties. A practical way to deal with this problem is to apply periodic boundary conditions. This means that images of the system are copied and translated by all possible linear combinations of the cell vectors. These images interact with the original particles which mimics an infinitely extended macroscopic system. This way artificial boundaries, such as walls, imposed to contain the particles in the cell are avoided. Moreover, since the interactions are in most cases short-ranged it is enough to consider only the first "shell" of images.
The calculation of short-ranged interactions obeys the minimum image convention which means one always takes into account only the smallest possible distance between two particles or between its periodic images. In order to calculate long-ranged interactions,

e.g. electrostatic interactions, strategies have been developed (cf. Sec. 3.3.2). Of course, the concept of periodic boundary conditions does not completely prevent finite-size effects, as the periodicity of the repeated images might still influence the system's behavior, in particular for small cells. Thus, one is always advised to test the convergence of certain properties with respect to the system size to exclude significant artefacts.

3.3 Interaction Models

A central issue in molecular dynamic simulations are the interactions among the particles, as they determine the forces as well as the energies and thus all the properties of the system. It is thus of great importance to choose an appropriate interaction model. In doing so, one has to balance computational efficiency and accuracy depending on what properties one desires to investigate.
One commonly differenciates between ab initio methods which are based on quantum mechanics, and empirical pre-defined force fields. While the former class additionally takes into account the electronic degrees of freedom of the atoms, the latter methods usually only depend on the positions of the atoms themselves.

3.3.1 Ab Initio Methods

On the atomic scale, the system no longer follows exactly the classical equations of motion, but rather obeys the laws of quantum mechanics. One of the fundamental differences is that the particles, in particular the electrons, are not represented by their positions and momenta anymore, but in terms of wave functions. The wave functions are determined by solving the Schrödinger-Equation [151]

$$\hat{H}|\Psi_i\rangle = E_i|\Psi_i\rangle\,. \tag{3.15}$$

where $\hat{H} = \hat{T} + \hat{V}$ is the Hamilton operator, the quantum mechanical analogon to the classical Hamiltonian, and E_i, $|\Psi_i\rangle$ are the energy eigenvalue and the wavefunction of state i.

In principle this equation has to be solved for both core ions and electrons of the system. Considering the heavy mass of the atomic cores which exceeds the electronic mass by several orders of magnitude, a way to approximately treat such systems is to separate the motion of the electrons from the motion of the ions. In this adiabatic

approximation the resulting electronic Hamilton operator includes the ionic positions merely as parameters, by treating the electrostatic interactions between ions and electrons as an external field $v(\boldsymbol{r})$ [25]:

$$\hat{H}_{BO} = -\frac{1}{2}\sum_i \nabla_i + \frac{1}{2}\sum_{i,ji\neq j} \frac{1}{|\boldsymbol{r_i} - \boldsymbol{r_j}|} + v(\boldsymbol{r}) = \hat{T} + \hat{V}_{ee} + \hat{V}_{ext}\,. \tag{3.16}$$

The corresponding wave function $\Psi(\{\boldsymbol{r_i}\})$ depends only on the coordinates of the electrons. This approximation is well-known under the name Born-Oppenheimer approximation.

Density Functional Theory

Another difficulty that is still contained in the Born-Oppenheimer electronic Hamiltonian is the exchange symmetry of the electrons which renders the calculation of the exact electronic wavefunction complicated and computationally demanding. Instead of dealing with the full electronic wave functions one can consider the electronic density $n(\boldsymbol{r})$ as the central quantity and express observables as functionals of this quantity [136, 117].
The basic idea behind density functional theory was formulated by Hohenberg and Kohn in 1964 [80], which states that a unique mapping between the external potential $V_{ext}(\boldsymbol{r})$ and the density $n(\boldsymbol{r})$ exists.
As a consequence, the energy can be written as:

$$E[n] = T[n] + V_{ee}[n] + \int d\boldsymbol{r} v(\boldsymbol{r}) n(\boldsymbol{r})\,. \tag{3.17}$$

The density function $n_0(\boldsymbol{r})$ which minimizes this energy functional corresponds to the ground state density. In principle Eq. 3.17 is exact, however, the functional dependence of the kinetic energy $T[n]$ as well as the electron-electron interaction $V_{ee}[n]$ is unknown. The basic approximation of density functional theory, as proposed by Kohn and Sham [93], is to replace the exact system by an auxiliary system of uncorrelated electrons with single particle wave functions $\Psi_i^0(\boldsymbol{r})$. This still yields the exact properties of the system as long as the density of the auxiliary system is equal to the original density. The notion of uncorrelated electrons, though, simplifies the calculation of the kinetic energy operator $\hat{T}^0$ and it reduces the electron-electron interaction to a coulombic Hartree energy $V_{Hartree}$. In order to account for the difference between the original system and the auxiliary system of independent electrons, one introduces another energetic contribution, the so-called

exchange-correlation functional $V_{xc}[n]$, which is the only remaining unknown expression in the formalism of density functional theory. Fortunately, in most cases its contribution appears to be small compared to the kinetic energy. Moreover, approximations to this term exist, which have been proven sufficiently accurate to calculate many physical properties for a wide range of materials.
The most common classes of exchange correlation functionals are the local density approximation (LDA), the generalized gradient approximation (GGA) and hybrid functionals, such as B3LYP [18]. All of them have revealed certain advantages and drawbacks in their performance and their computational efficiency, depending on the particular case and material.

Further practical approximations are common in state-of-the-art DFT codes to increase the computational efficiency.
The wave functions are expanded in an appropriate basis set for which the mathematical operations are easy to perform. The two most popular types of basis sets are (simplified) atomic orbitals and plane waves. While the former type is well suited for isolated atoms or molecules, the latter type intrinsically contains a periodicity, which makes them ideal for crystalline solids. The precision of this expansion can be controlled by the number of basis functions being included. For plane waves this is determined by the maximum wave vector k_{max} which is usually given in terms of the associated maximum electronic kinetic energy E_{cut}.
Crystalline solids require integrals over the wave vectors in the Brillouin zone (BZ), which can be approximated by a weighted sum including only a limited number of special points. The most popular choice for this k-point sampling is the Monkhorst-Pack scheme [125]. Problems arise for metals featuring partially filled bands near the fermi level, which introduce discontinuities. Such systems have to be treated with special algorithms, which apply a fictitious temperature and thus smear the discontinuities smoothly over a finite energy range of about 0.1 eV [180, 159].

Finally, it is common in DFT to treat only the valence electrons explicitly, whereas the core electrons are considered as fixed, because they hardly contribute to the properties and the reactivity of the material. By introducing so-called pseudopotentials which imitate the interaction between the core electrons and the valence electrons, this approximation

saves computational time due to the reduced number of degrees of freedom. These pseudopotentials characteristically have a very smooth shape avoiding the rapid oscillations and the coulomb singularity close to the atomic core which would require high-frequency plane waves and correspondingly high cutoff energies. Of course, one has to be careful when constructing such pseudopotentials, as they must not change the properties of the material significantly. The scheme that has been used throughout this work is the so-called projector augmented wave (PAW) method, proposed by Blöchl[23].

First Priciples Molecular Dynamics

Apart from the electronic density and total energy, density functional theory allows to calculate the forces acting on the core ions. This task is tremendously simplified by the Hellman-Feynman theorem, which states that if the system is in its ground state, these forces correspond the expectation value of the derivative of the Hamilton operator [58]:

$$\boldsymbol{F}_I = \sum_i \langle \Psi_i | -\frac{\partial \hat{H}_{KS}}{\partial \boldsymbol{R}_I} | \Psi_i \rangle \ . \tag{3.18}$$

The knowledge of the forces generally enables to perform molecular dynamics according to the schemes described in the previous section. One distinguishes between two ways in which these simulations can be carried out [118]. In Born-Oppenheimer (BO) molecular dynamics the electronic wave functions and the resulting forces are calculated at every time step by solving the Born-Oppenheimer-Schrödinger equation 3.16.
A usually more efficient way is the Car-Parrinello method [34], which is also based on the Born-Oppenheimer approximation, but in addition it includes the electronic degrees of freedom into the classical dynamics. Assigning a fictitious mass μ to the electronic orbitals, the classical Lagrangian can be written as

$$\mathcal{L} = \sum_i \frac{1}{2}\mu \int d\boldsymbol{r} |\dot{\Psi}_i|^2 + \sum_I \frac{1}{2} M \dot{\boldsymbol{R}}_I - E\left[\{\Psi_i\}, \{\boldsymbol{R_I}\}\right] \ , \tag{3.19}$$

where the Ψ_i are subject to the constraints of orthonormality. The associated equations of motions are formulated as described in Sec. 3.1. This approach allows to apply dynamical minimization methods to reach the ground state instead of repeated matrix diagonalization or direct minimization. Furthermore, given that in MD simulations two subsequent configurations of ions differ only very little from each other, it is often sufficient to integrate the electronic equations of motion over just one timestep to obtain new

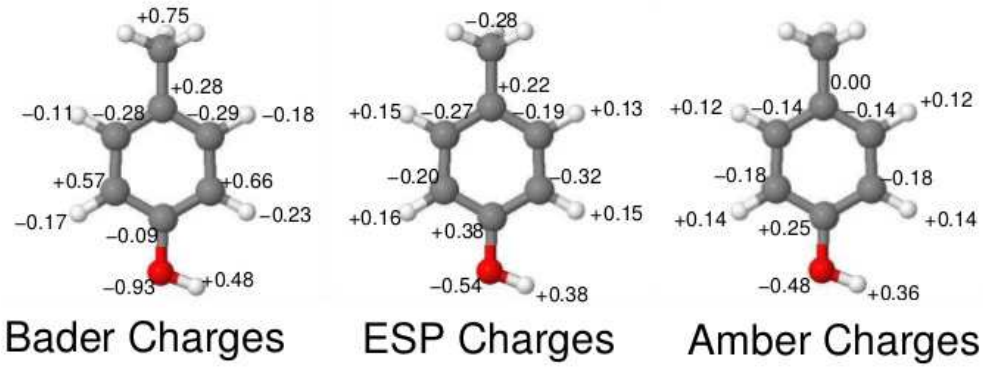

Figure 3.1: Charge values for the truncated tyrosine amino acid obtained from Bader analysis and ESP fit compared to the charges taken from the AMBER force field [45].

wavefunctions that are reasonably close to the actual ground state, instead of performing a full self-consistent minimization.

Charge Calculation

The local distribution of the electronic density obtained in a DFT calculation may be analyzed in terms of atomic point charges which is useful, e.g. to quantify the atomic oxidation state. Apart from that, quantum mechanical charges play an important role in the parametrization of empirical force fields, as they determine the electrostatic interactions. Various methods have been devised to calculate atomic charges from quantum mechanical calculations. Since they are based on different concepts the results commonly deviate from each other.

One possible approach are electrostatic potential derived (ESP) charges. One utilizes the electrostatic potential

$$V(\boldsymbol{r}) = \sum_I \frac{Z_I}{|\boldsymbol{r} - \boldsymbol{R}_I|} - \int d\boldsymbol{r}' \frac{\rho(\boldsymbol{r}')}{|\boldsymbol{r} - \boldsymbol{r}'|} \tag{3.20}$$

originating from the electronic density ρ and the charge of the core ions I. The charges are determined by fitting a set of point charges located at the positions of the ions to reproduce this potential outside the Van der Waals radii of the atoms [124, 46, 153, 191]. The last requirement renders this method feasible only for isolated molecules or surfaces, as one needs a considerable amount of unoccupied volume to obtain reasonable values.

Moreover, it implies that the electrostatics arising from ESP charges are well-suited primarily to calculate intermolecular interactions. In some cases subsurface atoms can suffer from unphysically high charge values as their electrostatic potential is screened by atoms close to the surface, as discussed in chapter 5. A common modification to this technique is the restrained electrostatic potential (RESP) charges method [17] which introduces restraints into the fitting procedure in order to increase the transferability of the charges of functional groups among different molecular contexts. This method is very popular in the field of biomolecular modeling, and most of the partial charges used in biomolecular force fields are obtained this way.

Another set of charges which is calculated in a very robust and unambiguous way, are the Bader charges, obtained on the basis of the *atoms in molecules* concept [12]. This approach defines atomic volumes by dividing space into separate basins, each associated with a certain atom. The division is carried out based on the gradients of the electronic density. In detail, each grid point is assigned to the atom that is ultimately reached when following the path of steepest increase of the density. Consequently, surfaces with vanishing gradient define the boundaries between different atomic volumes. In a second step the charges are calculated by integrating the charge density within these atomic basins.

In contrast to Mulliken charges [130] for example which are calculated as a population analysis by a projection of the wave function onto atomic orbital basis functions centered on the respective atom, the Bader charges are independent of the chosen basis set. Moreover, as Bader charges do not suffer from screening of buried atoms, changes in the oxidation state are captured reliably by this method, making it a good starting point to calculate the cohesive interactions within heterogeneous ionic solids for example. However, compared to the ESP charges the magnitude of the Bader charges is usually larger which can result in incorrect electrostatic potential values outside the molecule or the surface. As an example, Bader and ESP charge values for the tyrosine amino acid are displayed in Fig. 3.1 along with the RESP charges from the AMBER force field.

3.3.2 Empirical Force Fields

The prize one has to pay for the chemical accuracy of ab initio methods is the relatively small system size. Depending on the particular system, energy calculations are possible for up to about one thousand atoms at most, whereas molecular dynamics simulations using the Car-Parrinello method are feasible for only a few hundreds of atoms to achieve

reasonable simulation times of the order of 10 picoseconds. Generally, this limits the applicability of ab initio methods to very simplified model systems.
Fortunately, many molecules and solids move on a rather well-defined and reproducible potential energy landscape. As long as no chemical reactions are involved one can utilize this finding by defining the interaction potentials prior to the simulation. When calculating the interactions merely as a function of the atomic positions one avoids solving the Schrödinger equation for the electronic degrees of freedom which is the most elaborate part of ab initio calculations.
Such interaction models can be defined either on a semi-empirical basis by deriving the potential energy functions directly from the quantum mechanical equations or empirically by mapping the potential energy to appropriate functions. The parameters of these functions are tuned by fitting to suited target values which can be DFT energies, experimental observables or atomic and molecular structures. These reference values have to be chosen carefully according to which properties one is ultimately interested in investigating. Special care has to be taken when a model is transferred into a new context, for which it has not been explicitly tailored. One has to test carefully by comparing to experiments or to ab inito calculations whether the model still extrapolates well to the new situation, and possibly reparametrize the force field.
A large number of established force field models exist for a broad range of materials, such as biological molecules, metallic or ionic crystals and all kinds of liquids which will be described briefly in the following.

Ionic Force Fields

To model a purely ionic crystal it often turns out to be sufficient to include only electrostatic and short-ranged interactions:

$$V^{ionic} = \sum_{i<j} \frac{q_i q_j}{r_{ij}} + \sum_{i<j} V^{SR}(r_{ij}) \tag{3.21}$$

The electrostatic interactions are determined by the point charges of each ion which can be partial charges or formal charges. The short-ranged interactions accomplish the repulsion between the ions at small distances due to the Pauli-principle. Furthermore, they can account for dispersion effects. A typical function that is used for this kind of interactions

is the Buckingham potential

$$V^{Buck}(r_{ij}) = A_{ij}e^{-r_{ij}/\rho_{ij}} - \frac{C_{ij}}{{r_{ij}}^6}\,. \tag{3.22}$$

Embedded Atom Potentials

For metallic crystals the cohesion is not accomplished primarily by classical electrostatic interactions as it is the case for ionic materials, but rather by the nearly free electrons in the valence band. Such interactions are basically of quantum mechanical nature which renders a classical description more complicated. The semi-empirical embedded atom method (EAM) [50] or the closely related Finnis-Sinclair (FS) [59] potentials have turned out successful in the description of many different metals. In contrast to the previous case of pair-interactions these methods are formulated as manybody potentials. The general form is described as

$$V^{EAM} = \sum_{i<j} V^{pair}(r_{ij}) - \sum_i F^{embed}(\rho_i)\,, \tag{3.23}$$

where the first term V^{pair} describes pairwise repulsion and the second term F^{embed} represents the embedding energy which is a functional of the embedding density

$$\rho_i = \sum_j \rho_{ij}(r_{ij})\,. \tag{3.24}$$

The density ρ_i of each atom is calculated as the sum over all contributions ρ_{ij} from neighboring atoms. The embedding functional F^{embed} is, especially for FS-type potentials, typically the square root of the density, although for general EAM potentials it can also have different forms.

Biomolecular Force Fields

Modeling of biological molecules, such as proteins, nucleic acids or lipids, has developed into a vital field offering several well-established force fields. Among the most popular ones are the AMBER [45], CHARMM [116] or the OPLS [90] force field. As the AMBER force field has been used in the present work, its functional forms will be introduced in detail. It should be remarked, though, that most of these potential models use the same or very similar functional forms, only with different parameters.

The AMBER force field consists of the following terms:

$$V = \sum_{bonds} k^b (r_{ij} - r_0)^2 + \sum_{angles} k^\theta (\theta_{ijk} - \theta_0)^2 + \sum_{dihedrals} \frac{k^\phi}{2} [1 + \cos(n\phi_{ijkl} - \gamma)]$$

$$+ \sum_{pairs} \epsilon_{ij} \left[\left(\frac{\sigma_{ij}}{r_{ij}} \right)^{12} - 2 \left(\frac{\sigma_{ij}}{r_{ij}} \right)^{6} \right] + \sum_{pairs} \frac{q_i q_j}{r_{ij}} \tag{3.25}$$

The model includes intramolecular terms which describe the topology and the structure of a molecule. These are chemical bonds, angle bending, and dihedral angles. Bonds are modeled by a harmonic potential with spring constant k and equilibrium bond length r_0. Angle bending terms account for the stiffness of two connected bonds by including an angle force constant k^θ and equilibrium angle θ_0. Dihedral angles describe the torsion of four atoms around the central bond by the dihedral force constant k^ϕ, the periodicity n and the phase γ. Improper dihedrals have the same functional form as dihedral potentials, but describe the out-of-plane torsion of a planar group of atoms.
Additionally, Eq. 3.25 contains intermolecular terms which govern primarily the interaction between different molecules and between topologically remote parts of the same molecule. These contributions are described by Lennard-Jones and electrostatic Coulomb interactions. The Lennard-Jones term originally accounts for interatomic repulsion and van-der-Waals interactions, although it is often used to include all kinds of energetic contributions that are not captured by the previous potentials. The Lennard-Jones coefficients for a pair of interacting atoms i and j can be obtained from the atomic coefficients ϵ_i and σ_i using combination rules. In the context of the AMBER force field Lorentz-Berthelot rules apply, yielding $\epsilon_{ij} = \sqrt{\epsilon_i \epsilon_j}$ and $\sigma_{ij} = \sigma_i + \sigma_j$. The electrostatic interactions are based on partial charges q_i which are usually determined from ab initio calculations by the RESP method (cf. Sec. 3.3.1).

A special case of particular importance is the modeling of water molecules which is present as solvent in most systems. As molecules and surfaces interact with each other primarily via their solvation shell, an accurate description of water molecules is of vital importance. Several water models exist, yielding properties that sometimes differ slightly from each other. The most common ones are the simple point charge (SPC) model, the TIP3P or the TIP4P models [89]. The AMBER force field normally employs the TIP3P model which features constrained O-H bonds and constrained H-O-H angles. It interacts

with other molecules via non-bonded Lennard-Jones and electrostatic interactions with partial charges of $q_O = -0.834$ e and $q_H = 0.417$ e.

Electrostatic Interactions

The Lennard-Jones potential decays quickly as r^{-6} and can thus safely be truncated after an appropriate cutoff distance, rendering its computation quite efficient. In contrast, coulomb interactions merely decay as r^{-1}. Truncating such long ranged interactions generally leads to more pronounced errors, unless the cut-off radius is increased significantly which slows down the calculation considerably. A computationally efficient way to avoid the truncation of the coulomb interactions for neutral systems is the Ewald sum [6]. This method adds to each point charge a fictitious cloud of opposite charges which effectively screens the electrostatic potential at large distances. To compensate for this, the interactions of the additional set of charged clouds alone are evaluated in reciprocal space using the Poisson equation. The results are then subtracted from the previously calculated forces and energies. In practice the electrostatics are calculated using the following formula:

$$V^{es} = \sum_{i<j, r_{ij}<r_c} \frac{q_i q_j}{r} erfc(\alpha r_{ij}) + \frac{2\pi}{V} \sum_{\boldsymbol{k}} \frac{\exp(-k^2/4\alpha^2)}{k^2} |\sum_i q_i \exp(-i\boldsymbol{k}\cdot\boldsymbol{r}_i)|^2 \,, \qquad (3.26)$$

where the first term describes the truncated screened real space contribution and the second term represents the reciprocal space part. For the calculation of the reciprocal space contribution several schemes exist to map the charges onto a mesh prior to the fourier transform and to evaluate the interactions of the electric field with the particles afterwards. The methods employed in this work are the smoothed particle mesh ewald (SPME) [56] and the particle-particle particle-mesh (PPPM) [48] technique.

3.4 Free Energy Calculations

In order to compare the results with experiments one has to bear in mind that usually only a limited collection of possible microstates is considered in simulations. Therefore the thermodynamics and statistical mechanics of the ensemble in which the experiments and the simulations are performed play a crucial role in linking the simulation results to macroscopic observables.

In statistical mechanics the measured quantities are expressed as an average over all possible microstates spanning the entire phase space $\Gamma = \{\boldsymbol{R}; \boldsymbol{P}\}$ (cf. section 3.1) of the system. Most of the simulations presented in this work are performed in the canonical NVT ensemble. The corresponding probability associated with each microstate i and corresponding $(\boldsymbol{R}_i, \boldsymbol{P}_i)$ is thus

$$P(\boldsymbol{R}_i, \boldsymbol{P}_i) = \frac{1}{Z} \exp(-\beta \mathcal{H}(\boldsymbol{R}_i, \boldsymbol{P}_i)) \,, \tag{3.27}$$

Here $\mathcal{H} = T + V$ is the classical (or quantum mechanical) Hamiltonian of the system, $\beta = 1/(k_B T)$ is the inverse thermal energy and

$$Z = \int \int d\boldsymbol{R} d\boldsymbol{P} \exp(-\beta \mathcal{H}(\boldsymbol{R}, \boldsymbol{P})) \tag{3.28}$$

is the canonical partition function of the system which normalizes the probabilities. The thermodynamic potential associated with the canonical ensemble is the *Helmholtz free energy* $G = U - TS$ which is composed of the internal energy U and the entropy S of the system (whereas the *Gibbs free energy* contains the enthalpy instead of the internal energy, as it is associated with an NPT ensemble). Relating thermodynamics to statistical mechanics, the free energy can be expressed in terms of the partition function

$$G = -k_B T \ln Z \,. \tag{3.29}$$

In contrast to the calculation of the average observables, the direct evaluation of Eq. 3.29 from molecular dynamics simulations appears to be a difficult task, as the probability distribution 3.27 does not favor high-energy microstates. Such states, though, may contribute significantly to the free energy. In practice however, one is more interested in free energy differences between different subsystems than in absolute values. Since free energy is the driving force in the canonical ensemble, its differences govern the relative population of the subsystems. Introducing the partition functions Z_A and Z_B of subsystems A and B, one obtains

$$\Delta G = -k_B T \ln \frac{Z_A}{Z_B} \,. \tag{3.30}$$

The differences between the two subsystems can be of various nature: One can imagine subsystems which differ from each other in their Hamiltonians, their temperatures, or they occupy different regions Γ_A and Γ_B in phase space. In the context of this work one can distinguish for instance between a molecule adsorbed on a surface and the free

molecule in solution. Instead of a single ΔG value between two separate subsystems one can as well consider a continuous reaction coordinate $\lambda = \lambda(\boldsymbol{R})$ and calculate the free energy profile along its path:

$$G(\lambda) = -k_B T \ln P(\lambda) + G_0 \tag{3.31}$$

Here G_0 is an arbitrary additional constant, $P(\lambda) = Z(\lambda)/Z$ and

$$Z(\lambda) = \int d\boldsymbol{R} d\boldsymbol{P} \exp(-\beta \mathcal{H}(\boldsymbol{R}, \boldsymbol{P})) \delta(\lambda - \lambda(\boldsymbol{R})) \,. \tag{3.32}$$

Since Eq. 3.31 can be written in terms of the driving force $dG/d\lambda$ as

$$G(\lambda) = \int_{\lambda_0}^{\lambda} \frac{dG(\lambda')}{d\lambda'} d\lambda' + G(\lambda_0) \,, \tag{3.33}$$

the free energy profile is often called the *potential of mean force* (PMF).
When using non-cartesian reaction coordinates one additionally has to take into account the change of phase space volume in dependence of the reaction coordinate value [178].

Although the consideration of free energy differences instead of absolute values in principle simplifies the numerical treatment, one still has to devise suitable methods to practically calculate these values in simulations.

A straightforward way is to utilize Eq. 3.31 and run an equilibrium simulation for a long time to measure the probability distribution $P(\lambda)$ by counting the occurrences associated with each value of λ. While this works well for rather flat free energy landscapes, for more structured profiles it often leads to the reaction coordinate being trapped in a local free energy minimum which it cannot escape in the accessible simulation time. Other regions which might contribute significantly to the global free energy profile, are sampled insufficiently. This sampling problem constitutes the main challenge in free energy calculations.
Several strategies exist to overcome this problem, such as thermodynamic perturbation, thermodynamic integration, umbrella sampling or biased calculations to name just a few. In the following sections the most important ones in the context of molecular adsorption will be introduced briefly.

3.4.1 Thermodynamic Integration

A rigorous approach to sample the free energy profile properly is to apply constraints which enforce the reaction coordinate to assume certain values along the reaction path.

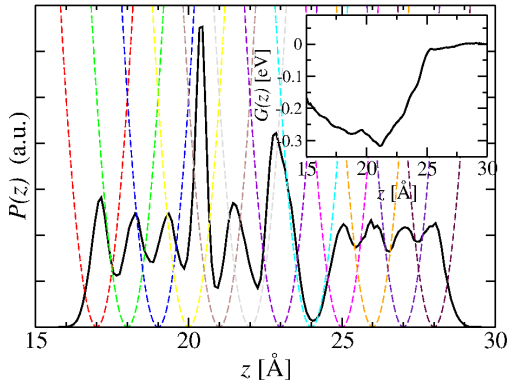

Figure 3.2: Combined probability distribution (*black solid line*) of a series of umbrella sampling simulations for the RGD-peptide on the oxidized titanium surface (cf. Chap. 5). The applied harmonic bias potentials are displayed by the *dashed lines*. The associated PMF is displayed in the *inset*.

Using Eq. 3.32 the free energy derivative in Eq. 3.33 can be written as

$$\frac{dG(\lambda)}{d\lambda} = -k_B T \frac{d \ln Z(\lambda)}{d\lambda} = -k_B T \frac{1}{Z(\lambda)} \frac{\partial Z(\lambda)}{\partial \lambda}$$

$$= \frac{1}{Z(\lambda)} \int d\boldsymbol{R} d\boldsymbol{P} \frac{\partial \mathcal{H}(\lambda)}{\partial \lambda} \exp(-\beta \mathcal{H}) \delta(\lambda - \lambda(\boldsymbol{R})) = \left\langle \frac{\partial \mathcal{H}(\lambda)}{\partial \lambda} \right\rangle . \tag{3.34}$$

Under the assumption of ergodic sampling, the derivative of the free energy equals the average of the derivative of the Hamiltonian, a quantity that can easily be evaluated in simulations. A series of simulations is carried out in each of which the reaction coordinate is constrained to a certain value of the reaction coordinate, thus spanning the entire range from initial to final state.

3.4.2 Umbrella Sampling

A different, probability-based approach is the so-called umbrella sampling method. Generally, the notion umbrella sampling comprises simulations with additional bias potential $V^{bias}(\lambda)$ that favors a certain region of the reaction coordinate. This way one obtains a biased probability distribution

$$P^{biased}(\lambda) = \exp[-\beta(G(\lambda) + V^{bias}(\lambda))] = P(\lambda) \exp(-\beta V^{bias}(\lambda)) . \tag{3.35}$$

Consequently, the unbiased probability is

$$P(\lambda) = P^{biased}(\lambda) \exp(\beta V^{bias}(\lambda)) \,, \tag{3.36}$$

which can be inserted into Eq. 3.31. In practice, one often uses harmonic bias potentials

$$V^{umbr}(\lambda) = \frac{1}{2} k^{umbr} (\lambda(\boldsymbol{R}) - \lambda_i)^2 \tag{3.37}$$

to restrain the reaction coordinate to a certain window around λ_i. A series of simulations with different values for λ_i spanning the reaction coordinate range of interest is then carried out and the resulting biased probability distributions are reweighted using the so-called *weighted histogram analysis method* (WHAM) [24, 101] to obtain the free energy profile. The WHAM technique involves an iterative determination of the additional constants G_0^i, until total free energy profile composed of the individual simulations assumes a continuous form.

The advantage of this method in comparison with thermodynamic integration is that the spacing of the sampling points λ_i can be chosen larger, as the harmonic potential allows exploring not only of the exact reaction coordinate value, but also of its vicinity. This decreases the number of simulations to be performed. The only strict requirement is that the histograms of adjacent windows have to overlap sufficiently.

As an example Fig. 3.2 shows the probability distribution of a series of umbrella sampling simulations of a peptide adsorbed on a surface. While the probability peaks for large reaction coordinate values, i.e. when the molecule is far from the surface, correspond exactly to the centers of the umbrella windows, in the transition region some probability peaks are shifted towards smaller z values, indicating a negative free energy change upon adsorption.

3.4.3 Metadynamics

Metadynamics provides another probability-based method which, at least theoretically, yields the exact free energy profile of one or more reaction coordinates [103]. In metadynamics the system starts from an unbiased equilibrium simulation and builds up the bias potential continuously during the simulation which in the end cancels the entire free energy profile. This means that the effective free energy profile which the reaction coordinate experiences, becomes increasingly flat and the motion of reaction coordinate becomes diffusive, preventing the system from being trapped in local minima. For this

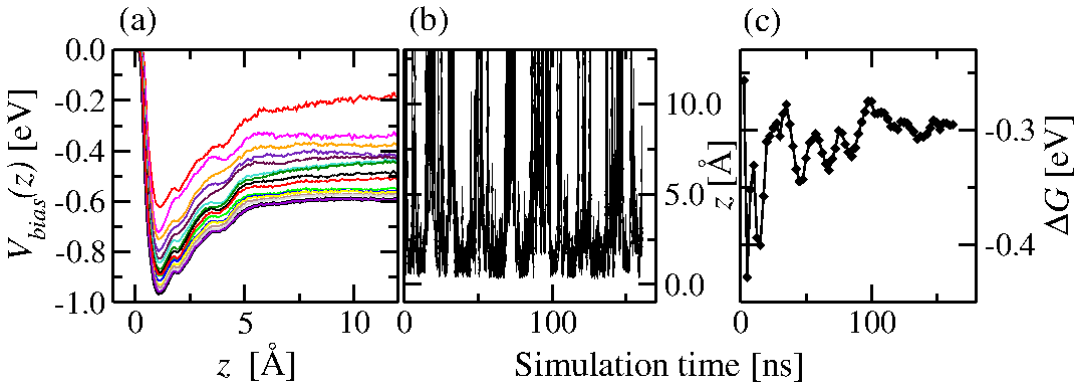

Figure 3.3: Convergence of the bias potential in a well-tempered metadynamics simulation(a) and the corresponding trajectory of the reaction coordinate (b) for the case of an amino acid side chain on the oxidized titanium surface (cf. Chap 6). The convergence of the integrated free energy difference ΔG according to Eq. 6.1 is displayed in (c)

purpose the bias potential is constructed in a way which repels the reaction coordinate from previously visited locations. In practice, a gaussian shaped hill is added, centered at every λ value that is assumed during the simulation:

$$V^{bias}(\lambda, t) = \sum_{t'<t} W_0 \exp\left[-\sum_{i=1}^{d} \frac{(\lambda_i - \lambda_i(t'))^2}{2\sigma^2}\right] . \tag{3.38}$$

The deposition takes place with a certain frequency. The probability to encounter the system in a minimum is higher than elsewhere, hence, a lot of gaussian hills are added around this location. As they increasingly fill the minimum, the bias potential eventually compensates the free energy well and allows the molecule to escape the trap.

The bias potential is time dependent which makes simple reweighting according to Eq. 3.36 impossible. However, in the end the bias potential effectively flattens the free energy surface, thus one can use its negative (modulo an additive constant) as an estimate of the free energy profile.

As the gaussian hills are continuously added during the simulation the bias potential does not exactly converge to a stationary form equal to the negative of the free energy profile but rather oscillates around it. For this reason the previous assumption remains an approximation. Nevertheless, one can obtain the exact profile from metadynamics, when the well-tempered ensemble is used [14]. In this scheme the height of a hill in Eq. 3.38

added at the time t is

$$W(t) = W_0 \exp[-V^{bias}(\lambda, t)/\Delta T] \,. \tag{3.39}$$

By choosing a suitable bias factor ΔT, the addition of new hills is exponentially switched off as the bias potential grows, so that $\partial V^{bias}/\partial t \to 0$ with $t \to \infty$.
At large times the bias potential grows slowly, allowing the system to maintain an equilibrated probability distribution $P(\lambda) \sim \exp[-\beta(G(\lambda) + V^{bias}(\lambda)]$. The deposition rate is then proportional to this distribution and one obtains [14]

$$\dot{V}^{bias}(\lambda, t) \sim W \exp\left[-V^{bias}(\lambda, t)/\Delta T\right] \exp[-\beta(G(\lambda) + V^{bias}(\lambda, t)] \,. \tag{3.40}$$

Ultimately, the condition that $\dot{V}^{bias}(\lambda, t \to \infty) \to 0$ for all λ-values requires

$$V^{bias}(\lambda, t \to \infty) = -\Delta T/(T + \Delta T) G(\lambda) \tag{3.41}$$

modulo a constant. The biased probability distribution in this case becomes

$$P^{biased}(\lambda) \sim \exp\left[-\frac{G(\lambda)}{k_B(T + \Delta T)}\right] \,, \tag{3.42}$$

which is obviously not completely flat but rather resembles the distribution at a higher temperature $T + \Delta T$, since the bias potential does not fully cancel the free energy profile.
The choice of the bias factor ΔT must balance mainly two aspects:
Low values of ΔT facilitate quicker convergence of V^{bias}, whereas high values improve the sampling of the reaction coordinate.
The time evolution and filling of the free energy surface is displayed in Fig. 3.3 for the case of an arginine side chain adsorbing on a titanium surface (as explained in detail in Chap. 6). To assess the precision, the convergence of the integrated free energy difference (according to Eq. 6.1 in Chap. 6) is displayed in (c). In this case the error of is estimated as 0.01 eV.

3.4.4 Replica Exchange Methods

The presented methods to obtain potentials of mean force for a one- or mulitdimensional reaction coordinate enhance only the sampling of phase space along this collective variables. For the remaining $3N - f$ (f being the dimension of the reaction coordinate) degrees of freedom, an exhaustive sampling of phase space cannot automatically be assumed. Considering e.g. the adsorption of a medium-sized molecule, such as a peptide on

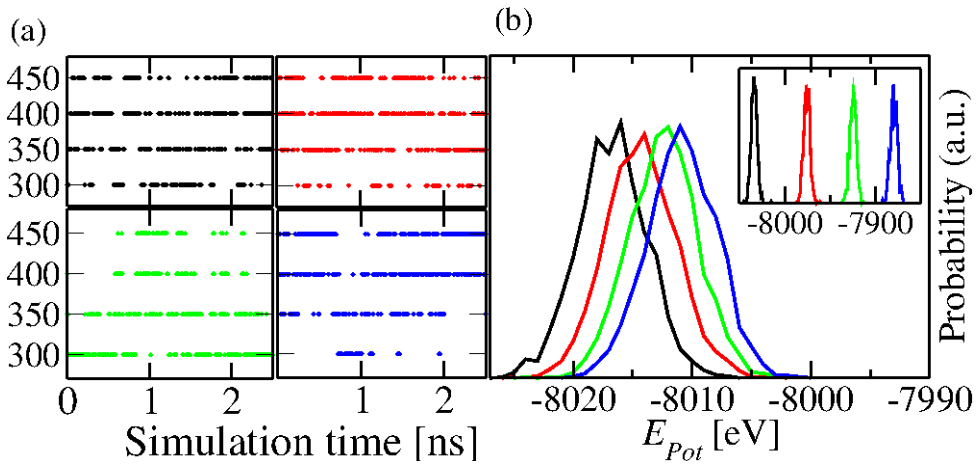

Figure 3.4: Section of the trajectories of the four replicas along the solute temperatures from a metadynamics+REST simulation (*a*). Distribution of potential energies for solute temperatures of 300K (*black*), 350K (*red*) 400K (*green*) and 450K (*blue*) (*b*). For comparison the *inset* displays the corresponding distributions when the same temperatures are applied to all degrees of freedom as in conventional RE. The simulations refer to the RKLPDA peptide on the oxidized titanium surface, cf. chap. 6

a solid substrate, where the center-of-mass distance to the surface represents the reaction coordinate one can obtain a potential of mean force along this collective variable using one of the methods described above. However, apart from barriers in this collective variable which are supposed to be handled by the chosen method of free energy calculation, other barriers, such as rotational barriers around peptide backbone torsion angles, exist As these are not directly associated with the reaction coordinate, their sampling is generally not taken into account by the primary sampling method in a controlled manner which can, in the worst case, exclude important molecular conformations from the potential of mean force calculation [133].

In order to overcome such problems, one can associate each degree of freedom, for which one expects significant barriers, with a reaction coordinate, increasing the dimensionality of the potential of mean force. Though excess degrees of freedom can be integrated out of the final free energy profile, not only the computational effort increases dramatically, also each individual barrier has to be identified separately which renders this method feasible only for small molecules. An alternative approach which takes care of sufficient sampling in a natural way without a bias potential, is provided by the *replica exchange (RE)*

technique [160]. In this approach possible free energy barriers are overcome at elevated temperatures, increasing the probability of barrier crossing according to the Arrhenius equation of activated processes $P \sim \exp(-\Delta G/k_B T)$, where ΔG denotes the height of the barrier. As, on the other hand, one is usually interested in the properties at room temperature, several replicas of the same system are simulated in parallel, each of which is assigned a certain temperature, spanning the entire range between room temperature and maximum temperature. From time to time neighboring replicas are allowed to attempt an exchange of temperatures which causes a wandering of the replicas in temperature space. Each attempt is accepted or rejected according to a standard Monte Carlo Metropolis criterion:

$$P(i \leftrightarrow j) = \exp[-(\beta_i - \beta_j)(E_j - E_i)] \tag{3.43}$$

Ideally, this leads to each replica diffusing from the bottom to the top temperature, where barrier crossing is facilitated, and back to room temperature (as displayed in Fig. 3.4 (a)). In this process the Boltzmann based acceptance criterion ensures a canonical distribution of configurations at each temperature. The base temperature trajectory can then be used to calculate various properties, such as free energies. While the replica exchange method was originally developed to merely enhance sampling of the phase space, it has been shown that its combination with other primary sampling techniques such as metadynamics can significantly improve the results, e.g. for the case of protein folding [30]. Regarding surface adsorption, a combination of RE with a fixed bias potential along the reaction coordinate as primary method has been reported [133].

One of the major drawbacks of replica exchange methods is that the potential energy distribution of neighboring replicas have to overlap sufficiently to ensure a reasonable acceptance ratio of the exchange attempts. As the relative width of the distributions decrease with increasing system size, one often has to employ a small spacing of temperatures which makes a large numbers of replicas necessary in order to reach sufficiently high temperatures for barrier crossing. This increases the computational effort in a dramatic, sometimes even prohibitive way. Different methods have been devised in order to increase the computational efficiency of RE simulations. As the difficulties arise mainly from solvent contributions to the potential energy which are usually not relevant compared to conformational transitions of the solute, different methods have been devised in order to reduce the influence of the heat capacity of the solvent. The *temperature intervals with*

global exchange of replicas (TIGER) method [111], for example provides an empirical approach to decrease the number of replicas, while maintaining a good acceptance ratio for the replica exchanges.

Another technique which appears particularly promising, as it resembles a canonical distribution while avoiding a large number of replicas, is the *replica exchange with solute tempering (REST)* method [114]. Here the temperature ladder is only applied to the solute molecule, whereas the solvent temperature is kept constant. By doing so, the heat capacity of the system is artificially reduced, causing the potential energy distributions of neighboring replicas to overlap even for a larger temperature spacing. This means less replicas have to be included which increases computational efficiency and at the same time the diffusion from bottom requires less intermediate steps and therefore takes place much faster. Considering the example of a hexapeptide adsorbed on a surface, the potential energy distributions from conventional and solute tempering (ST) simulations are compared in Fig.3.4 (b). While the ST distributions exhibit sufficient overlap, the energy distributions including all degrees of freedom into the tempering do not overlap at all.
As temperature, or more specifically thermal energy, is only defined relative to the potential energy, rescaling of the potential energy is equivalent to rescaling of temperature. Accordingly, selective tempering is achieved by only rescaling the intramolecular interactions of the solute, while keeping the total kinetic energy constant. At elevated temperatures the potential energy surface of the solute appears more shallow, consequently intramolecular barriers appear smaller and can be crossed easier with a probability $P \sim \exp(-\gamma\Delta E/(k_B T) = \exp(-\Delta E/(k_B T/\gamma)$ where $\gamma < 1.0$ is the scale factor. Due the fictitious nature of the solute tempering, the coupling of the solvent, i.e. the magnitude of its interactions with the solute, is somewhat arbitrary in this framework. Technical reasons suggest intermediate scaling factors. A factor of $\sqrt{\lambda}$ has appeared particularly favorable regarding electrostatic interactions [173], i.e. the potential energy of replica i is

$$E_i = \frac{T_0}{T_i} E_0^{mm} + \sqrt{\frac{T_0}{T_i}} E_0^{ms} + E_0^{ss}, \tag{3.44}$$

where m and s denote solute molecule respectively solvent, and the subscript 0 refers to the base temperature. In contrast to common replica exchange implementations, the Hamiltonian rather than the temperature is exchanged between the replicas.
Although the Metropolis criterion in principle yields an exact canonical ensemble, one has to keep in mind that enhanced sampling applies only to the degrees of freedom included

in the tempering. Barriers involving only solvent molecules, though, cannot be overcome by this method, which might, in some unfortunate cases, lead to a distribution of states deviating from the canonical ensemble.

Though promising and computationally feasible, this technique has only been applied to a small number of examples of molecules in solution so far [33, 85]. In this work we present for the first time the application of the metadynamics method combined with the REST technique to calculate adsorption free energies for medium-sized molecules with a considerable number of internal degrees of freedom.

Chapter 4

The Oxidized Titanium Surface

In this chapter I describe the first principle molecular dynamics (FPMD) simulations of the oxidation of the bare Ti(0001) surface, which were performed in order to construct the reference model for the oxidized titanium surface. I analyze the resulting structure, focusing in particular on the atomic charges. In section 4.2 the development of the classical force field is addressed, which is then applied in molecular dynamics simulations presented and discussed in section 4.3.
This chapter has been published in Ref. [149].

4.1 FPMD Modeling of the Oxidation of Ti(0001)

4.1.1 Computational Details

All simulations are performed within the formalism of the spin-polarized Density Functional Theory, using the PW91 exchange correlation GGA functional [137] and the PAW method [23] to represent the interactions between electrons and core ions, as implemented in the Lautrec code [183]. The PAW dataset for Ti is generated with 12 explicit valence electrons, including 3, 2, 2 projectors for the s, p and d angular momentum channels. The dataset for O includes 6 valence electrons and 2 projectors in each of the s and p channels. Both the minimization of the electronic states and the molecular dynamics simulations are performed using the Car-Parrinello (CP) method [34] on the basis of special algorithms developed to treat metallic systems [180, 159]. The wave functions are expanded in plane waves up to a kinetic energy cut-off of 540 eV, and the electronic states are occupied

according to a Fermi-Dirac distribution using a smearing width of 0.1 eV. As in previous simulations of the oxidation of Al [43], Si [44], and TiN [198] surfaces, no spin constraint is imposed during the dynamics.

The Ti(0001) surface is modeled by a periodically repeated $(2\sqrt{3}\times 3)$ surface supercell consisting of a slab of five (0001) layers of atoms in the xy plane, separated by a vacuum region of 11.64 Å in the z direction, corresponding to further five atomic layers. The surface cell is sampled using the (0.25, 0.25) point of the Brillouin zone. The atoms of the bottom surface layer, not involved in the oxidation reactions, are kept fixed during the dynamics. An electrostatic correction to remove the macroscopic dipole along the z supercell direction is applied to avoid spurious effects during the formation of oxide on only one side of the surface slab [131]. In all geometry relaxations we ensure that all force components on all unconstrained atoms are less than 0.05 eV/Å. Convergence of total energy differences with respect to the chosen cutoff is checked in all cases to be within 0.01 eV.

4.1.2 Oxidation Reactions

We perform FPMD simulations of the consecutive reactions of O_2 molecules placed one at a time above the Ti(0001) surface. Every simulation is concluded with a full relaxation of the atomic positions before placing a further oxygen molecule above the previously formed oxide layer and starting a novel simulation. No initial velocity is imposed to the incoming molecules, and the first nine simulations (up to a coverage of 1.5 ML of O) are performed within the microcanonical ensemble (without any temperature constraint). This thus represents 0 K conditions, except that a temperature of the oxygen gas allowing diffusion of the O_2 molecules to within ∼3 Å from the surface is implicitly assumed.

The first eight molecules spontaneously chemisorb to the surface and immediately dissociate according to the same "hot-atom" mechanism we already observed in the case of the oxidation of Al,[43] Si [44], TiN [41, 198], and Co/Cr surfaces [197]. For coverages below 0.5 ML, the O atoms remain adsorbed on top of the surface in hcp or fcc sites.

After adsorption of the third molecule, one O atom in a hcp site spontaneously binds to the underlying Ti atom of the first subsurface layer and occupies an interstitial position among the surface Ti atoms (Fig. 4.1 *(a)*). Further oxidation proceeds while Ti atoms leave the surface plane and O atoms are incorporated below the surface, with formation of an oxide network with a thickness of about 4 Å (Fig. 4.1 *(b), (c)*). At a coverage of

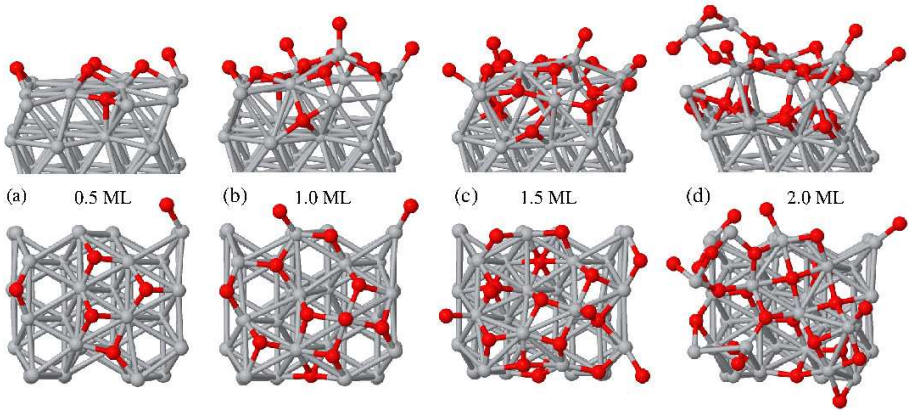

Figure 4.1: Selected final snapshots of consecutive FPMD simulations of the oxidation of the Ti(0001) surface, labeled with the correspondent oxygen coverages.

1.5 ML, the ninth O_2 molecule is able to chemisorb but not to dissociate spontaneously, indicating a reactivity decrease of the surface as found in other systems [41, 198], and the need for thermal activation for further oxide growth (Fig. 4.1 *(c)*).

In this first oxidation stage, the variation of the work function of the surface $\Delta\phi$ is found first to decrease slightly up to a minimum value of -0.17 eV (at a coverage of 0.67 ML), consistently with previous calculations [115]. Later $\Delta\phi$ suddenly increases, reaching a value of $+1.25$ eV at a coverage of 1 ML of O, and varying only little after the three subsequent chemisorption/dissociation events ($+1.28$, $+0.90$, $+1.32$ eV). The abrupt increase of the work function is associated to the extraction off the surface plane of a Ti atom which remains bound to three O atoms of the surface and one O atom "on top". This behavior is in good agreement with early measurements of $\Delta\phi$ performed during the oxidation of Ti(0001) at low oxygen pressures ($10^{-9}-10^{-7}$ Torr) and just above room temperature (100°C) [22], where $\Delta\phi$ was found to rapidly increase and stabilize at a value of $+1.25$ eV. A different behavior was observed in the same work during oxidation at higher temperatures (400 and 500°C), where $\Delta\phi$ is initially negative, presents a minimum of about -0.1 eV and becomes positive only at a later stage, eventually reaching stable values of about $+0.3$ eV. At the end of the oxidation process, the authors suggest that the oxide layer formed presents a composition close to TiO and that undissociated oxygen molecules remain adsorbed on the oxide structure. These could be removed by stopping the oxygen flux in the oxidation chamber, as indicated by a decrease of $\Delta\phi$ by about 20%

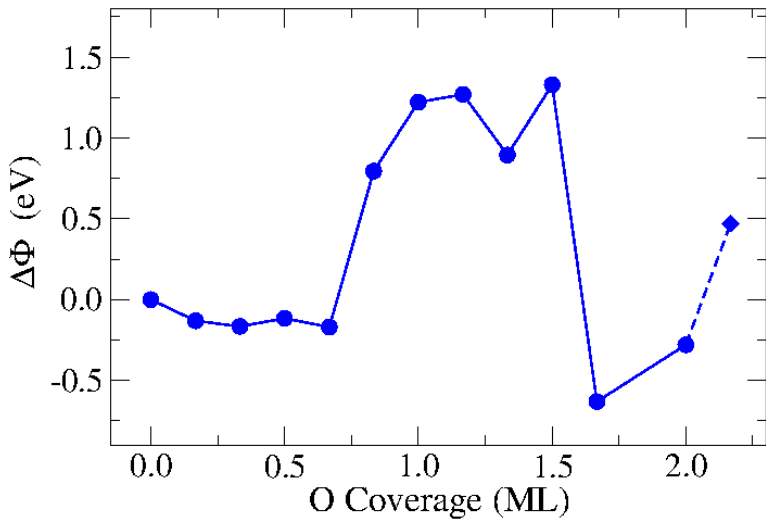

Figure 4.2: Computed change of the work function of the Ti(0001) surface after consecutive oxidation reactions as a function of the oxygen coverage.

concomitant with a decrease of the Auger oxygen signal.

These findings are consistent with the results of our further simulated oxidation reactions (above 1.5 ML of O), which we perform upon increasing the temperature of the simulation to a maximum of 800 K to promote oxygen dissociation and rearrangements of the O and Ti atoms within the oxide structure. Namely, after the thermally activated dissociation of further three oxygen molecules and the subsequent thermal annealing of the oxide structure (2 ML of O) at 1100 K for 3 ps, the computed $\Delta\phi$ is -0.28 eV. At the end of this simulation, the 24 O atoms form bonds to all (and only) the 24 Ti atoms belonging to the first and second surface layer, consistently with the TiO stoichiometry suggested in Ref. [22] (Fig. 4.1 *(d)*). Notably, the surface still presents sites where oxygen molecules could adsorb, and possibly dissociate spontaneously. In particular, after one additional molecule is placed chemisorbed over the oxide structure, it accepts electrons from the underlying surface, causing $\Delta\phi$ to increase again to $+0.47$, in qualitative agreement with the experimental evidence [22].

During typical oxidation experiments we can expect that the diffusion of Ti and O atoms may lead to thicker oxide layers than those obtained here, due to the severe time-scale limitation of the FPMD approach. However, the agreement of stoichiometry and work function values between our simulated structures and the available experimental

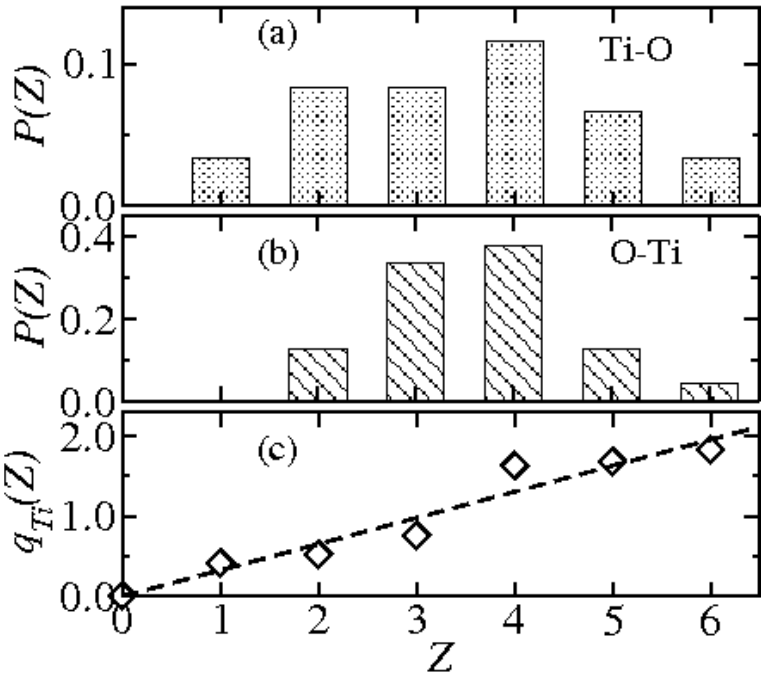

Figure 4.3: Probability distribution of the coordination numbers $P(Z_{Ti-O})$ (a) and $P(Z_{O-Ti})$ (b) (the value for $Z_{Ti-O} = 0$ corresponding to bulk Ti atoms is omitted for better visibility). Dependency of the Ti charges $q_{Ti}(Z_{Ti-O})$ on the number of O neighbors (c).

data is encouraging, and indicate that the former may indeed be seen as *representative models* for the ultrathin oxide layers which form on Ti(0001) at about room temperature.

4.1.3 Structural and Charge Analysis

In this section we analyze the thin layer oxide structure obtained in the quantum mechanical simulations described above. After completion of the oxidation reactions, the 12 titanium atoms of the topmost (0001) surface layer are completely incorporated in an oxide network. The second layer of Ti atoms retains its hexagonal order, except for the inclusion of one oxygen atom there within, so that the oxide scale is separated from the underlying metal by a clearly defined interface. The oxide layer presents a row of 3 exposed twofold coordinated bridging oxygen atoms, a characteristic feature of TiO_2 [107] and oxidized TiN surfaces [198].

Figure 4.3 *(a)* and *(b)* show the distribution of the coordination numbers Z_{Ti-O} and

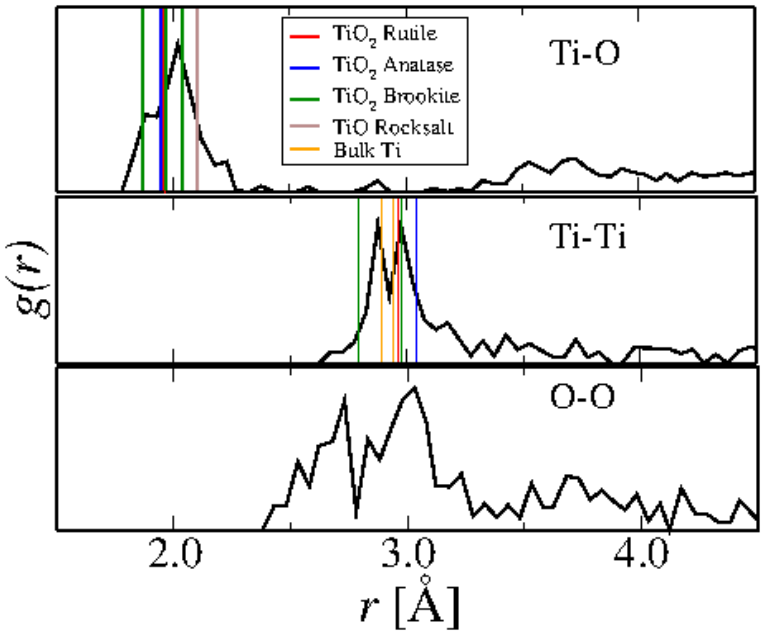

Figure 4.4: Partial radial distribution functions $g_{IJ}(r)$ for the oxidized titanium surface (black solid lines). The colored lines indicate the bond lengths in the TiO_2 crstal structures rutile (red), anatase (blue), brookite (green), Rocksalt TiO (violet) and in bulk hcp titanium (orange).

Z_{O-Ti} of the oxide O and Ti atoms. These are distributed between values 2 and 6 for oxygen (compared to $Z_{O-Ti} = 3$ for the TiO_2 crystals, $Z_{O-Ti} = 6$ for TiO crystals in the rocksalt structure and $Z_{O-Ti} = 4$ for Ti_2O_3 crystals in the corundum structure) and between 1 and 6 for titanium ($Z_{Ti-O} = 6$ for TiO_2, TiO and Ti_2O_3 crystals). On average, $\langle Z_{O-Ti} \rangle = 3.625$ revealing a slightly higher coordination of the oxygen atoms compared to crystalline TiO_2. Interestingly, the maximum probability for Z_{O-Ti} is found at a four-fold coordination of oxygen atoms, as in Ti_2O_3 corundum crystals.

The partial radial distribution functions $g_{ij}(r)$ for the 3 different atoms pairs, calculated taking into account only the 24 Ti atoms of the two topmost (0001) surface layers, are shown in in Fig. 4.4. For comparison, the nearest neighbors distances in the rutile, anatase and brookite TiO_2 crystal structures, of the TiO rocksalt structure [16] as well as bulk Ti are indicated by the colored lines. The first neighbor peak of g_{Ti-O} presents a main maximum and a smaller shoulder towards smaller distances, whose positions coincide well with the two bond lengths in brookite. The shoulder towards larger bond

lengths can be instead seen as a TiO-like feature. The positions of the two maxima in the first double peak of g_{Ti-Ti} coincides with the shorter bond length in bulk Ti and with the larger Ti-Ti distance in brookite structure. Moreover, the shorter Ti-Ti distances in the oxide layer are again roughly corresponding to the short brookite Ti-Ti length. The distances between oxygen atoms in the oxide layer exhibit a broad distribution, which does not allow for a reliable comparison with the crystal bond lengths. In general, the broad distance distributions are indicative of the predominantly amorphous character of the thin oxide layer, although the features in common with brookite, rather than rutile or anatase, are intriguing.

A very important aspect of our analysis is the distribution of charges among the atoms, which will form the basis for the optimization of a classical potential to describe the Ti/TiO_x interface possessing both analytic simplicity and a good degree of transferability. The Ti atoms of our interface system exhibit a broad range of oxidation states, from neutral atoms in the bulk metallic region to fully oxidized atoms in the oxide layer. Within the DFT formalism we calculate atomic charges from the electron density according to the "atoms-in-molecules" method (cf. Sec. 3.3.1). The resulting Bader charges are reported in the graph in Fig. 4.5. The atoms in the bulk metallic region (atom numbers 1-36) remain almost neutral, the subsurface metallic layer (37-48) is slightly positively charged with values around 0.5 e due to partial electron transfer to the oxygen atoms, and the charges of Ti atoms within the oxide layer (49-60) increase up to 2.0 e, depending roughly linearly on the oxygen coordination as shown in Fig. 4.3 *(c)*. All oxygen atoms (number 61-84) are negatively charged with values that vary only little around the average charge of $-1.22\,e$.

In order to compare the Bader charge distribution with that of a purely classical picture, we apply the electronegativity equalization method (EEM) of Mortier et al. [129]. Within this formalism the charges are calculated by minimizing the electrostatic energy under the constraint of charge neutrality. The electrostatic energy of a set of charged atoms can be written as

$$E^{es}(q_1, ..., q_N) = \sum_i \left[\chi_i q_i + \frac{1}{2} J_i {q_i}^2 \right] + \frac{1}{2} \sum_{i,j} \frac{q_i q_j}{r_{ij}} \,, \tag{4.1}$$

where r_{ij} are the distances between atoms i and j and the parameters χ_i and J_i are referred to as the atomic electronegativity and hardness, respectively. The first term of the equation can be considered the self energy due to partial ionization of the atoms, the

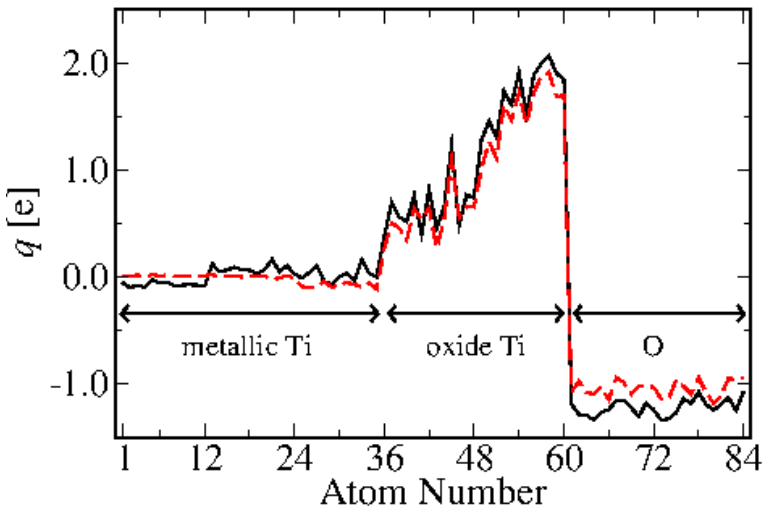

Figure 4.5: Bader charges q_i (black solid line) for each atom of the DFT model of the oxidized titanium surface along with the classical charges calculated using the electronegativity equalization method EEM (red dashed line).

second term the electrostatic interaction between different atomic sites. While the determination of the values for the parameters χ_i and J_i will be addressed in the next section, we anticipate here the good agreement between the Bader and EEM charges (shown by the dashed red line in Fig. 4.5). Although the modulus of the EEM charges is slightly smaller compared to the Bader charges, the charge distributions differ only by a constant of proportionality, revealing a good consistency between classical and quantum mechanical charges. This could have been indeed expected for fully oxidized TiO_2 allomorphes, which present a strong ionic character, but was not foreseeable a priori for the thin oxide layer including variable oxidation states of the Ti species.

4.2 A Classical Force Field for the Ti/TiO_x Interface

This section is devoted to the development of a classical force field to model Ti/TiO_x interfaces. Our main requirement for the force field is to be able to reproduce the structural stability of pre-existing structures, e.g. as obtained by quantum mechanical calculations, during MD runs at room temperature. Moreover, the form of the force field should be chosen so as to allow for quick and efficient adjustments of its parameters depending on local chemical variation of the modeled systems, as required in dynamical QM/MM calcu-

lations (for instance within the LOTF formalism [47]). This poses the problem of keeping the analytical potential form as simple as possible, while at the same time ensuring a good degree of transferability of the same form between different environments, such as between different crystal structures or amorphous oxides, and systems including variable oxidation states. In particular the variation of the atomic charges in the thin oxide layer will be a crucial point of our development, as described below.

4.2.1 Definition of the Potential Form

The hcp metallic region underneath the superficial oxide layer can be treated using a manybody potential suitable for metallic Ti. In this work we use a Finnis-Sinclair potential as proposed by Ackland [2]. Albeit simple, this FS potential is able to reproduce structural and mechanical properties of bulk Ti in a satisfactory way. In the Ackland approach, the energy of each metal atom is given by

$$E_i^{met} = \frac{1}{2}\sum_j V^{met}(r) f_c^{met}(q_i) f_c^{met}(q_j) - \sqrt{\tilde{\rho}_i} \tag{4.2}$$

where the sum runs over all atom indexes and

$$\tilde{\rho}_i = \sum_j \rho(r) f_c^{met}(q_i) f_c^{met}(q_j)\ . \tag{4.3}$$

The pair potential $V^{met}(r)$ and the density $\rho(r)$ are parametrized using cubic splines:

$$V^{met}(r) = \sum_k a_k (r_k - r)^3 \Theta(r_k - r)\ ; \tag{4.4}$$

$$\rho(r) = \sum_k A_k (R_k - r)^3 \Theta(R_k - r)\ , \tag{4.5}$$

where $\Theta(x)$ is the step function. In Eqs. (4.2) and (4.3) we have introduced cut-off functions

$$f_c^{met}(q) = \begin{cases} 1, & q < Q_{met} - \Delta \\ 1 - (q - Q_{met} + \Delta)/2\Delta, & Q_{met} - \Delta < q < Q_{met} + \Delta \\ 0, & q > Q_{met} + \Delta \end{cases} \tag{4.6}$$

that depend linearly on the atomic charges q. These cut-off functions ensure that the Ti-Ti FS interaction continuously decreases and is eventually switched off when the charges on the titanium atoms increase (i.e. by entering in the oxide region of a Ti/TiO$_x$ interface).

As far as the interactions within the oxide layer are concerned, the basis for their definition is the agreement between quantum mechanical charges and classical charges obtained by purely electrostatic arguments, as described in the previous Section of this paper. After replacement of the partial charges of common ionic force fields by these EEM charges, our finding suggests that Ti oxides, including non-stoichiometric ultrathin oxide layers, can be well described by using only electrostatic (Coulomb) interactions between the atoms, together with a short ranged two-body potential:

$$V_{ij}^{ox}(r) = \frac{1}{2}\sum_{i\neq j}\frac{q_i q_j}{r} + \frac{1}{2}\sum_{i\neq j} V_{ij}^{SR}(r)\cdot f_c^{ox}(q_i, q_j)\ , \tag{4.7}$$

where r is the distance between atoms i and j and

$$V_{ij}^{SR}(r) = A_{ij}\exp(-r/\rho_{ij}) - \frac{C_{ij}}{r^6} \tag{4.8}$$

is a Buckingham potential including dispersion and repulsive interactions. This is the same potential form that has been used by of Matsui and Akaogi (MA) to model TiO_2 polymorphs,[119] except for the cut-off function

$$f_c^{ox}(q_i, q_j) = 1 - f_c^{met}(q_i) f_c^{met}(q_j)\ , \tag{4.9}$$

if i and j both correspond to Ti atoms, whereas $f_c^{ox} = 1$ otherwise. This factor gradually switches off the oxide-related Ti-Ti interactions while entering in the metallic region of the system. Thus, our combined potential (equations 4.2 and 4.7) continuously changes from the metal region to the oxide layer and reduces to the Ackland potential or the MA potential form in the case of bulk Ti or bulk TiO_2, respectively.

4.2.2 Definition of the Potential Parameters

The original MA parametrization was developed to model bulk TiO_2 polymorphs and includes partial charges $q_{Ti} = 2.196$ and $q_O = -1.098$, the modulus of the latter being only slightly smaller than the Bader charges on O atoms as computed in the previous Section. Taking into account the previously highlighted correspondence between quantum and classical charges, we can adapt the MA parameters to model oxidized Ti surfaces.

Consistency with the original MA parametrization can be ensured by choosing the atomic parameters χ_i and J_i in Eq. 4.1 so as to obtain the q_{Ti} and q_O MA charges when minimizing the EEM electrostatic energy of the bulk TiO_2 rutile structure (see

Table 4.1: Values of the atomic electronegativity parameter χ_i and the atomic hardness parameter J_i used in the electronegativity equalization method.

	Ti	O
χ_I [V]	0.0	8.729
J_I [V/e]	12.864	17.197

Table 4.1). With this values of χ_i and J_i we can now compute the atomic charges for any arbitrary oxide structure, in particular containing multiple formal Ti valencies. As already mentioned in section 4.1.3 the EEM charges obtained for the oxidized Ti(0001) surface show very good proportionality to the corresponding Bader charges (see Fig. 4.5). Although the EEM parameters are commonly fit to atomic ionization energies rather than to ionic charges, the fact that the resulting charges are consistent with the Bader charges of the oxidized surface justifies our way of determining them, and enables us to use the original MA set of parameters also for the short-term potential (Eq. 4.8).

We have also tested an alternative parametrization, in which we choose not to include any dispersion interaction in the Buckingham potential ($C_{ij} = 0$ for both Ti and O) and to remove all non-Coulomb Ti-Ti interactions in the oxide ($A_{Ti-Ti} = 0$). The remaining parameters are obtained by a fit to the lattice and elastic constants of bulk rutile, again keeping the original MA values for q_{Ti} and q_O. In this case, the value of A_{Ti-O} are significantly higher than in the previous parametrization (see Table 4.2). This leads to steeper Ti-O repulsion and thus to a sharper potential minimum than in the previous case, as visible from the corresponding $V^{ox}(r)$ curves for 3 different charges $q_{Ti} = 2.196$, $q_{Ti} = 1.5$ and $q_{Ti} = 0.5$ (at constant oxygen charge $q_O = -1.098$) (Figure 4.6).

The interactions in the metallic region were again described by the FS-potential of Ackland, after adjusting the values Q_{met} and Δ to reproduce the DFT Ti-Ti and Ti-O bond lengths across the Ti/TiO$_x$ interface. As we will see below, with this additional parametrization the structure of the oxide layer obtained by FPMD is slightly better reproduced than in the previously described "MA-like" parametrization, and has the advantage of avoiding the calculation of a number of interactions.

Table 4.2: The two parameter sets for our Ti-O potential, and the parameter set for the FS Ti potential.[2] The lattice parameter for titanium was set to $a = 2.94$ Å. The values marked with * are the original MA parameters.[119]

Buckingham Potential						
	"MA-like" parameters			Alternative parameters		
	$\tilde{A}_{IJ}$ [eV]	ρ_{IJ} [Å]	$C_{IJ}[eV]$	$\tilde{A}_{IJ}[eV]$	ρ_{IJ} [Å]	$C_{IJ}[eV]$
Ti-Ti	31120.429 *	0.154 *	5.247 *	0.000	0.000	0.000
O-O	11782.847 *	0.234 *	30.222 *	85.164	0.489	0.000
Ti-O	16957.656 *	0.194 *	12.593 *	7211646.2	0.115	0.000
Charge dependencies						
Q_{met} [e]	0.8			1.45		
Δ [e]	0.1			0.25		
Finnis-Sinclair Ti Potential						
k	$A_k\,[eVa^{-3}\,2^{-3/2}]$	$R_k\,[a\,2^{1/2}]$		$a_k\,[eVa^{-3}\,2^{-3/2}]$	$r_k\,[a\,2^{1/2}]$	
1	39.795927	1.22		-57.099097	1.22	
2	-40.061305	1.05		80.735598	1.20	
3				-21.761468	1.12	
4				-10.396479	0.95	
5				74.515028	0.80	
6				35.921024	0.707107	

4.3 Classical Simulations with the Novel Potential

4.3.1 Computational Details

All classical Molecular Dynamics simulations are performed using the DL_POLY program [176]. The conjugate gradient (cg) method is applied for structural relaxation. The electrostatic interactions are calculated using the smoothed particle mesh ewald (SPME) method with a precision of 10^{-6} and a real space cutoff of 6.0 Å. The cutoff of the metal potential is set to $r_{met} = 5.0717$ Å as in [2]. For all other short-ranged forces we use $r_{cut} = 6.0$ Å. For simulations at constant temperature and volume the velocity-Verlet in-

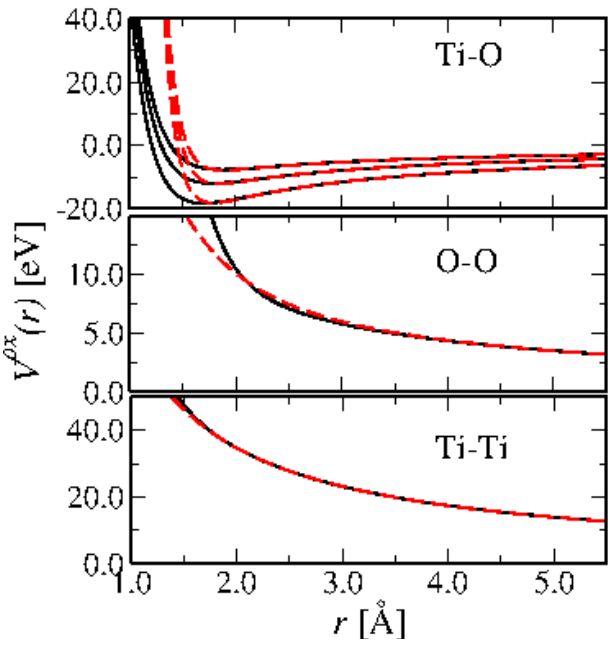

Figure 4.6: Interaction potentials V^{ox} for the 3 atom pairs according to equation 4.7. Comparison between the two MA-like (solid lines) and our alternative parametrization (dashed lines). The Ti-O interactions are computed with charges $q_O = -1.098$ and $q_{Ti} = 2.196$, 1.5 and 1.0 (bottom to top). The O-O and Ti-Ti interactions are computed with $q_O = -1.098$ and $q_{Ti} = 2.196$.

tegration algorithm is used with a timestep of 1 fs and the initial temperature is controlled by velocity rescaling. For simulations at constant pressure the Nose-Hoover scheme with thermostat and barostat relaxation times of 0.5 ps is employed.

For a given initial structure, the EEM charge equilibration is performed via the conjugate gradient method until the electrochemical potential $\mu_i = \partial E^{ES}/\partial q_i$ of all atoms converges with deviations of less than 0.1 V from the average value. The fitting of the potential parameters as well as the structural optimization and the calculation of the elastic properties of the TiO_2 crystals are performed using the GULP program package [61].

4.3.2 Transferability of the Classical Potential

Before using the potential described in Section 4.2 to simulate the oxidized titanium surface, we address in this section the transferability of our two parametrizations among different types of crystalline and amorphous Ti oxides and the rutile (110) surface. Al-

though we do not intend to use the potential to investigate the crystal properties of perfect systems, its ability to model various titanium oxide systems in a sufficiently consistent and reliable way is important.

Crystalline TiO_2 phases

For the three crystal structures rutile, anatase and brookite, the structural and elastic properties after relaxation both with the "MA-like" and the alternative parameter sets are reported in table 4.3 and compared with the available experimental values. The transferability of the MA potential to TiO_2 polymorphs has already been established in previous publications [119, 13, 79]. We find here that also the alternative parametrization leads to a reasonable agreement with the MA parametrization and with the experimental results.

The Rutile 110 Surface

Since we are ultimately interested in surface simulations, we test here the ability of the classical potential to describe the rutile (110) surface, which is modeled by a slab consisting of 6 atomic layers. We first relax the slab at the quantum mechanical level using DFT, and use the resulting structure as the input to compute the EEM charges on all atoms. With these charges (which differ on the surface atoms only slightly from the bulk MA-charges) we then relax again the surface slab using both parametrizations of our classical potential.

The displacements $\Delta z_i = {z_i}^{class} - {z_i}^{DFT}$ of each atom in the normal direction to surface with respect to the reference DFT structure are shown in Fig. 4.7. While the ability of a modified MA potential to model this surface has already been demonstrated by Bandura et al. [13], we find that our alternative parametrization leads to even smaller deviations (less than 0.2 Å) than the original parametrization (up to 0.5 Å). This holds in particular for the surface atoms (1-6), which are predominantly affected by relaxations with respect to their bulk positions.

Amorphous TiO_2

To construct a model for amorphous TiO_2 we randomly place 1000 titanium atoms and 2000 oxygen atoms in an tetragonal box with edges $L_x = 40.00$ Å, $L_y = 40.00$ Å and

Table 4.3: Properties of the different TiO_2 polymorphs after structural optimization with the two parametrization of our potential. The properties of the rutile structure were used for fitting the parametrization alternative to the "MA-like" one (see text). The properties of the amorphous TiO_2 are calculated at 300 K.

		"MA-like" set	Alternative set	Experiment
Rutile	a[Å]	4.50	4.62	4.594 [1]
	c[Å]	3.01	3.07	2.959 [a]
	B[GPa]	235.9	210.1	211.0 [2]
	C_{11}[GPa]	321.2	281.9	268.0 [b]
	C_{33}[GPa]	443.2	483.0	484.0 [b]
	C_{12}[GPa]	227.8	172.9	175.0 [b]
	C_{23}[GPa]	146.3	141.2	147.0 [b]
	C_{44}[GPa]	122.4	121.9	124.0 [b]
	C_{66}[GPa]	224.7	174.5	190.0 [b]
Anatase	a[Å]	3.77	3.81	3.785 [3]
	c[Å]	9.58	10.03	9.512 [c]
	B[GPa]	166.2	204.4	179.0 [c]
Brookite	a[Å]	9.15	9.33	9.174 [4]
	b[Å]	5.39	5.49	5.449 [d]
	c[Å]	5.15	5.34	5.138 [d]
	B[GPa]	198.8	204.5	-
Amorphous	ρ[g/cm^3]	4.03	1.93	3.50 [5]

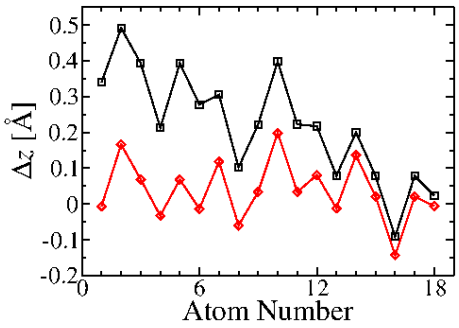

Figure 4.7: Relaxation of the rutile 110 surface (6 layers): Displacements Δz_i along the surface normal direction between the DFT structure and the structures minimized classically with the MA-like (black squares) and our alternative parametrization (red circles). For symmetry reasons only the displacements of the atoms belonging to the top 3 layers are displayed.

$L_z = 21.813$ Å, which corresponds to an initial density $\rho = 3.80$ g/cm^3. This system is annealed first at 5000 K for 100 ps, then for another 100 ps at 1000 K at constant volume. Afterwards we perform a series of 50 ps NPT simulations with zero pressure at 1000 K, 700 K, 500 K and 300 K. The structural properties are then averaged during a subsequent 100 ps run at 300 K. Additionally we relax the system at vanishing pressure, to obtain the density at 0 K.

Using the MA-like parameter set we obtain a density ρ of 4.03 g/cm^3 at 300 K and 4.07 g/cm^3 at 0 K, which lie between the experimental value of about 3.50 g/cm^3 measured for amorphous TiO_2 thin films,[123] and the density of 4.23 g/cm^3 of crystalline TiO_2. While at zero temperature the alternative parametrization yields still a realistic density of $\rho = 3.41$ g/cm^3 when starting from a system with an initial density of $\rho = 3.80$ g/cm^3, the density measured at 300 K decreases dramatically to 1.93 g/cm^3. Compared to the experimental results and to the results obtained with the MA parameters this value is significantly too low. Remarkably, the average Ti-O bond length is nearly the same for both potentials, whereas the number of such bonds is significantly smaller for the alternative parameter set.

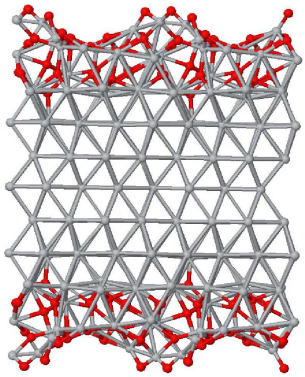

Figure 4.8: Input structure for the classical simulations.

4.3.3 Classical MD Simulations of the Oxidized Ti(0001) Surface

Stability of the Reference DFT Structure

In this section we investigate the ability of the developed classical potentials to reproduce the structural features of the thin oxide layer formed on Ti(0001) in the FPMD simulations. As the input structure for the classical simulations we use the final relaxed DFT model (Fig. 4.1 *(d)*) repeated twice in each of the x and y directions on the surface plane. In order to avoid a net dipole moment in the simulation cell, the DFT structure is symmetrically mirrored with respect to the bottom layer of titanium atoms along the z direction perpendicular to the surface. The resulting slab consisting of 432 titanium and 192 oxygen atoms is shown in Fig. 4.8.

The edges of the simulation cell are $L_x = 17.615$Å, $L_y = 20.34$Å and $L_z = 90.00$Å. After computing the EEM charges for the whole system, we first relax its structure with our novel potential using both parameter sets described earlier, and then perform 200 ps MD simulations at 300 K. The structures so obtained are analyzed with respect to their coordination number distributions and radial distribution functions.

After static relaxation, we observe that both potentials do not lead to any major structural changes. Importantly, the oxygen atoms do not diffuse inside the metallic region, and the sharp interface between the oxide layer and the metal substrate is conserved. Also the rows of bridging oxygen atoms on the outer surface side remain stable, although a small number of Ti-O bonds are broken and new bonds are formed inside the oxide layer.

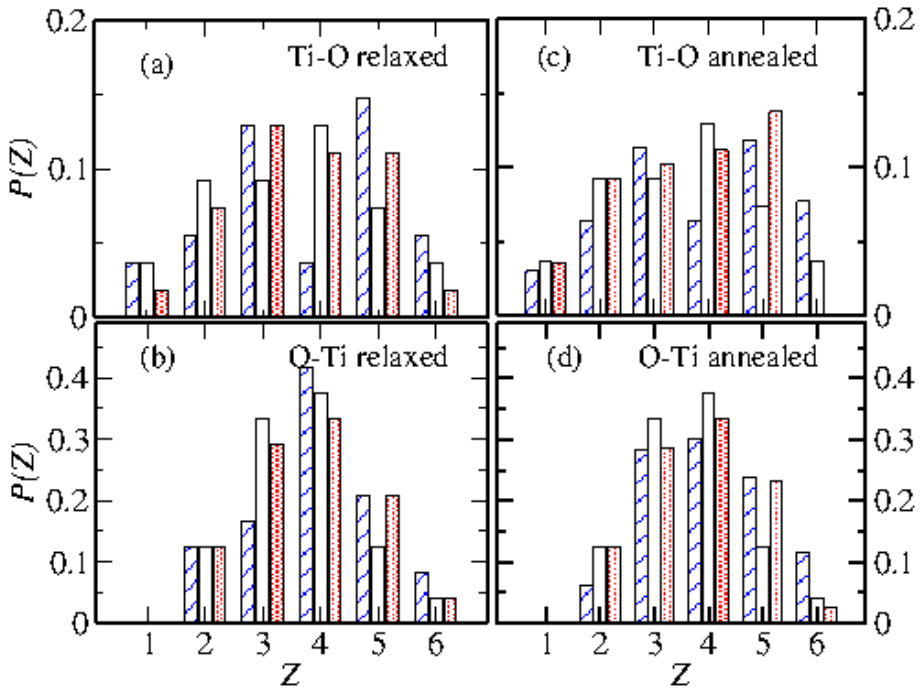

Figure 4.9: Distribution $P(Z)$ of coordination numbers Z_{IJ} for Ti (a) after relaxation and (c) after annealing at 300 K and oxygen, and for O (b) after relaxation and (d) after annealing at 300 K with respect to the other species. The bars correspond to the reference DFT model (empty), the MA-like parameterization (stripes) and our alternative parametrization (dots). The bars corresponding to $Z_{Ti-O} = 0$ are omitted for better visibility, as they overtop the other ones.

These little structural rearrangements can be investigated by looking at the distribution of coordination numbers $P(Z)$ of the first neighbors Z for the Ti and O atoms. The neighbors are counted within spheres of radius $R_c = 2.5$ Å centered on the atoms and $P(Z)$ is normalized to the total number of atoms of the respective species.

As shown in Fig. 4.9, the distributions resulting from the two classical parametrizations deviate only little from those of the DFT structure. In particular, the number of Ti atoms not bound to oxygen ($Z_{Ti} = 0$, not displayed) and the number of twofold coordinated O atoms ($Z_O = 2$) do not change, showing that no diffusion of O in the metal or breaking of the superficial bridging oxygen chains takes place, as mentioned above. Small changes are limited to atoms with higher coordination, revealing a general tendency of already oxidized Ti atoms ($Z_{Ti} = 4$ or 5) to become coordinated by 6 O neighbors. In general,

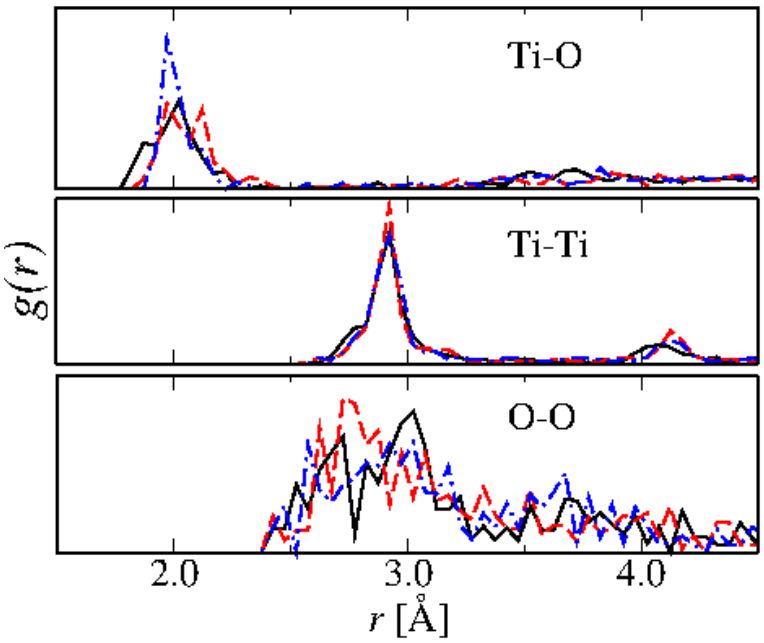

Figure 4.10: Partial radial distribution functions $g_{IJ}(r)$ for Ti-O (top), Ti-Ti (middle) and O-O (bottom) pairs: DFT reference model (solid lines), MA-like parametrization (dashed lines) and our alternative parametrization (dot-dashed lines).

our alternative potential parametrization produces a slightly better agreement with the DFT structure than the original "MA-like" one.

The partial radial distribution functions $g_{ij}(r)$ are shown in Fig. 4.10. Although little variations are present for all three kinds of atom pairs the distribution functions of the classical models agree well with the ones of the DFT structure. We only note that for the MA parameter set, the Ti-O distance distribution within the first neighbour shell reveals two peaks with a distance of about 0.15 Å to each other, whereas for the alternative parametrization the width of the peak is slightly reduced. For both classical models the shoulder towards smaller distances r, which contains mainly bonds between bridging oxygen and titanium atoms is not reproduced (a shortcoming which could in principle be corrected by adjusting the Buckingham parameters specifically for this particular atom pair, at the expense of simplicity and generality of the potential). The number of Ti-O bonds present in the oxide network can be calculated via integration of the first peak of $g_{Ti-O}(r)$ (using a cutoff distance $R_c = 2.5$ Å as for the $P(Z)$ distributions). While in the unit cell of the original DFT model (including 24 oxygen atoms) 87 Ti-O bonds are

present, 95 bonds are obtained after relaxation with the MA-like parameter set, and 90 bonds with the alternative parametrization.

The stability of the oxide structure is now investigated during MD simulations at room temperature. The MA-like parameter set leads to notable changes with respect to the relaxed configuration, particularly regarding the row of bridging oxygen atoms, which becomes partially incorporated into the oxide layer leaving a rather flat surface. These changes are visible from the $P(Z)$ functions computed before and after annealing (Fig. 4.9). A much better behavior is obtained using the alternative parameter set, for which the relaxed structure remains stable over the timescale of our simulations. However, if the simulation temperature is increased, dramatic changes of the oxide network topology take place, becoming visible after about 600 K. This reveals that our new potential parametrization is only applicable to room-temperature simulations.

Classical Generation of Thin-Layer Structures

In this Section we aim to produce superficial thin-layer oxide structures on Ti(0001) purely classically, using our developed potential in a *predictive* way. We first start with producing a system of bulk amorphous TiO_2 containing 96 titanium atoms and 192 oxygen atoms as described in Section 4.3.2. For this simulations we only use the MA-like parameter set, since the alternative parametrization failed to produce realistic amorphous TiO_2 structures. The edge lengths of the simulation box are chosen to be $L_x = 17.615$ Å and $L_y = 20.34$ Å in order to match the titanium surface cell. The box length in z-direction is set to $L_z = 9.35170$Å in order to maintain the experimental density of 3.80 g/cm^3 as measured in Ref. [79] The equilibrated structure is placed between the two free surfaces of a 7-layer Ti(0001) slab to create a Ti/TiO_2/Ti sandwich model. To equilibrate the Ti/TiO_2 interfaces we first anneal the model at 1000 K for 100 ps using MA charges in the oxide layer and no charges on the Ti atoms of the slab. The system is subsequently gradually cooled in two 100 ps MD runs at 700 K and 300 K, and fully relaxed. We finally compute new EEM charges for the whole model and relax the system again.

A thin superficial oxide layer is now obtained by cleaving the system in the central region of the amorphous TiO_2 slab, leaving 48 Ti atoms and 96 O atoms on each side of the titanium surface. The box length along the surface normal is increased to $L_z = 90.0$ Å inserting a vacuum gap between the newly created oxide surfaces. The cleaving of the oxide layer leaves a number of oddly coordinated atoms on the surface, in particular

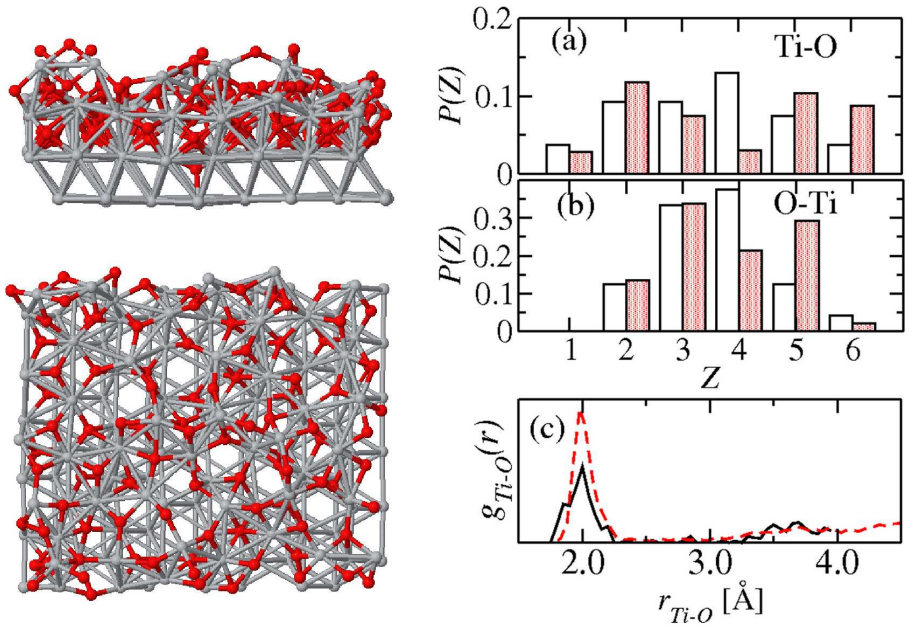

Figure 4.11: Left: Final structure of the oxidized titanium surface generated purely classically using the MA-parametrization. Right: Properties of this structure (dotted bars and dashed line) compared to the reference DFT model (empty bars and solid line). Distribution $P(Z)$ of the coordination numbers of titanium (a) and oxygen (b) atoms, radial distribution function $g_{Ti-O}(r)$ between titanium and oxygen atoms (c).

onefold coordinated O atoms that are not present in the quantum mechanical reference model. However, after an initial relaxation using the previously computed bulk EEM charges followed by two further iterations of EEM charge calculation and relaxation, all dangling bonds are healed. We now perform a final MD run annealing the system at 300 K for 250 ps, during which the topology of the oxide network remains stable, and fully relax the atomic positions.

The atomic composition and the size of the model obtained in this way (shown in Fig. 4.11) are identical to those of the previously investigated model, constructed directly from the DFT reference structure. The surface features 26 exposed bridging oxygen atoms compared to 24 present in the DFT reference model, and a sharp interface between oxide layer and metallic region. A total of 715 Ti-O bonds are present in the oxide network, corresponding to 89.4 bonds referred to the supercell used in the DFT simulations. This value is in very good agreement with the original DFT value (87 bonds) and the two

classically relaxed structures described earlier (92 and 90 bonds, see Section 4.3.3). We find some deviations of the Ti-O partial radial distribution function and of the distribution of coordination numbers (Fig. 4.9) from the DFT reference, which are more pronounced than in the systems analyzed in Section 4.3.3. In particular, a marked preference for 5-fold, rather than 4-fold coordination of both Ti and O atoms is found.

4.4 Summary and Discussion

In the present chapter we have performed a series of DFT Molecular Dynamics simulations of the oxidation of the titanium (0001) surface up to an oxygen coverage of 2 ML. Out findings regarding saturation of the oxygen uptake, work function analysis and stoichiometry are in good agreement with experimental results.

The final structure is amorphous and is separated from the metallic region by a rather sharp interface, also as a consequence of inhibited diffusion processes within the timescale accessible by our technique. The distributions of the bond-lengths and coordination numbers reveal features of TiO, TiO_2 and Ti_2O_3 crystals. Interestingly, the Bader charges variation within the obtained model can be reproduced classically with remarkable precision (within a proportionality factor), after calculation of charges by minimizing the electrostatic energy.

As presented in Section 4.2, the Ti/TiO_x interface can be modeled by combining a Finnis-Sinclair potential for the metal substrate with a potential form previously used by Matsui and Akaogi to describe TiO_2 allotropes [119].

Two parameter sets for the short-range contributions of the oxide force field are proposed and tested with respect to their transferability and their ability to keep the reference model stable upon relaxation and annealing at room temperature. Considering in particular the oxidized titanium surface, both parameter sets reproduce well the DFT reference model after static relaxation at 0 K. However, in dynamic simulations the MA-like parametrization fails to preserve the rows of twofold coordinated bridging oxygen atoms.

The reason why the alternative parameter set is particularly well suited to reproduce structures minimized at the DFT level, whereas it fails when applied to arbitrary oxide systems at higher temperature, is due to the shape of the Ti-O potential (see Fig. 4.6). The steep increase at small atomic distances leads, on the one hand, to rather sharp potential minima which maintain the stability of pre-optimized systems. On the other hand, this

causes a pronounced anharmonicity of the potential, which is likely to cause breaking of Ti-O bonds upon annealing and is responsible for an unphysically large thermal expansion of amorphous TiO_2.

Due to its better transferability to amorphous titanium oxide, the MA-like parametrization allowed us to create a model for an oxidized Ti surface in a purely classical way (see Section 4.3.3). Although the structural details of such model deviate quantitatively from the one obtained by DFT, overall the two models do not present severe differences. An advantage of this method might be the possibility of creating large models for surface structures which include *e.g.* steps and long-scale roughness and could be used instead of periodic replicas of the DFT supercell.

We note that during all structure relaxations and MD simulations we keep the EEM charges fixed to their values computed for the initial structure. However, since changes of the atomic coordination may take place during long MD runs, this method of dealing with the charges is *not* self-consistent. Another possibility would be to re-calculate the charges at every MD step (or at least with a certain frequency during the atomic motion). However, all our attempts of performing such self-consistent calculations did not lead to satisfactory results. In particular, small changes in the structure that emerge upon applying the classical potential cause further deviations of the charges, which in return lead to more pronounced structural rearrangements. This initiates a diverging loop and eventually leads to physically unrealistic situations. For instance, self-consistent charge updates during classical optimization of our DFT model resulted in O atoms migrating deeper and deeper into the metallic region and the creation of a Ti-terminated structure bearing no resemblance to the original model.

Although the results of our test are to be considered only as preliminary, we find that self-consistent charge transfer methods [162, 175, 69] in general tend to favor high coordination numbers of O atoms due to the large gain in electrostatic energy. This is not a problem for crystals or crystal-like structures, in which the coordination numbers are imposed by the regular arrangement of the atoms preventing structural changes during relaxation, but it becomes an evident deficiency in the case of heterogeneous systems with a broad distribution of coordination numbers, such as superficial ultrathin oxide layers.

Therefore, we conclude that these systems can be reliably modeled by using fixed charges, although this limits the predictive power of the potential and its ability to account for structural changes due to chemical reactions at the surface.

Finally, our point-charged based model not only preserves consistency with the original MA force field, but is also fully compatible with common force fields used to simulate liquid water and biological molecules as I will proceed to show in the next chapter.

Chapter 5

The Interface with Water

In this chapter I describe FPMD simulations of the interfaces between bulk water and both TiO_2 and the oxidized Ti(0001) surface. These calculations are used as a reference model for the construction of our potential in Sec. 5.2. In particular, I focus on an analysis of the charges of surface atoms and on how to achieve consistency with generic biomolecular force fields. I then proceed to derive appropriate non-bonded interactions and optimal parameters from DFT calculations of the PES of water and ammonia on the TiO_2 surface. In Sec. 5.2.5 I compare the classical model to DFT results of small organic molecules adsorbed on the dry oxidized surface. Subsequently, classical simulations of wet systems are presented and discussed in comparison to experimental results in Sec. 5.3. Finally, the adsorption behavior of the RGD-peptide on the oxidized titanium surface is investigated in Sec. 5.4.
This chapter has been published in Ref. [150].

5.1 FPMD Simulations of Water Adsorption

In order to obtain accurate model systems of the interfaces between oxidized titanium and bulk water we perform extended FPMD simulations based on DFT, comparing the water adsorption behavior on a rutile(110) surface with that on an ultrathin oxide film grown on Ti(0001). The computational details involved in these calculation have been described in Sec. 4.1.1.

5.1.1 Water Adsorption on Rutile TiO_2(110)

The dominant adsorption mode of water on the rutile TiO_2(110) crystal surface has been the subject of controversial discussions for decades. Theoretical studies have reported contradicting energetic orders for either molecular, mixed or dissociative adsorption at low water coverage ($\leq$1 monolayer) [113, 104, 15]. Regarding experimental results, spontaneous dissociation of water molecules on the perfect rutile (110) surface is generally considered to be unlikely, whereas it is facilitated at surface defect sites [53, 77, 190]. Recently, the change of free energy, rather than of potential energy, upon water adsorption was calculated in DFT MD simulations, yielding a positive value of +0.6 eV for the dissociation of bulk water on the perfect rutile 110 surface [37], which corroborates the experimental finding. Here we consider a 4-layer-slab of a 1×3 surface unit cell including 24 titanium and 48 oxygen atoms in contact with 21 water molecules. The dimensions of our supercell are 6.56×8.95×40.0 Å^3. By means of both dynamical simulations and static total energy calculations, we find that molecular adsorption at the fivefold-coordinated titanium atoms (Ti_{5f}) is the preferred way of interaction on the perfect TiO_2 rutile surface, in agreement with the Car-Parrinello MD studies of ref. [104]. In particular, when starting from an initially dissociated configuration with one of the protons bound to the neighbor bridging oxygen atoms, proton transfer and recombination of the water molecule eventually occurs within a few hundreds fs of dynamics. Direct Ti–O bond formation between water and the surface takes place exclusively at Ti_{5f} atoms with a coverage close to 100%. Namely, all three equivalent Ti_{5f} sites of our surface cell remain occupied by an adsorbed molecule for more than 90% of the time during the FPMD simulations at $\sim$350 K.

5.1.2 Water Adsorption on Oxidized Ti(0001)

Starting from the dry oxidized Ti surface, as described in chapter 4, we fill the vacuum gap with 28 pre-equilibrated water molecules and saturate the reactivity of the bottom surface of the slab with 12 hydrogen atoms in hcp positions, thus preventing spurious reactions between the water and the metallic slab. An FPMD simulation lasting 5 ps is carried out in the NVE ensemble, after initial thermalization of the system by velocity rescaling to a temperature of 350 K. During the dynamics, we observe adsorption, but not dissociation, of water molecules at exposed undercoordinated Ti atoms, similarly as on

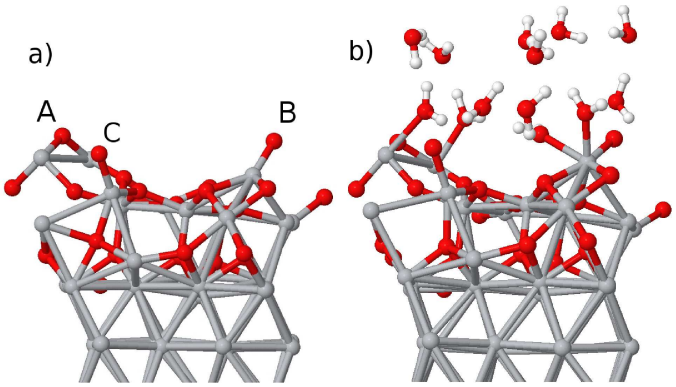

Figure 5.1: DFT model for the dry oxidized titanium surface (a) and snapshot of the interface between the surface and water from FPMD simulations (b).

the rutile TiO_2(110) surface. In the case of the thin oxide film, the preferred adsorption sites are the Ti atoms which are bound to the twofold-coordinated bridging oxygen atoms (which we will from now on refer to as *TiB* and *OB*, respectively). Once adsorbed, most of the molecules remain stably bound throughout the simulation. Only one molecule temporarily binds to a titanium atom located in the valley between the rows of bridging oxygen, and later desorbs leaving the site free. In summary, a total of 4 water molecules stably adsorb on the surface during our FPMD trajectory, occupying 3 of the 4 *TiB* adsorption sites, one of which accommodates two water molecules at the same time (Fig. 5.1 (b)). We calculate the desorption energies of these four water molecules from the total energy differences between the fully minimized water-decorated surface (in the absence of other free water molecules) and the same system upon removal of the adsorbed water molecules, once at a time, plus the total energy of the removed isolated water molecules in the same supercell. We obtain values of 0.53, 0.48, 0.91, and 0.44 eV. By comparison, for the desorption energy of a single water molecule from the fully hydrated 3×1 TiO_2(110) surface we find 0.83 eV.

In a further simulation, in which we started from a defective surface by removing one of the *OB* atoms, the adsorption of a water molecules takes place in a dissociative manner. One proton is transferred to a nearby bridging oxygen atom leaving a hydroxyl group adsorbed at the undercoordinated titanium atom. The corresponding calculated desorption energy value upon recombination of the dissociated molecule in the gas phase is 1.9 eV. Our computed values of desorption energy from the different sites agree fairly

well with the values measured experimentally for the desorption of water from a ∼100 nm thick oxide layer on Ti [106]. Namely, two main desorption peaks at 0.53 and 0.75 eV were identified and assigned to desorption of molecularly adsorbed water on different surface sites, while a third peak at 1.2 eV was assigned to associative desorption from previously dissociated water molecules.

These results suggest that our model, although based on a system of very limited size, may indeed be representative of realistic Ti/TiO_x/Water interfaces. We thus use it as a basis for constructing a classical potential which would enable us to simulate larger systems for longer time than achievable with a full quantum mechanical formalism. To this end, we rely on the fact that our oxidized surface, in the absence of obvious defects such as the oxygen vacancy that we arbitrarily created, showed little reactivity when exposed to liquid water. Therefore, we can assume that the physical/chemical behavior at the interface between oxidized Ti and the outer environment may be well captured by a simple potential based on non-bonded interactions, as described in the next section.

5.2 A Classical Potential for Ti/TiO_x/Water Interfaces

5.2.1 Computational Details

Apart from some modifications, as described in the following, we have employed the same basic simulation setup as described in Sec. 4.3.1. Due to the inclusion of Lennard-Jones potentials the cutoff for the short-ranged interactions has been increased. If not stated otherwise, a value of 12.0 Å is used. Dynamic simulations at finite temperature are performed in a NVT ensemble using the Berendsen thermostat [19] with a relaxation time of 0.5 ps and an integration timestep of 1 fs. The resulting surface areas of the oxidized Ti supercells comprise 17.62×20.34 Å^2 for the 2×2 surface and 35.23×40.68 Å^2 for the 4×4 surface. The central plane of titanium atoms is fixed to provide a constant reference coordinate frame. Before adding any adsorbate molecules, the dry surface is relaxed classically. The surface-water interface is prepared by filling the vacuum gap with pre-equilibrated water molecules. After relaxing and thermalizing the system, the height of the simulation cell is initially adjusted to obtain a 1 atm pressure along the surface normal.

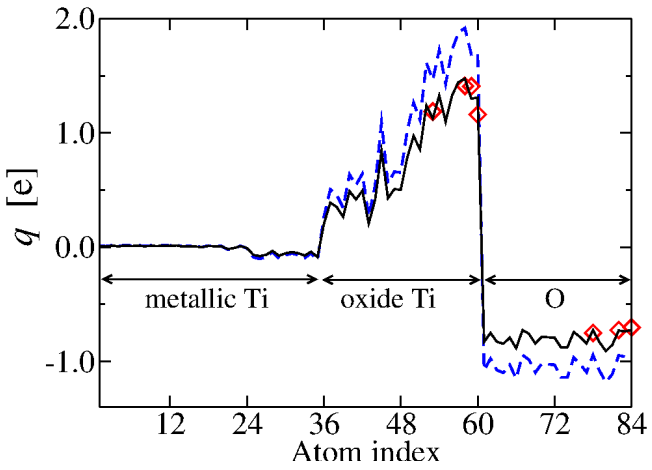

Figure 5.2: Charges of the dry oxidized titanium surface: Original EEM charges (*dashed line*), scaled EEM charges (*solid line*) and the ESP charges of the exposed surface atoms (*diamonds*).

5.2.2 Rescaling of the Point Charges for Surface/Adsorbate Interactions

In our potential, the point charges q_i employed in the electrostatic interactions within the oxide are determined using the electronegativity equalization method (EEM) of Mortier et al. [129]. Their values within the thin oxide film (dashed line in Fig. 5.2) are proportional to atomic Bader charges[12] computed at the DFT level, and are consistent with the parametrization of the short-ranged interactions. However, as explained in Sec. 3.3.1 these charges are not guaranteed to reproduce well the electrostatic interactions between the oxide layer and molecular species above the surface. Indeed, most common force fields for water or biomolecules, including the widely used TIP3P water model [89] or the AMBER [45] biomolecular force field, are based on electrostatic potential (ESP/RESP) derived charges (cf. Sec 3.3.1). We thus compute ESP charges for the exposed *OB* and *TiB* atoms (for atoms buried in the surface, the ESP charge value have little or no significance). As shown in 5.2, the obtained ESP charges are sightly lower than the EEM charges. Therefore, to compute the Coulomb electrostatic energy between molecular adsorbates and the oxidized surface, we rescale all surface point charges by a factor of 0.77, as determined ad hoc to match the EEM and ESP charges on the exposed surface bridging oxygen atoms (solid line in 5.2). Only to calculate the interactions between

the Ti and O atoms within the surface, we retain the original EEM charges in order to preserve the potential parametrization of Chap. 4 .

5.2.3 Interactions with Oxygen-containing Molecules

The finding of Sec. 5.1 that water adsorption on the defect-free oxidized Ti surface takes place without dissociation allows us to model the water/surface interactions by employing only electrostatic and non-bonded short-ranged forces. In this way, we can easily combine the potential described in the previous section with established biomolecular force fields in order to perform simulations of biomolecular adsorption on oxidized Ti, which is the ultimate goal of our work. We describe the interactions of the surface with adsorbates, in particular with water molecules, by a Lennard-Jones (LJ) and Coulomb non-bonded potential, as e.g. in the AMBER force field:

$$V_{IJ}(r) = \varepsilon_{IJ}\left[\left(\frac{\sigma_{IJ}}{r}\right)^{12} - 2\left(\frac{\sigma_{IJ}}{r}\right)^{6}\right] + \frac{q_I q_J}{r}\,, \tag{5.1}$$

The parameters ε_{IJ} and σ_{IJ} for each pair IJ of interacting species can be obtained using the combination rules $\varepsilon_{IJ} = \sqrt{\varepsilon_I \varepsilon_J}$ and $\sigma_{IJ} = (\sigma_I + \sigma_J)$ [45]. The atomic parameters ε_I and σ_I for water and biological molecules can be taken from the AMBER [45] or the generalized AMBER force field (GAFF) [186], which leaves only the 4 LJ parameters for the titanium and oxygen atoms of the surface to be determined. Differently from previous approaches (e.g. refs. [13, 155]), we determine these parameters from a fit of the energy landscape of water desorbing from a rutile TiO_2(110) crystal surface, rather than from optimization of the structural properties of adsorbed water molecules.

As a reference, we compute the potential energy surface (PES) of one water molecule placed at different heights above the fully hydrated 3×1 rutile (110) surface cell by means of DFT, as displayed in the inset of 5.3. Starting from a fully minimized configuration, one of the water molecules is displaced vertically along the surface normal and total energy calculations are performed at each separation, keeping all atomic positions fixed. The resulting PES is shown in 5.3 (black solid line), yielding an potential minimum of -1.1 eV. This is deeper than the desorption energy computed in Sec. 5.1 (0.83 eV) because of the lack of atomic relaxation.

For exactly the same atomic configurations, we now compute total energies using our classical potential, optimizing the LJ parameters for the surface atoms by a least squares fit to the DFT PES using the GULP package [61]. Both the DFT and the classical energy

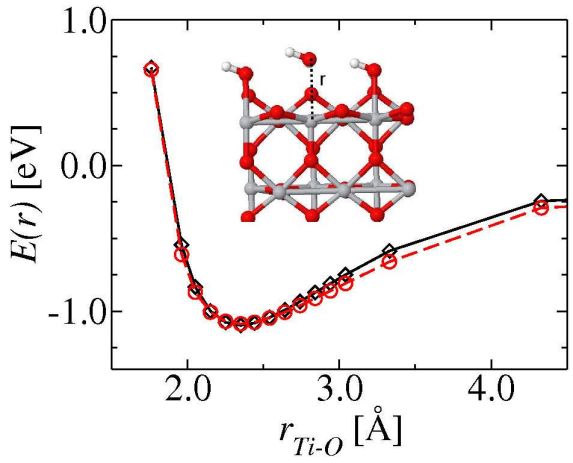

Figure 5.3: Potential energy surface (PES) of a water molecule at various separations from the TiO_2 rutile 110 surface: DFT (black diamonds) and classical calculations (red circles). The structure is displayed in the inset.

values are rigidly shifted to obtain a value of 0.0 eV for a water-surface separation of 8 Å. In these calculations, the point charges on the rutile atoms are computed from the EEM charges scaled by the same factor of 0.77 determined for the oxidized Ti surface (see previous section). Notably, the resulting charges are nearly identical to the ESP charges computed for the crystal surface (e.g. the average charge values of the bridging oxygen atoms are 0.67 electrons in both cases).

As shown in 5.3, the agreement between the DFT and classical PES is excellent for the optimal LJ parameter set listed in 5.1. We note that in our approach the used Lennard-Jones potential must not be seen as a physical representation of dispersion interactions, but only as an arbitrary way of mapping the true surface-water interactions by means of Coulomb and short-range terms. In fact, weak dispersion interactions are not properly accounted for, and generally underestimated [134], in the DFT total energy calculations. However, the deep minimum of the potential well on the polar oxide surface suggests that electrostatic attraction by far exceeds the dispersion forces, which can be thus safely neglected.

Using these interaction parameters, the water molecules are relaxed classically to compare the adsorbed geometry on the crystal surface to the corresponding DFT structure. Upon full atomic relaxation, at the classical level, the calculated desorption energies of a single water molecule from the hydrated surface is 0.81 eV, which is in very good agree-

Table 5.1: Lennard-Jones parameters of the surface atoms.

	Lennard-Jones-Parameters	
	ε_I [eV]	σ_I [Å]
Ti	0.01455	0.7827
O	0.01983	1.6154
	Ti-N 9-6 potential	
ε_{Ti-N} [eV]	0.140155	
σ_{Ti-N} [Å]	2.30769	

ment with the DFT value of 0.83 eV. We will indeed show later in this chapter that these parameters lead to computed values of the work of hydration of Ti oxide surfaces in good agreement with experiments, thus justifying the approximations taken in our approach. The distances between fivefold titanium and water oxygen, water hydrogen and bridging oxygen, as well as between hydrogen and oxygen of 2 neighbor water molecules are reported in 5.2. We notice small differences between the DFT and the classical structure, in particular the hydrogen bridges are longer in the classical model. However, we consider these differences as acceptable for our purposes and we refrain from correcting them *ad hoc* by introducing bending potentials [13, 155], as they would prevent the desorption of the bound water molecules from the surface, or their replacement by other water molecules. These are events that we often observed in long FPMD simulations, and that we would like to reproduce also in classical simulations.

Table 5.2: Interatomic distances of the DFT and the classical model after relaxation of the water molecules on the rutile 110 surface.

	DFT	Classical
Ti_5-OW [Å]	2.34	2.24
HW-OB [Å]	1.81	2.09
HW-OW [Å]	2.14	2.17

Another feature which should be captured by the potential is the correct adsorption energy of a second water layer, as discussed in Ref. [155] . To check this issue, we place

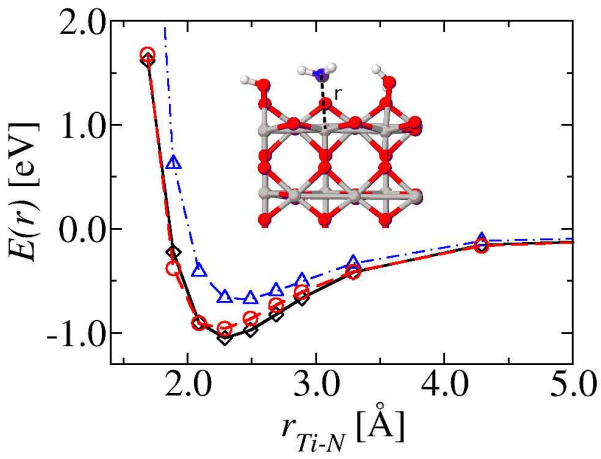

Figure 5.4: PES of an ammonia molecule at various separations from the TiO_2 rutile 110 surface: DFT (black diamonds) compared to classical calculations with original (blue triangles) and modified parameters (red circles). The structure is displayed in the inset.

an additional water molecule over the crystal surface terminated by 3 adsorbed water molecules, with the H atoms pointing towards the surface *OB* atoms. For this system we calculate the DFT and the classical PES as described above, obtaining adsorption energy minima of -0.14 eV and -0.12 eV for the DFT and the classical potential, respectively.

5.2.4 Interactions with Nitrogen-containing Molecules

Obviously not all molecules of interest bind to the surface via oxygen atoms, as in the case of water. It is thus necessary to check the transferability of the surface LJ parameters to the case of molecules adsorbing via different atoms, in particular nitrogen given its abundance in protein and other biomolecules. For this purpose we compute the adsorption of ammonia on the hydrated TiO_2(110) surface, as the simplest possible reference case. PES calculations are performed in the same way as described above, replacing only one of the water molecules by ammonia, while retaining the other two water molecules adsorbed on the surface. For the classical description of the NH_3 molecule, we use the Lennard-Jones parameters taken from the generalized AMBER force field. Since the AMBER force field does not specify partial charges for ammonia, we assign to the atoms ESP charges of -0.84 and +0.28, obtained by the same method as described in Sec. 5.2.2. Comparing the DFT and classical PES (5.4), it appears that the position of the energy minimum

determining the equilibrium bond-length is slightly shifted towards larger distances and especially the depth of the potential minimum is too shallow in the classical case. Notably, even trying a further optimization of the LJ parameter of the surface Ti and O atom did not lead to satisfactory results. Depending on the particular circumstances, this deviation from the quantum mechanical behavior can either be accepted as a limit of the parameter transferability, or a modification of the potential form must be introduced. In order to ensure a tight consistency with the DFT results, we chose to introduce an *ad hoc* 9-6-potential to model the interactions between N and Ti atoms:

$$V_{Ti-N}(r) = \frac{\varepsilon_{Ti-N}}{3}\left[6\left(\frac{\sigma_{Ti-N}}{r}\right)^9 - 9\left(\frac{\sigma_{Ti-N}}{r}\right)^6\right] \tag{5.2}$$

The parameters ε_{Ti-N} and σ_{Ti-N} are determined by fitting to the DFT PES, the resulting values given in 5.1. With this potential form, the DFT adsorption energy profile can be now very well reproduced (5.4).

5.2.5 Adsorption of Organic Molecules on the Dry Oxidized Ti Surface

In this section, we check whether the force field parameters determined in the previous section taking the TiO_2(110) surface as a reference are transferable to the case of adsorption of small organic molecules on the oxidized Ti surface. To this aim, the PES of methanol (CH_3OH), formic acid (HCOOH) and methylamine (CH_3NH_2) above the dry oxidized titanium surface are calculated both by means of full-level DFT and of our newly developed classical potential. For the reasons mentioned in Sec. 5.2.4 and for the sake of consistency, for all molecules we computed ESP charges with our DFT code. These are found to differ by less than 0.05 e from the corresponding point charges of the AMBER force field, when available. The LJ parameters of all atomic pairs are obtained by the standard combination rules, as described above. For each of the molecules, the minimum-energy adsorption geometry is obtained by FPMD simulations followed by careful relaxation. Taking the resulting structures as the input models, the molecules are displaced along the directions of the bond connecting them to the surface, and total energy calculations are performed without atomic relaxation. The relaxed adsorbed configurations are shown in 5.5.

In the case of formic acid, we found that the molecule could adsorb either in a molecular or in a dissociated form, depending on the initial orientation of the carboxyl hydrogen.

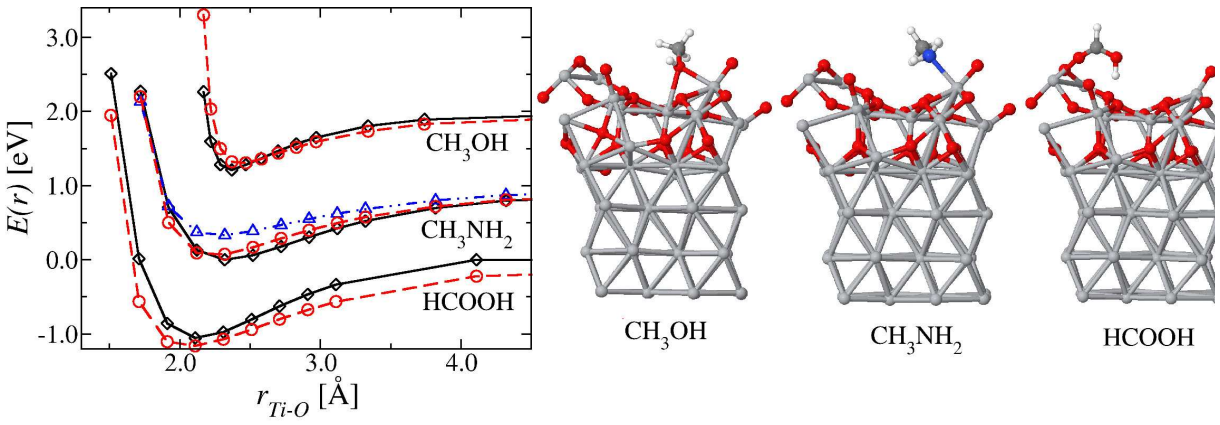

Figure 5.5: PES of methanol (CH_3OH), methylamine (CH_3NH_2) and formic acid (HCOOH) on the dry oxidized titanium surface: DFT (*black diamonds*) vs. classical energies (*red circles*). For CH_3NH_2 the results for unchanged (*blue triangles*) and modified (*red circles*) Ti-N interactions are displayed. For clarity the PES for CH_3NH_2 and CH_3OH are shifted vertically by 1.0 respectively 2.0 eV.

Since the dissociation reactions cannot be taken into account using our simple force field, we focus here on the molecularly adsorbed configuration. The OH group of methanol was found to bind to two titanium atoms, therefore the molecule was displaced vertically above the surface. Methylamine adsorbs with the N atom of the amine group bound to a *TiB* atom of the surface.

For methanol, the PES obtained with our classical potential agrees very well with the energies calculated with DFT (5.5), in the case of formic acid the classical energies slightly overestimate the DFT values by about 0.1 eV. For methylamine, we find excellent agreement between the two PES when including the modified 9-6 Ti-N interaction potential, whereas using the standard 12-6 LJ potential for Ti-N results in considerably lower adsorption energy, although the equilibrium bond-length is correctly reproduced.

5.3 Adsorption Behavior of Wet Systems

In the previous section, we have constructed a classical force-field potential which is able to reproduce the adsorption energy of small molecules both on crystalline TiO_2 surfaces and on the thin oxide film grown on Ti(0001). Here, we apply our potential

to investigate the behavior of interfaces between oxidized Ti and liquid water or fully solvated organic molecules. In particular, we take into account two representative cases for which quantitative experimental results are available, namely the heat of immersion of titanium oxide and the adsorption of single tyrosine molecules on oxidized Ti.

5.3.1 Heat of Immersion of TiO_x Surfaces

The heat of immersion of a surface, ΔH_{imm}, is defined as the energy gained upon placing the dry surface in contact with liquid water. In contrast to the case of e.g. the oxidized silicon surface, where water molecules are stably chemisorbed in a dissociative manner, mostly molecular adsorption and physisorption of water takes place on titanium oxide surfaces, as already mentioned in Sec. 5.1. As found in TPD experiments, the desorption temperature of these molecules is around or even below room temperature [77, 106, 128]. Therefore, the amount of surface water molecules which remain bound to the surface upon drying cannot be unambiguously identified, as this significantly depends on the conditions of preparation, in particular on the drying temperature [128]. Correspondingly, as ΔH_{imm} depends on the number of molecules already bound to the surface prior to immersion in liquid water, scattered values between 0.2 and 0.6 J/m^2 have been reported for TiO_2 crystals [68, 128, 51]. A linear decrease of ΔH_{imm} with an increasing amount on initially adsorbed water on the TiO_2 rutile and anatase surfaces has been obtained in Ref. [128]. Also in that study, however, the measured values scatter by as much as 0.3 J/m^2 for different investigated samples at the same initial water coverage, which makes possible only a rough comparison with theoretical investigations.

Here we start our study considering the interface between bulk water and a 6 layer slab model of the rutile TiO_2(110) surface including a 6×12 surface unit cell comprising an area of 35.23×40.68 Å^2. Similar to the findings from our FPMD simulations, in classical MD runs at 300 K we observe water molecules binding preferentially to Ti_{5f} atoms, where they remain stably adsorbed for large part of the simulations. The heat of immersion can be calculated by subtracting from the average potential energy of the wet surface E_W the average potential energy of the corresponding dry surface E_D and the potential energy of bulk water containing the remaining number of water molecules, E_B [39]. Starting from a 200 ps trajectory of the whole system with N_{tot} water molecules, these molecules are sorted with decreasing probability of being bound to the surface. The bulk water molecules are removed leaving only a certain number N_{ads} of molecules (according to

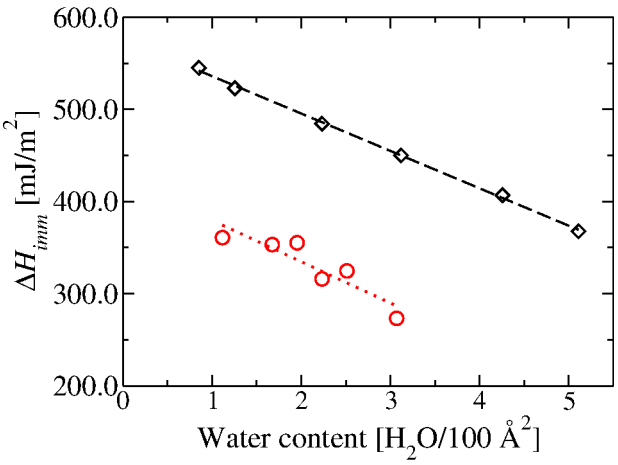

Figure 5.6: Heat of immersion for the TiO_2 rutile 110 surface (*black diamonds*) and the oxidized Ti surface (*red circles*) as a function of the water content. The straight lines are linear fits to the data.

their adsorption probability) on the surface. For these dry surfaces, simulation runs of 200 ps at a temperature of 300 K are performed to obtain the corresponding E_D average potential energies. From these values and the corresponding potential energy of bulk water containing $N_{tot} - N_{ads}$ water molecules, we calculate the heat of immersion as

$$\Delta H_{imm}(N_{ads}) = \left[E_D(N_{ads}) + E_B(N_{tot} - N_{ads}) - E_W(N_{tot})\right] / (2 * A_{Surf}) \ , \qquad (5.3)$$

where A_{Surf} is the surface area of only one side of the slab. The potential energies of the bulk water systems are calculated by first adjusting the height of each water cell in a 200 ps NPT run to obtain a pressure of 1 atm, followed by another 200 ps NVT simulation, in which the average energies were computed. A total number of 1188 water molecules is included as the liquid phase, and 'dry' surface systems with 24, 36, 64, 88, 120 and 144 pre-adsorbed water molecules are investigated. For $N_{ads} = 144$, all fivefold coordinated Ti of the rutile 110 surface atoms are occupied by water molecules.

The resulting dependence of ΔH_{imm} of the number of pre-adsorbed water molecules is shown in 5.6. In agreement with the findings of Ref. [128] , a perfectly linear decrease is obtained, and also the absolute values compare well with those available in the literature (between 200 and 600 mJ/m^2, see above). The slope of the linear regression is 0.25 eV/H_2O, which represents the desorption energy per molecule from the surface into bulk water. If we neglect the hydration of adsorbed molecules, the same quantity can be

calculated by adding the heat of vaporization of water (-0.45 eV for TIP3P water[89]) to the desorption energy into the gas phase (~ 0.8 eV, see above), obtaining 0.35 eV. A comparison of these two numbers gives an estimate of about -0.1 eV for the hydration energy of adsorbed molecules on the surface.

We note that our value of 0.25 eV only takes into account molecular adsorption, while dissociative adsorption events on defective crystal sites such as steps or edges are expected to be associated with larger energy values (of the order of 1.2 to 1.9 eV, see Sec. 5.1). This may explain the significantly larger value of 0.82 eV/H_2O reported in Ref. [128] for the case of rutile powder samples.

The heat of immersion calculated for the oxidized surface displays a slightly different behavior. In this case, we include 1520 water molecules in the liquid phase in contact with the 4×4 repetition of the DFT surface model, and performed 'dry' simulations for $N_{ads} = 32, 48, 56, 64, 72$ and 88. First of all, the obtained values are considerably lower than those for the crystal surface, as they range from about 260 to 380 mJ/m^2. They are closer to the value of 260 mJ/m^2 which has been reported for small TiO_2 nanoparticles [68]. Moreover, although a tendency of the heat of immersion to decrease upon increasing the pre-adsorbed water content can be identified, the values are scattered and no clearly linear dependence is observed. This must be attributed to the fact that, in contrast to the perfect rutile surface, not all adsorption sites are equivalent on the oxidized surface, as indicated also by the scattered values of the static DFT adsorption energies on this surface (cf. Sec. 5.1). The scattering could possibly be reduced by changing the order of removing the water molecules and thus averaging over the different adsorption sites. However, sampling of a large number of permutations would increase the computer time exceedingly, and lies beyond the scope of this work. Interestingly, fitting a linear function to the obtained values yields a to a very similar slope compared to the crystal surface.

5.3.2 Desorption Force of Tyrosine

As a further validation of the force field, we calculate the maximum detachment force of single tyrosine residues from the oxidized titanium surface. This has been measured by AFM force-spectroscopy experiments leading to a value of 97 ± 28 pN [108]. In our simulations, to exclude contributions from the backbone adsorbing to the surface we consider a reduced molecule consisting of a phenol ring bound to a methyl group. The intramolecular interactions as well as the LJ parameters and partial charges of the molecule are

taken from the AMBER force field, the charge value of the methyl carbon was adjusted to obtain a neutral molecule. After equilibration we then carry out a 39 ns classical MD run of the molecule on the oxidized surface at 300K, recording one snapshot every 500 ps. 78 of these snapshots were taken as independent starting configurations in subsequent umbrella-sampling runs. Such a large number of simulations yields reliable statistics for the force distribution, however, as a drawback, only the small 2×2 repetition of the DFT surface model could be used, to keep the computational cost reasonable. Due to the smaller cell size the cutoff radius for non-bonded interactions and for the real-space contribution of the electrostatic interactions had to be reduced to 8.0 Å.

Using a harmonic umbrella potential in the z direction normal to the surface applied to the carbon atom of the methyl group

$$V_{umbr}(z_c) = \frac{1}{2} k_{umbr}(z_c - z_{umbr})^2 \ , \tag{5.4}$$

with $k_{umbr} = 0.2$ eV/Å^2 and $z_{umbr} = 16.0$ Å (compared to $z \simeq 12$ Å for the exposed bridging oxygen atoms of the surface), the molecule was initially constrained to be close to the surface in a 300.0 ps simulation. In this representation, the $z = 0.0$ value refers to the central plane of titanium atoms, which are kept fixed. A steered molecular dynamics simulation (SMD) [88, 82] was then performed to mimic the experimental AFM setup, applying a time-dependent umbrella potential

$$V_{smd}(z_c, t) = \frac{1}{2} k_{smd}(z_c - z_0(t))^2 \ . \tag{5.5}$$

By choosing $z_0(t) = z_C(t = 0) + v_{smd} \cdot t$ the molecule is pulled off the surface at constant velocity. We set $v_{smd} = 0.5$ m/s and $k_{smd} = 0.1$ eV/Å^2. The instant pulling force $F(z_0) = k_{smd}(z_c - z_0)$ is recorded as a function of the pulling height z_0 every 5 fs. In order to eliminate large fluctuations, running averages of the force values over blocks comprising z_0 ranges of 0.025 Å are taken into account. In this way the short-time fluctuations are found to decrease considerably, whereas the actual force-displacement-curve, which varies on a larger timescale, is not affected significantly.

A representative example of a force-displacement-curve is shown in 5.7. Initially the adhesion force increases roughly linearly until eventually a sudden decrease is visible, which reflects the detachment of the molecule from the surface. We calculate the peak forces for a total number of 73 simulations, their distribution is displayed in a histogram in 5.7. In five cases no clear force peak could be identified, indicating that the molecule was not

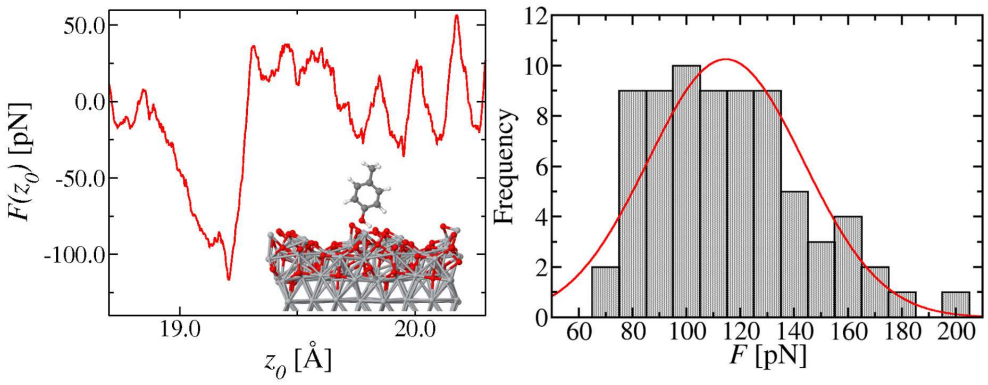

Figure 5.7: SMD simulations of tyrosine on the oxidized surface. *Left*: Example for a force-displacement-curve $F(z_0)$. *Right*: Histogram of the maximum desorption forces and gaussian fit to the distribution (red line).

adsorbed at the beginning of the simulations (more precisely, we did not consider peaks smaller than 60 pN, which correspond to the fluctuations of the pulling force acting on a free, solvated molecule dragged through bulk water). These simulations were discarded and not considered in the histogram. Considering the trajectories of the individual simulations, we note that the adhesion to the surface is in general mediated by hydrogen bonds between the hydroxyl group of the phenol ring and surface oxygen atoms, as assumed in ref. [108]. Moreover, in some cases the hydroxyl oxygen is observed to bind temporarily to one *TiB* atom after displacement of an adsorbed water molecule, leading to the values on the shoulder towards larger forces in the distribution. In summary, our computed forces range from 70 to 200 pN. A gaussian distribution fit to the values yields an average force of 108 pN and a width of 31 pN. Within this variance the average force value agrees well with the experimental results of ref. [108] (97 ± 28 pN). Therefore, we feel that our interaction potential can be reliably applied to investigate new systems, for which the experimental understanding is still incomplete, as performed in a representative case in the next section.

5.4 Adsorption of RGD Peptides on the Oxidized Ti Surface

Finally, as a first application of the developed force field, we present simulations of the arginine-glycine-aspartic acid (RGD) peptide sequence adsorbing on Ti. This sequence is present in proteins building the extracellular matrix, such as fibronectin and collagen, where it acts as an integrin binding site and plays an important role in the process of cell adhesion [144]. Since such peptides are used to functionalize the surfaces of metal implants to enhance bone cell adhesion [193, 141], an interesting aspect is their direct adsorption behavior as this competes to binding to integrins. Despite its importance, only few simulation studies are devoted to the investigation of the adsorption of RGD-sequences on solid state surfaces, particularly on crystalline titanium oxide [112, 157, 192].

Here we perform umbrella sampling simulations to obtain force-displacement profiles from which the potential of mean force (PMF) and the free energy of adsorption can be calculated. In order to avoid charged end groups, the molecule is terminated with NME (CH_3NH-) and ACE (-$COCH_3$) sequences, yielding a NME-ASP-GLY-ARG-ACE peptide. The peptide is completely modeled using the AMBER force field, including its partial charges. For similar reasons as stated in Sec. 5.3.2 we consider a 2×2 surface area and use a cutoff radius of 8.0 Å. After pre-equilibrating and adjusting the cell height, the system is annealed at 450 K for 200 ps (keeping the surface atoms fixed) to overcome possible adsorption barriers to the surface, followed by another annealing at 300 K for 300 ps. The resulting configuration, which is shown in 5.8 (c), is used as initial model for our free energy calculations.

The RGD molecule binds to the surface via the arginine side chain, which is able to penetrate the first layer of water molecules in the valley between two rows of bridging oxygen atoms. The interaction with the surface is mediated both via hydrogen bonds between the guanidinium group and surface oxygen atoms and via electrostatic interactions between nitrogen and titanium atoms. The ASP side chain is also oriented towards the surface, with the carboxyl oxygen atoms forming hydrogen bonds with the ARG side chain and with surface water molecules.

In the umbrella sampling simulations, as the reaction coordinate we chose the z-position $z_{C\alpha}$ of the alpha carbon of the central glycine residue, with a zero offset corresponding to the position of the central plane of the surface slab (as described in Sec.

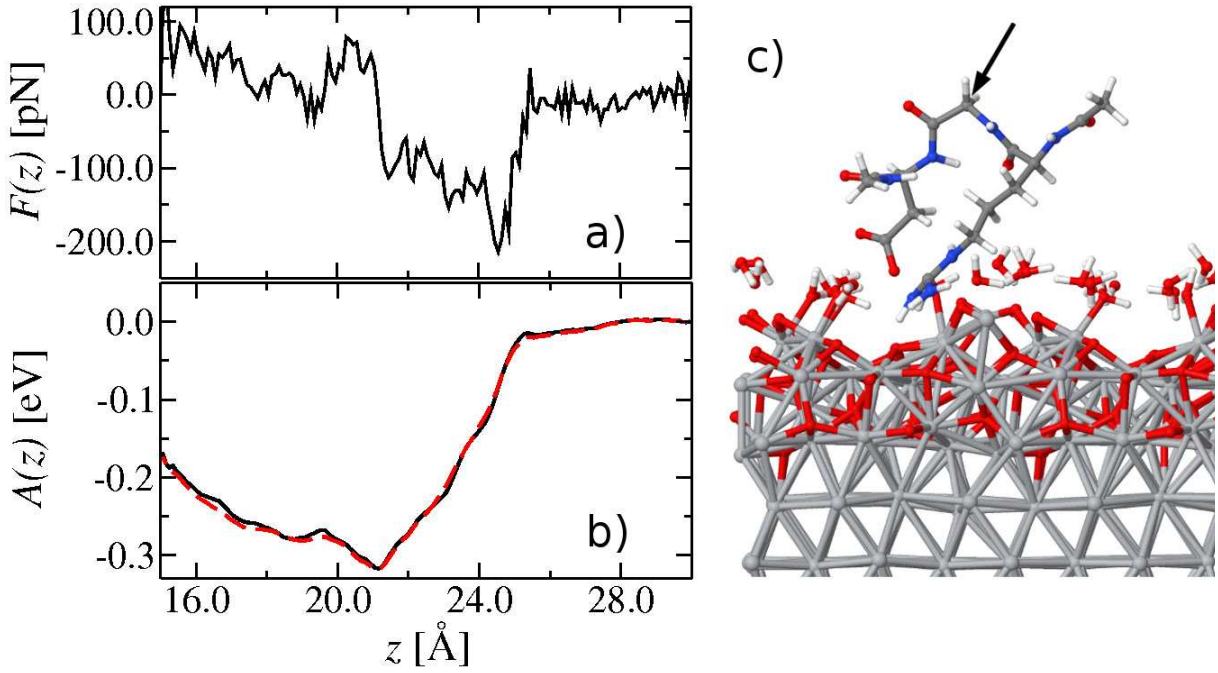

Figure 5.8: Desorption of the RGD-containing peptide from the oxidized Ti surface: Force profile (a), free energy profile obtained by WHAM (*solid line*) and TI (*dashed line*), and snapshot of the initial adsorbed configuration (c). For clarity, only the first layer of water molecules is displayed. The arrow marks the glycine alpha-carbon atom.

5.3.2). The reaction coordinate is then increased stepwise from 16.0 to 29.0 Å and restrained to a total of 14 windows with 1.0 Å width by a harmonic potential (see Eq. 5.4) with a force constant $k_{umbr} = 0.2$ eV/Å^2. For each window a simulation run of 1.2 ns is performed, where the first 200 ps are discarded from the force analysis. The reaction coordinate and the z-component of the force acting on it are recorded every 5 fs.

To calculate the free energy profile $A(z)$ we employ two conceptually different methods, namely (i) the weighted histogram analysis method (WHAM)[101], evaluating the probability using the code of Grossfield [67], and (ii) the potential of mean force (PMF) as obtained by thermodynamic integration (TI) of the average force[49, 178]

$$G(z) = \int_{z_{max}}^{z} \langle F(z') \rangle dz' \ . \tag{5.6}$$

The unbiased force is obtained by performing the average over all umbrella windows and

correcting the value by the respective umbrella force:

$$\langle F(z)\rangle = \sum_{i=1}^{N_{umbr}} \frac{n_i(z)[\langle F^i_{biased}(z)\rangle + (d\,V^i_{umbr}(z)/dz)]}{n_{tot}(z)}\,, \tag{5.7}$$

where the i indicates the respective umbrella window, $n_i(z)$ gives the number of appearances of a reaction coordinate value of z from umbrella window i and $n_{tot}(z) = \sum_i n_i(z)$ yields the total number of counts for the value z. The forces, the probability and the corresponding free energy profile are collected in bins of 0.1 Å width.

The unbiased force profile $F(z)$ is displayed in 5.8 (a). When increasing the z_0-value of the umbrella center, first the sidechain of the ASP residue is detached from the surface due to its shorter length compared to ARG. Finally the guanidinium group of the ARG residue desorbs producing a force peak of about -215 pN at a z-value of 24.5 Å in the force profile. The free energy profiles calculated with the two methods are shown in 5.8 (b). Importantly, we note that the two curves agree almost perfectly with each other, giving a strong hint that the force calculations and the reaction coordinate sampling have reached convergence. In the free energy profile we observe a minimum depth of 0.32 eV. In analogy to Ref. [133] the free energy of adsorption ΔG_{ads} can be calculated as

$$\Delta G_{ads} = -k_B T \ln \frac{c_{ads}}{c_{bulk}}\,, \tag{5.8}$$

where

$$c_{ads} = \frac{1}{z_0 - z_{min}} \int_{z_{min}}^{z_0} \exp(-\beta G(z))dz\ ,\ c_{bulk} = \frac{1}{z_{max} - z_0} \int_{z_0}^{z_{max}} \exp(-\beta G(z))dz\,, \tag{5.9}$$

and z_0 defines the border between adsorbed and desorbed region. Applied to the PMF displayed in Fig. 5.8, a value of $\Delta G_{ads} = -0.26$ eV is obtained. Experimental values for the binding free energy between RGD-containing peptides and integrin proteins in the absence of a surface are found to be in the range of 0.16 eV [109], whereas simulations of such a situation yield a binding free energy of 0.13 eV [38]. Hence, when a titanium surface is functionalized using RGD-containing peptides, a situation might arise where adsorption on the surface is in competition with the desired process of binding to integrin molecules. From a comparison of the respective free energy values we can conclude that the adsorption of RGD on the oxidized titanium surface is considerably stronger and might thus limit the functionality of the sequence. Therefore, immobilization via appropriate spacers, such as specific binding peptides [95] where direct adsorption of RGD at the titanium surface is less likely, should be preferred over non-specific surface adsorption to enhance cell adhesion via binding to integrin.

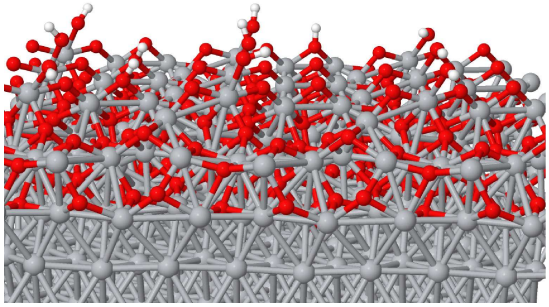

Figure 5.9: The charged oxidized titanium surface with hydroxyl groups and protonated bridging oxygen atoms.

5.5 Development of a Charged Surface Model

Having established its general reliability, in the following we will show how the surface model can be augmented towards a more realistic description.
Titanium surfaces with a superficial oxide layer generally exhibit isoelectric points between 5.0 and 6.0 [26, 99, 121], implying that both negatively and positively charged surface terminations exist . Even if our FMPD simulations of water on the oxidized titanium surface showed only molecular adsorption, one would ultimately expect dissociation of water molecules for two reasons: First, as known from the literature [190, 104] and from our FPMD simulations (cf. Sec. 5.1), spontaneous dissociation is favored in the presence of surface defects such as oxygen vacancies, which one must always assume to be present on experimental substrates. Second, the dissociation of adsorbed water molecules is an equilibrium reaction, which is accompanied by a free energy change of about +0.6 eV [37]. To encounter such an event in a few ps of FPMD simulations is thus highly unlikely, whereas on experimentally accessible time scales one would ultimately expect an equilibrium of molecular and deprotonated water molecules as well as protonated bridging oxygen atoms.

Based on these considerations we have decided to include charged surface sites to our model employing a scheme similar to the one proposed by Predota et al. [139] for the charged rutile surface: A certain fraction of the adsorbed water molecules is deprotonated and protons are added to some of the bridging oxygen atoms. As the isoelectric point is in the acidic range, an overall excess of negatively charged sites must be maintained,

the exact ratio between $TiOH^-$ and Ti_2OH^+ groups is chosen to be 16:5, which leads to a surface charge of -0.123 C/m^2 close to the experimental value of -0.13 C/m^2 [165]. The resulting surface model is displayed in Fig. 5.9 In agreement with DFT ESP charge calculations, the charges of the dissociated water molecules are taken to be identical to the charge values of the TIP3P water model. As this procedure yields only a charge magnitude of ± 0.417 e for a positive respectively negative group, the difference to the actual protonation/deprotonation charge of ± 1.0 e has to be accounted for in a reasonable way. DFT calculations show virtually no difference in the Bader charges as well as in the ESP charges of the exposed surface atoms between the neutral surface and surfaces with $TiOH^-$ or Ti_2OH^+ terminations, which implies that the charge is rather delocalized, probably due to metallic titanium region below the thin oxide layer. We therefore distribute the excess charge of $[N(Ti_2OH^+) - N(TiOH^-)] \times 0.5823$ e equally among all atoms belonging to the oxide layer.
Regarding the Lennard-Jones coefficients for hydroxyl oxygen and hydrogen atoms we use the same values as given in the TIP3P water model. Assuming the hydroxyl groups to be chemisorbed at the surface, we model the bond between the hydroxyl oxygen atom and the connected titanium by a harmonic potential. In order to reproduce the DFT geometry a bending potential is introduced, whose parameters are adapted from Ref. [139].

5.6 Summary and Discussion

In this chapter, we have presented an extension of the classical force field developed in Chap. 4 to model the interactions between natively oxidized titanium surfaces and liquid water as well as solvated biomolecules. The interactions across the solid/liquid interfaces comprise Coulomb forces between ESP point charges and a Lennard-Jones potential, whose coefficients for the surface atoms have been determined by fitting the classical PES of a water molecule at various separations from the TiO_2 rutile 110 surface to the corresponding DFT energies. In this way, the potential is fully consistent with commonly used biomolecular force-fields. We have demonstrated that the interactions with generic organic molecules can be reliably obtained by applying standard combination rules to the generalized AMBER force field (GAFF). In particular, the obtained potential is fully transferable to the case of molecules containing O, C, and H atoms adsorbed on thin oxide layers grown on metallic Ti, for which the adsorption PES calculated with

full DFT and with our classical potential is excellent. However, if the direct surface-molecule interactions involve nitrogen atoms, quantitative agreement between the DFT and classical PES could be achieved only after introducing an additional 9-6 potential to model the Ti-N interactions. After adjusting the respective potential parameters, using an NH_3 molecule adsorbed on the partially wet rutile surface as a reference, excellent transferability to the case of the natively oxidized surface has been found.

As mentioned before, the major approximation intrinsic in our potential parametrization is the use of standard DFT calculations to determine the reference surface/molecule interactions, which do not properly take into account dispersion forces. In our specific case however, where highly polar surfaces are considered, the electrostatic contributions far exceed weak forces of the Van der Waals type, resulting in adsorption energies of the order of 0.8 eV per water molecule. Indeed, with our potential parametrization we obtain a fairly good agreement between the absolute values of the computed and measured heat of immersion of TiO_2 crystals, as well as of the maximum adhesion force of single tyrosine molecules to Ti surfaces.

In fact, a potential as simple as the one presented here (based on purely electrostatic and Lennard-Jones interaction) is expected to be accurate only under the assumption that no bond breaking or forming events take place, except the direct binding of O or N atoms of organic molecules to Ti atoms of the surface, for which the potential has been parametrized *ad hoc*. Under this assumption, the transferability of our potential to the case of generic organic molecules on the oxidized titanium surface is surprisingly good, and allows us for the first time to investigate the atomistic mechanisms of biomolecular adsorption at titanium/water interfaces. Finally, charged surface terminations have been introduced, to account for the experimental surface charge and isoelectric point of titanium.

Chapter 6

Surface Recognition of Peptides

The specific recognition of materials surfaces by small peptide sequences has become a widely investigated, interdisciplinary research topic with fields of application ranging from nanoelectronics to medicine and pharmacology [148, 152]. However, a rationalization of the binding driving forces in terms of clear structure-function relationships is missing, as the atomistic details of material surfaces in a wet environment are hard to elucidate both experimentally and theoretically [52]. Even for the case of well-established peptide-material couples such as the titanium-binding motif minTBP-1, consisting of the amino acid sequence RKLPDA, the mechanisms of interactions remain speculative and based purely on electrostatic arguments [146, 76, 75]. Biological recognition, however, is based on a complex interplay of interactions that provide optimal host-guest matching via steric exclusions, hydrophobic/hydrophilic patterns, directional hydrogen bonding, solvent structuring, as well as electrostatics. In fact, a recent molecular dynamics study has pointed out that not only direct surface-molecule interactions, but indirect, solvent-mediated effects govern the adsorption behavior of the RKLPDA peptide on the neutral TiO_2(110) rutile surface [154].

Useful insights in the dependence of the adhesion strength on the single residues composing the minTBP-1-peptide have been obtained by means of atomic force microscopy (AFM), quartz crystal microbalance (QCM) and, in a single study limited to crystalline rutile, molecular dynamics (MD) techniques [146, 76, 75]. The adhesion strength, as measured for instance with AFM force spectroscopy, has been found to be strongly decreased upon mutation for alanine, especially of the positively charged R and K residues and of the cyclic P residue, as well as on changing of the residue positions within the sequence

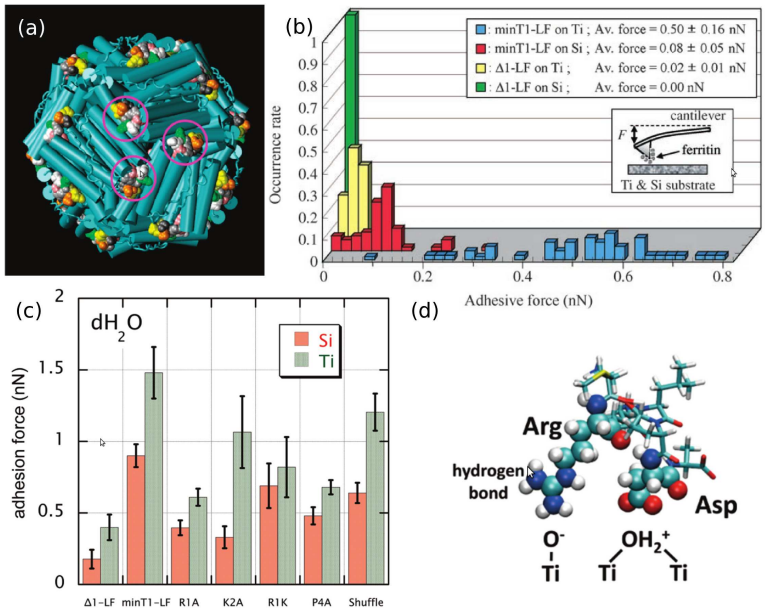

Figure 6.1: Experimental results for the adhesion of the minTBP-1-peptide RKLPDA. Ferritin complex modified with RKLPDA-peptides ((*a*), *circles*, taken from Ref. [76]). AFM adhesion force histograms of ferritin with and without minTBP-1 on Ti and Si, measured in the presence of TWEEN20 surfactant ((*b*), taken from Ref. [195]). Average AFM adhesion forces of ferritin modified with different mutations of the minTBP-1-peptide on Ti and Si ((*c*), taken from Ref. [75]). Adsorption model proposed by Hayashi et al. based on experimental results ((*d*), taken from Ref. [75]).

(cf. Fig. 6.1). Since the same peptide binds also, but less strongly to silicon, the latter surface has often been used as a comparison, as subtle differences in the binding under different conditions may help elucidate the origin of its specific binding mechanism to Ti [75]. This is the subject of our investigations, which go beyond idealized, crystalline surfaces and make use, instead, of realistic surface models of the natively oxidized Ti and Si surfaces in contact with liquid water.

6.0.1 Surface Models and Computational Details

To this end, we use the structural and interaction model for the natively oxidized titanium surface, as described in chapters 4 and 5. In detail, a negatively charged surface with a charge density of -0.123 C/m^2 has been employed, where the ratio of negatively charged

$TiOH^-$ groups to positive protonated bridging oxygen is set to 16:5 (cf. Sec. 5.5). For the RKLPDA simulations the titanium surface covers an area of 35.23×40.68 Å^2. For the truncated amino acid side chains studied in Sec. 6.2.6 a smaller model with an area of 26.42×30.51 Å^2 is employed.

The oxidized silicon surface is modeled based on the structure and the force field proposed by Cole et al. [39]. To compare the results to the charged oxidized titanium surface at the same level, we introduce charged surface terminations. In contrast to titanium, on the neutral surface only hydroxyl groups are present, which originate from spontaneously dissociated water molecules [39]. The isoelectric point of silicon surfaces is found to be lower than 3.0 [121, 84], allowing almost exclusively negative surface terminations, which, in this case, are deprotonated silanol groups (SiO^-). One out of four hydroxyl groups is deprotonated, yielding a surface charge of -0.136 C/m^2 similar to experimental values [164]. The DFT ESP charges of this surface reveal that the negative charge is, in contrast to the titanium surface, rather localized around the deprotonated hydroxyl group. Based on the DFT results the charges of the oxygen, the connected Si atom, the next shell of oxygen atoms and the second shell of Si are changed with respect to the original model to obtain a total charge of -1.0 e per negative group.
The surface area comprises 43.49×43.49 Å^2 for the entire peptide and 32.61×32.61 Å^2 for the truncated side chains.
The RKLPDA peptide is described by the AMBER force field [45]. Its termini are capped by ACE (i.e CH_3CO-) respectively NME (i.e. -$NHCH_3$) residues to avoid charged end groups that are not present in the experimentally studied molecules [76, 75].

All simulations are carried out using the program package LAMMPS [138]. To increase the computational efficiency, the surface atoms except for hydroxyl groups and hydrogens attached to bridging oxygen atoms are frozen. All bonds including hydrogen atoms are constrained to their equilibrium values. Electrostatic interactions are calculated by the pppm method with a precision of 10^{-5}. A 12.0 Å cutoff for the non-bonded interactions and for the real-space contribution of the electrostatics has been chosen. The production simulations are performed in an NVT ensemble using a Nosé-Hoover thermostat [81] with a timestep of 2.0 fs at a temperature of 300 K. As it is generally almost impossible to calculate the pressure tensor in simulations involving polar substrates with fixed atoms, the height of the simulation cell is initially adjusted to maintain the standard water density in a volume element far away from the surface.

6.1 Free Energy of Adsorption

Before discussing the adhesion mechanisms in detail, we first focus on quantifying the adsorption of the peptide in general. When considering equilibrium adsorption the free energy change ΔG_{ads} is the central observable. The dissociation constant $K_d = K_{ads}^{-1}$ for the titanium-binding peptide (TBP) RKLPDAPGMHTW, which contains the titanium-binding motif (minTBP-1) RKLPDA, has been determined experimentally using light extinction measurements in the supernatant phase [146]. In detail, a value of $K_d = 13.2 \pm 4.0$ μmol/l has been measured on titanium which yields, according to Eq. 2.2, a free energy value of $\Delta G_{ads} = -0.394$ eV. Compared to minTBP-1, the TBP features an excess sequence of amino acids which has been shown to have little effect on the adsorption at titanium substrates, though [147]. Hence, we assume the free energy of adsorption for the RKLPDA-hexapeptide to be close to this value.

In order to compare our simulation model to these experiments and to establish a reliable method to calculate ΔG_{ads} for such medium-sized molecules, we perform different free energy calculations for the RKLPDA peptide on the oxidized titanium surface.

As the experimental free energy difference is commonly associated with an equilibrium of adsorption and desorption, it is important to take both processes into account when ΔG_{ads} is calculated from MD simulations. In this regard, metadynamics (cf. Sec. 3.4.3) provides a conceptually superior approach compared to thermodynamic integration or umbrella sampling, in particular when investigating heterogeneous surfaces. As this technique introduces a bias potential to compensate the true free energy profile, the motion of the reaction coordinate ultimately becomes diffusive and an equilibrium between adsorption and desorption can be observed at room temperature even on the simulation timescale of some tens of nanoseconds. Moreover, in order to achieve sufficient sampling of the complete phase space of the peptide, we perform another set of metadynamics simulations in which we additionally apply the replica exchange method with solute tempering (REST) as described in section 3.4.4. In detail, the simulations are performed in the well-tempered ensemble with a bias factor of 10.0. Gaussian hills with a height of 0.02 eV and a width of 0.1 Å are deposited every 0.5 ps. In the REST simulations four replicas at solute temperatures of 300, 350, 400, and 450 K are employed and exchanges between

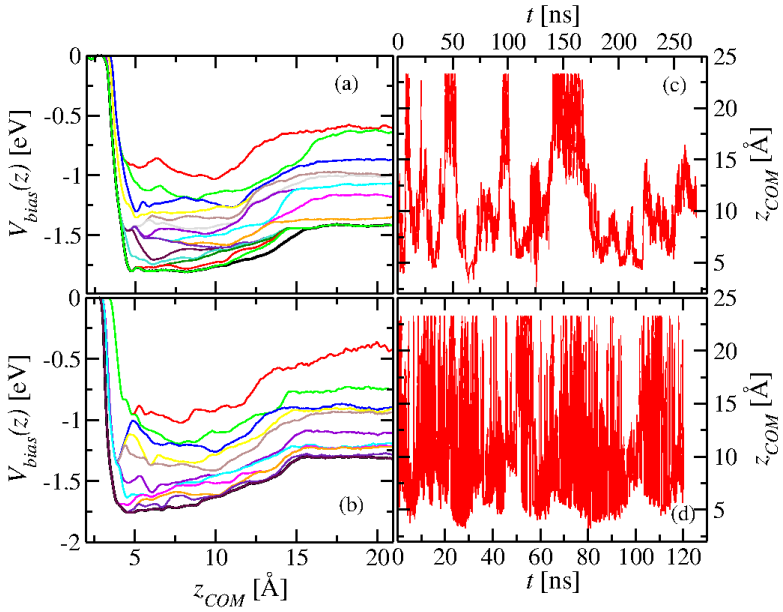

Figure 6.2: Evolution of the bias potential from the metadynamics (*a*) and the metadynamics+REST (*b*, base replica) simulation. Trajectories of the reaction coordinate z_{COM} from the metadynamics (*c*) and the metadynamics+REST (*d*, base replica).

replicas are attempted every picosecond. The results presented in the following comprise simulations over 270 ns for metadynamics alone and 120 ns for metadynamics+REST.

The time evolution of the bias potential for both metadynamics and metadynamics+REST (300 K replica) are displayed in Fig. 6.2, along with the corresponding trajectories of the reaction coordinate. While the reaction coordinate for metadynamics alone samples about 4 transitions between adsorbed state and solution, the metadynamics+REST simulation exhibits a discontinuous center of mass trajectory with enhanced sampling of the reaction coordinate range. As far as the exchange of the replicas is concerned, we find that all of them are able to access the entire temperature range, even on the time scale of few nanoseconds (as displayed in Fig. 3.4).

The final free energy profiles are displayed in Fig. 6.3. From the entire profile, we can compute a net free energy of adsorption ΔG_{ads} as [133]

$$\Delta G_{ads} = -k_B T \ln \frac{c_{ads}}{c_{bulk}} , \tag{6.1}$$

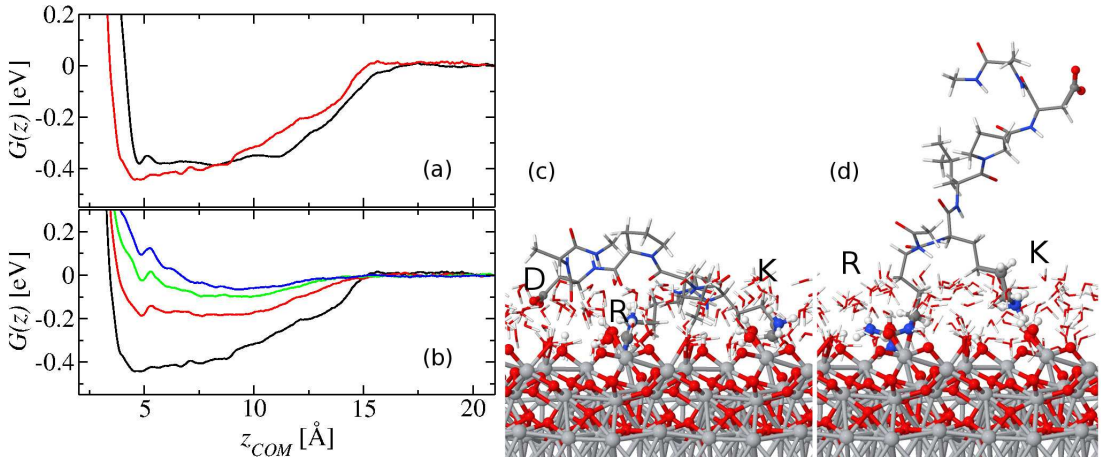

Figure 6.3: (*a*) Free energy profile of the titanium-binding motif RKLPDA on Ti obtained by metadynamics (*black*) and metadynamics+REST (*red*). (*b*) Free energy profiles of each REST solute temperature: 300 K (*black*), 350 K (*red*), 400 K (*green*), and 450 K (*blue*). Flat (*c*) and upright (*d*) adsorbed geometries from metadynamics+REST simulations.

where

$$c_{ads} = \frac{1}{z_0 - z_{min}} \int_{z_{min}}^{z_0} \exp(-\beta G(z)) dz \ , \ c_{bulk} = \frac{1}{z_{max} - z_0} \int_{z_0}^{z_{max}} \exp(-\beta G(z)) dz \ , \quad (6.2)$$

and z_0 defines the border between adsorbed region and bulk solution. The integrated value of the adsorption free energy for metadynamics alone is $\Delta G_{ads} = -0.34$ eV whereas for metadynamics+REST a value of $\Delta G_{ads} = -0.40$ eV is obtained. After the first 50 ns we find that for metadynamics+REST ΔG_{ads} varies only little with increasing simulation time. We estimate the error by the amplitude of the oscillations around the final value as 0.04 eV. For metadynamics alone it appears more difficult to achieve convergence even after more than 250 ns of simulation time. Though ΔG_{ads} does not change significantly during the final 50 ns, a further systematic change cannot be excluded, given the small number of transitions between adsorbed state and bulk solution. Consequently the error must be assumed to be considerably larger compared to the metadynamics+REST value. Importantly, both values are in overall consistency with the experimental free energy of adsorption of the TBP molecule. While ΔG_{ads} obtained from metadynamics alone underestimates the experimental value, the free energy difference obtained from metadynamics+REST indeed shows excellent agreement.

Although the free energy profiles obtained for the high temperature replicas (Fig. 6.3

(b)) do not have a physical meaning due to the artificial implementation of the solute tempering, they are important from a technical point of view. When considering e.g. the profile associated with the 400 K replicas, we already find an almost completely flat free energy landscape. This means that the molecule hardly encounters any significant barrier upon desorption. Thus, in addition to enhanced sampling of internal degrees of freedom of the peptide, the replica exchange method apparently improves sampling along the reaction coordinate, visible in the center-of-mass-trajectory in Fig. 6.2.

In the adsorbed configurations of the peptide taken from the metadynamics+REST simulations the arginine side chain is always in close contact with the surface. The importance of this residue for the adhesion to the surface has been reported experimentally in Refs. [147, 146, 75]. In general we observe two main adsorbed geometries:
The states with their center of mass close to the surface are associated with conformations where R, K, and D side chains are attached to the surface (Fig. 6.3 (c)). These contacts enforce a flat, tightly bound geometry, even allowing the formation of hydrogen bonds between backbone amine groups and the exposed surface oxygen atoms. While the exact adsorption mechanism of R and K will be discussed in detail in Sec. 6.2.5, we mention here that the carboxylate group of D can approach the surface either via hydrogen bonds with surface hydrogen atoms or via an adsorbed sodium ion.
In addition, we encounter geometries with the carboxylate group of D pointing towards solution (Fig. 6.3 (d)). In this case the molecule assumes a more vertical adsorption conformation where the contact is established merely by the positively charged end group of R, in most cases accompanied by K. Comparing the free energy profiles obtained with and without solute tempering, we find considerable differences particularly in the range of small reaction coordinate values. The solute tempering simulations reveal a pronounced minimum which does not emerge to this extent in metadynamics alone, as also reflected in the smaller ΔG_{ads} value. Such reaction coordinate values correspond to tightly adsorbed conformations (Fig. 6.3 (c)). The increased population of these states upon solute tempering suggests that they require intramolecular barriers to be overcome. This finding is corroborated by equilibrium simulations which reveal such adsorbed geometries only after a period of annealing at 450 K. In metadynamics alone such conformations are less likely to be encountered, stressing the importance of additional sampling methods.
In all cases the desorption of the peptide crucially involves the detachment of R.

6.2 Adhesion forces on Ti and Si

6.2.1 Initial configurations

To compare our simulations of the RKLPDA peptide on titanium and silicon to the AFM experiments of Ref. [76, 75] and in order to investigate the detachment processes on an individual basis rather than as an averaged quantity, we perform SMD simulations as described in Sec. 5.3.2 to compute adhesion forces. One of the major challenges when comparing to such experiments is to gather a representative statistical sampling. Therefore, special attention is paid to the generation of independent adsorption configurations which is carried out according to the following scheme. First, the peptide is annealed in solution for 0.7 ns with random initial velocities at 450 K in a langevin thermostat, followed by 0.8 ns of annealing at 300 K. The resulting system of solvent and peptide is shifted along the z-direction under periodic boundary conditions until the peptide resides at the bottom of the cell. The entire block is then placed in the vacuum gap between the two oxidized surfaces of the titanium or the silicon slab. After a short relaxation the cell height is slowly adjusted to maintain the correct water density in the bulk region during a 200 ps run. Finally, we anneal the whole system once more at 450 K for 0.7 ns to overcome possible barriers followed by another equilibration at 300 K for 1 ns. A total number of 29 different starting configurations for titanium and 26 configurations for silicon are considered.

On titanium we find that RKLPDA can adsorb with the side chains of the charged R, K and D residues, in line with the adsorption model proposed by Hayashi et al. [76, 75] (cf. Fig 6.1 (d)) and with simulation results on the neutral TiO_2 rutile surface [154]. Apart from one case, all initial conformations feature the guanidinium group of R adsorbed on the surface, accompanied by either the positively charged K end group or the negative carboxylate group of D. Some initial geometries even reveal the simultaneous adsorption of all three residues (cf. Fig. 6.5). This behavior corresponds to the findings of our extensive metadynamics+REST simulations, indicating that the protocol for the generation of initial conformations indeed samples the phase space well.

On the oxidized silicon surface we find a similar situation, clearly favoring the adsorption via the R residue, which remains close to the surface, in most cases accompanied by the K side chain. However, in contrast to titanium, D is rarely found in proximity of the silicon surface.

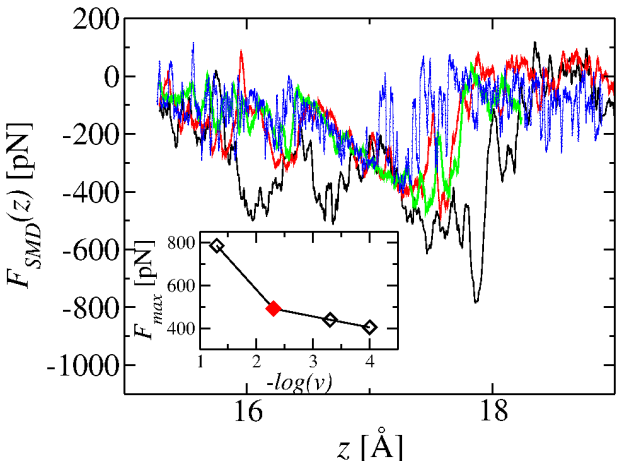

Figure 6.4: Force-displacement curves for the R endgroup on Ti obtained with pulling velocities of 5.0 (*black*), 0.5 (*red*), 0.05 (*green*), and 0.01 (*blue*) m/s. The peak force in dependence of the negative logarithm of the velocity is displayed in the *inset*.

6.2.2 AFM force histograms

To compute the adsorption forces on the two surfaces and compare our results to the AFM force spectroscopy experiments of Refs. [76, 75], we perform a series of steered molecular dynamics simulations (SMD) [88] as described in Chap. 5. For each adsorbed configuration, the molecule is pulled off the surface using a time-dependent harmonic potential

$$V_{smd}(z_c, t) = \frac{1}{2} k_{smd}(z_c - z_0(t))^2 \ , \tag{6.3}$$

where the z-coordinate z_C of the carbon atom of the NME cap at the C-terminal end of the peptide is tethered to an anchor $z_0(t) = z_C(t = 0) + v_{smd} \cdot t$ moving with constant velocity. Each simulation is carried out until the molecule completely desorbs from the surface (up to 7 ns in each case), with parameters $k_{smd} = 0.5$ eV/Å^2 and $v_{smd} = 0.5$ m/s. Running averages over blocks comprising z-values of 0.05 Å are performed on the force-displacement curves, which appeared to remove high-frequency oscillations, while leaving the overall shape of the curve unaffected.

The pulling velocities feasible in SMD simulations are typically several orders of magnitude larger than the experimental ones. Before discussing the results obtained for the entire peptide, we assess the influence of the pulling velocity on the adhesion forces, considering the case of the $CNHCH_3(NH_2)_2^+$ molecule as a model for the arginine end group

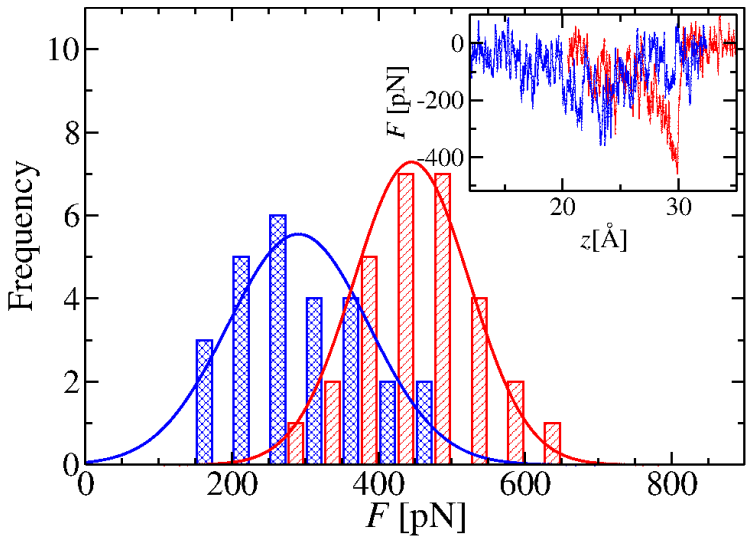

Figure 6.5: Histogram of the SMD force peaks and typical force-displacement curves (displayed in the inset) on titanium (*red*) and on silicon (*blue*).

(cf. Sec. 6.2.6). From the same initial adsorbed geometry on titanium, we perform several SMD simulations, pulling the molecule with velocities of 5.0, 0.5, 0.05, and 0.01 m/s off the surface. The resulting force-displacement curves are displayed in Fig. 6.4. While the F-D-curve corresponding to the largest velocity apparently overshoots the adhesion force, the remaining curves yield similar characteristics and values in the same range. Beyond the sharp drop from 5.0 to 0.5 m/s, the peak values decrease only slightly upon further reduction of the speed. We therefore choose to use a velocity of 0.5 m/s for our production simulations. Given that the resolution of the adhesion force histogram is as large as 50 pN, this setting yields reasonable peak force values, while allowing to include a large number of different initial geometries, which is equally important for a realistic quantification. Notwithstanding, one has to bear in mind the velocity issue when comparing the simulation results to AFM experiments.

In Fig. 6.5 representative force-displacement curves for the RKLPDA peptide on the oxidized titanium and silicon surface are displayed. The force-displacement curves typically exhibit an initial increase of the force which in some cases features several smaller subpeaks, until a maximum force peak is reached, after which the force decays rapidly. The peak force of each SMD run has been evaluated and the results are displayed in a histogram in Fig. 6.5. The forces range from 250 pN to 650 pN for the Ti surface and

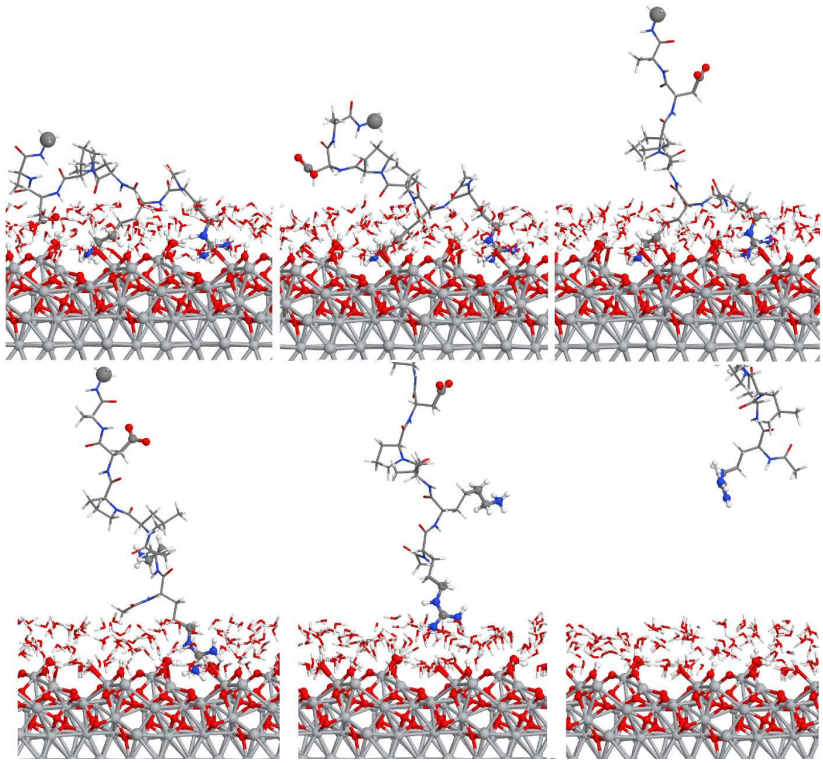

Figure 6.6: Snapshots from a typical SMD simulation of the minTBP-1-peptide on titanium. The charged end groups are displayed as ball-stick models, the large sphere marks the carbon atom to which the spring is attached.

from 150 pN to 500 pN for Si. Average detachment forces are obtained by fitting the histograms with a Gaussian function which yields values of 445 ± 79 pN on titanium and 291 ± 96 pN on silicon. These force values are about a factor 3 smaller than the AFM experiments of Refs. [76, 75]. This is most probably due to the fact that the experiments were performed with a RKLPDA-modified ferritin protein (cf. Fig. 6.1), meaning that the measured forces likely contain contributions from more than one peptide and from the ferritin itself. We note, however, that the experimental force distribution measured on Ti in the presence of TWEEN20 surfactant [76, 195], introduced to reduce hydrophobic protein-surface interactions and obtain values representative of a single RKLPDA peptide, agrees remarkably well with our simulation results (the measured average force on Ti is 0.5 ± 0.16 pN, cf. Fig. 6.1)). Moreover, most importantly, the ratio between the average forces on Ti and on Si obtained in our simulations is about 1.5:1, which is in excellent agreement with the experimental ratio of about 1.6 obtained experimentally in pure water

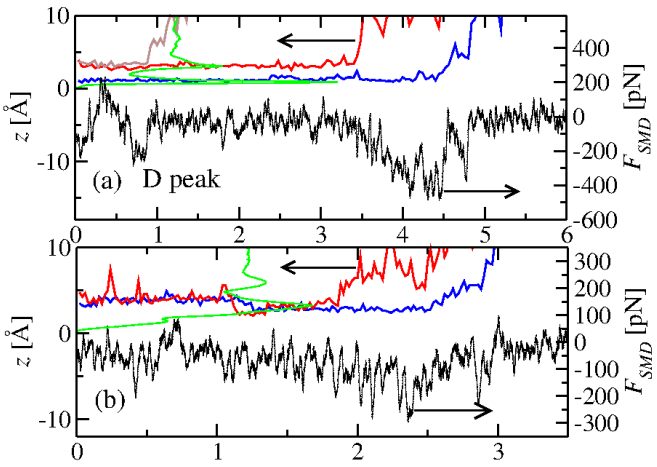

Figure 6.7: Trajectories of the central C atom of the R end group (*blue*) and of the N atom of K (*red*) along with the corresponding SMD forces (*black*) on titanium (*top*) and silicon (*bottom*) and the respective water density profile (*green*). Additionally, on Ti the carboxylate C of the D residue is displayed (*brown*).

[75].

6.2.3 Analysis of SMD

This agreement encourages us to carefully analyze the trajectories of the SMD simulations in order to elucidate the mechanisms underlying this specific adhesion. Irrespective of the initial conditions, on titanium the R side chain remains in proximity of the surface, in most cases accompanied by K, until the onset of detachment. In general, the maximum force peaks in all SMD simulations are associated with the detachment of either the R or the K side chain, whereas detachment of the D residue causes merely a smaller pre-peak of about 250 pN (see Fig. 6.7 and the corresponding snapshots in Fig. 6.6). In part, this is due to the fact that K and R are naturally the last residues to be pulled off the surface when the harmonic spring is attached to the alanine C-terminal of the peptide, consistently with the AFM experimental setup. Yet, the minor detachment force of D indicates that the adhesion of this residue is not as pronounced as it is for the positively charged ones.

A similar situation is observed on the oxidized Si surface: A typical example is shown in 6.7, where the desorption of the peptide takes place via detachment of the R side

chain. Equivalently, we have found several events with K involved in the main desorption process. Compared to titanium the force peaks often emerge less distinctly.

6.2.4 Water structures on the two surfaces

The similar desorption behavior on Ti and Si argues against a significant influence of the chemical nature of the adsorbed residues on the different adhesion forces. As proposed by Hayashi et al. [76, 75], the D residue indeed exhibits a distinguished behavior, as it can bind to titanium, but hardly to silicon. This difference apparently influences the equilibrium adsorption of the peptide, as discussed in the context of adsorption free energy in Sec. 6.1. The stronger adhesion forces on Ti, though, reveal no direct correlation with this particular role of aspartic acid, as they are produced exclusively by the detachment of R and K. Instead, the major differences between Ti and Si seem to arise from the specific interactions of the R and K side chains with the markedly different structures of the water solvent at the solid/liquid interfaces, and thus from the degree of surface hydrophilicity.

The density profiles of water oxygen atoms along the normal direction to the Ti and Si surfaces are displayed in Fig. 6.8, revealing the expected, pronounced ordering of the water molecules in both cases. On titanium, however, the density within the first layer is much larger, the layer width is smaller and even the second layer still emerges distinctly, being comparable to the first main peak on silicon. This evident structuring is intriguing giving that, compared to the commonly used, almost ideally flat model systems, both surface models exhibit considerable topological roughness and chemical heterogeneity. In fact, a laterally resolved analysis of the water structure reveals that on the oxidized Ti surface the density maxima appear as localized spots, whereas on Si they assume a rather contiguous form. In addition, particularly the Si surface presents outspread areas of reduced water density, which can be associated with local hydrophobic sites, similar to simulation results on various silica and quartz surfaces [35, 132]. Interestingly, the adsorption geometry of the peptide is directly influenced by the local density changes in the water structure, resulting in subtle differences in the adsorption configurations of the R and K side chains on Ti or Si, as shown in Fig. 6.8: On Si the aliphatic parts of the side chains spread almost flat within regions of low water density, while the charged moieties occupy large-density positions. On Ti the side chains adsorb in an upright manner, suggesting a stronger hydrophilic character of the surface. In particular, localized water density maxima, facilitated by the topological features of the oxidized surface, apparently

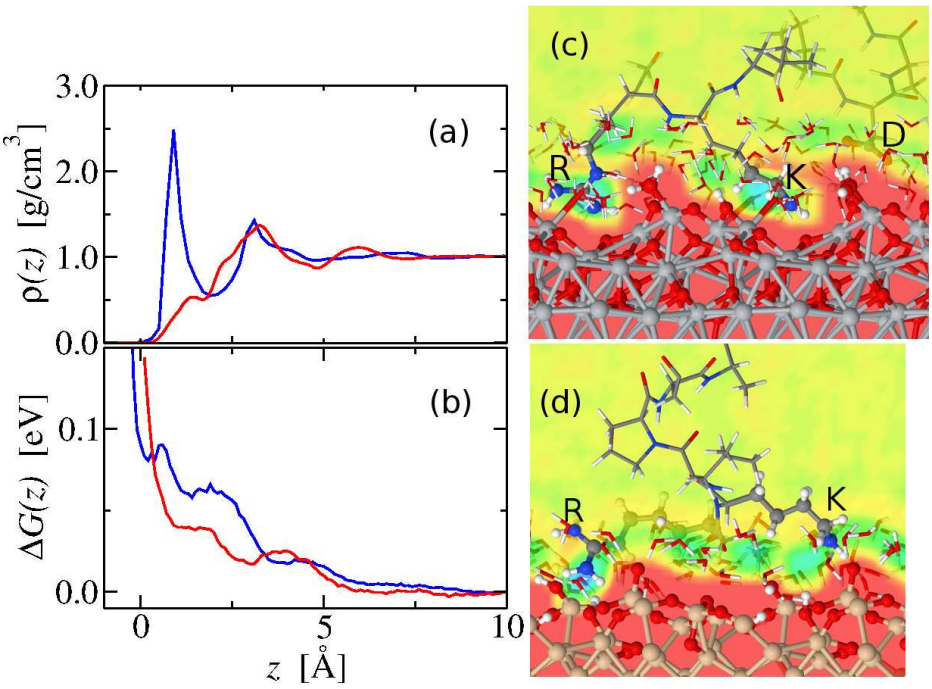

Figure 6.8: (*a*) Density profile of water oxygen on Ti (blue) and on Si (red). (*b*) The free energy profiles of a spherical hydrophobic solute on Ti (blue) and on Si (red). (*c,d*) Adsorbed peptide on Ti respectively Si with a map of the unperturbed water density (displayed within a vertical plane, which includes the R and K end groups).

act as adsorption "hot spots", capturing the polar arginine end group in a stable way during the SMD simulations until detachment.

Instead of measuring the contact angle, which is impeded by the surface charge and the counterions, a quantitative assessment of the hydrophilic character of the two surfaces is performed by calculating the local compressibility of a spherical hydrophobic solute of radius 2.5 Å. Its interactions with all other atoms are modeled by a WCA potential [187], following the method introduced in Ref. [62, 1] [1]. As displayed in the inset of Fig. 6.8, the computed adsorption free energy profile is positive in both cases, indicating hydrophilic surfaces. The stepwise increase of the free energy profile bears the signature of the water

[1]The PMF of the hydrophobic WCA solute is calculated by performing an equilibrium simulation without bias potential for 20 ns. The free energy is evaluated using the probability ratio method, $G(\lambda) = -k_B T \ln P(\lambda)$, which we have found to yield equivalent results compared to other approaches involving a bias potential.

layers, which successively have to be penetrated upon approaching the surface. The height of each step is larger on Ti compared to Si, suggesting a more stable water structure and hence a stronger hydrophilic character.

6.2.5 Different forces from different water structures

Considering in detail the z-trajectory (Fig. 6.7) of the guanidinium group of R and the ammonium group of K on the Ti surface, we find that the latter preferentially resides within the first or the second water layer, where it forms hydrogen bonds with surface hydroxyl groups, adsorbed water molecules and bridging oxygen atoms. The former always accommodates reproducibly in a tilted position within the first water layer above the valley between two rows of bridging oxygen atoms (cf. Figs. 6.6 and 6.8). In this position it can interact directly with the surface atoms underneath and, at the same time, form a network of hydrogen bonds with both the molecules of the surrounding water layer and the adsorbed water and hydroxyl groups. Moreover, it is confined laterally by the rows of bridging oxygen atoms, thus acting as an anchor for the whole molecule. Upon pulling the molecule off the surface, the guanidinium group retains its conformation and sustains the pulling force until it suddenly snaps out of the water layer into a new metastable position with one of its amine groups still in the first water layer and the other one in the second layer. The anchoring of R within the first layer of adsorbed water is a significant difference of the natively oxidized Ti to the TiO_2 rutile 110 surface, where the first layer of water is built by molecules tightly bound to the fivefold coordinated titanium atoms and can hardly be entered by other adsorbates [127].
On the Si surface both the R and the K side chains reside within the first water layer, seeking proximity of a deprotonated hydroxyl group to establish hydrogen bonds. Direct interaction with surface bridging oxygen atoms is rarely observed, and the adsorbed residues still form a large part of their hydrogen bonds with surrounding water molecules. Due to the lesser extent of structuring within the first solvent layer, when the peptide is pulled off the surface the force increases up to a less pronounced maximum peak and does not drop sharply afterwards, indicating a softer desorption transition compared to the Ti surface (see Fig. 6.7).

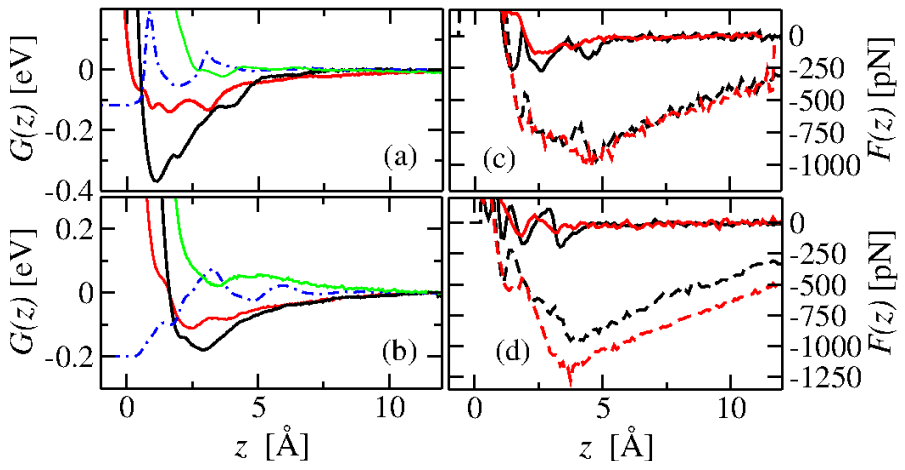

Figure 6.9: *Left*: Free energy profiles for truncated arginine (*black*), lysine (*red*), and aspartic acid (*green*) side chains on titanium (*a*) and silicon (*b*). The respective water density profiles (in arbitrary units) are depicted by the dashed blue lines. *Right*: Full (*solid lines*) and dry (*dashed lines*) equilibrium forces acting on the arginine (*c*) respectively the lysine (*d*) side chains on titanium (*black*) and silicon (*red*).

6.2.6 Adsorption of the end groups

In order to study in a more quantitative way the implications of the specific interfacial solvent structure on the driving force of peptide adsorption, we compute the free energy adsorption profiles for isolated R, K, and D side chains, modelled by a $CNHCH_3(NH_2)_2^+$, a $CH_3NH_3^+$, and a CH_3COO^- molecule, respectively. As in Sec. 6.1 we employ the metadynamics approach [2]. The evolution of the bias potential and the associated trajectory of the reaction coordinate is shown in Fig. 3.3.
The resulting free energy profiles are presented in Fig. 6.9.

On Si, the acetate molecule reveals a local minimum in proximity of the surface. This is separated by a free energy barrier from bulk solution, explaining the absence of D adsorption in our simulations of the peptide. On Ti, no significant barrier is found for this molecule, allowing spontaneous adsorption, however, the free energy minimum appears to be rather shallow. For the other molecules the adsorption takes place without a

[2]We choose the z-coordinates of the central C atom in R, the N atom in K, and C atom in D as reaction coordinate. We deposit Gaussian hills with 0.02 eV height and 0.1 Å width every 0.4 ps. Convergence is achieved by employing the well-tempered ensemble with a bias factor of 5.0

considerable free energy barrier. As the detachment forces arise merely from the positively charged residues, we will concentrate our investigations on these species in the following. Using Eq. 6.1, the strongest adsorption free energy is computed for arginine at the Ti surface, amounting to -0.305 eV compared to -0.151 eV on silicon. On both substrates lysine binds weaker, with ΔG_{ads} values of -0.092 eV on Ti and -0.066 eV on Si. From the convergence of ΔG_{ads} with simulation time (cf. Fig. 3.3) we estimate the error of all of these value as 0.01 eV.

We note that the adsorption behavior of the side chains observed in the simulations of the whole peptide is recovered from these profiles. On Ti, arginine has a stable adsorbed conformation in the first water layer with metastable states between both layers and inside the second layer, whereas lysine has the most stable location within the second layer, with local minima in the first layer accessible upon overcoming a small free energy barrier. On Si, the most favorable position of both residues is within the first, broad water layer. Remarkably, the methyl-ammonium molecule which we used as an analogue for the lysine residue, can approach the silicon surface both via the polar ammonium end and the nonpolar methyl group, in line with simulation results for methanol on quartz surfaces [132]. This indicates once more the presence of hydrophobic and hydrophilic regions in close vicinity to each other which has significant implications on the adsorption behavior. The overall shape of the free energy profiles reflects well the water density structure, with the density maxima coinciding with the free energy minima and with the more or less sharp structure of the water peaks corresponding with more or less pronounced slopes of the free energy wells. In particular, as the adhesion forces are determined by the free energy slope, higher forces are expected for the Ti surface, in agreement with the results of the SMD simulations presented above (see Fig. 6.5).

A careful analysis of the metadynamics simulations allows us now to asses the influence of the water structure on the surface adhesion. For each molecule and surface, we can compute force profiles $F(z)$ along the adsorption trajectories taking into account either all interactions ("wet" forces) or only direct molecule-surface interactions ("dry" forces) [3] (Fig. 6.9). The most evident result from this analysis is that the dry forces are much larger and much longer-ranged than the wet forces, due to the absence of electrostatic

[3]The dry forces were obtained from the metadynamics snapshots by removing the water molecules and calculating the forces on the molecule. As the system is no longer charge-neutral, the ewald sum is replaced by a coulomb sum which is cut off at a distance of 20 Å.

screening by the orientational and structural ordering of the water molecules above the surface and by the counterions. Remarkable is the inversion of the interaction strength, i.e. the dry adsorption forces are larger on the *silicon* surface. Instead, the wet forces on *titanium* clearly exceed the corresponding values on silicon consistently with the results of our SMD simulations of the whole RKLPDA peptide. Importantly, the peaks of the force profile not only can be assigned to the transitions between metastable states in the free energy profile, but also correspond to the peaks of the water density profile. In particular, we find multiple distinct force peaks for adsorption at the Ti/water interface, and only a single broad force peak for adsorption at the Si/water interface. In contrast, the dry forces lack a clear structure, again suggesting that adhesion forces are largely mediated by the water structure at the interface, which is thus at the origin of the stronger interactions with the Ti surface.

6.3 Summary and Discussion

In summary, our results provide a clear rationalization of the origin of the specific titanium recognition by the RKLPDA peptide. Consistently with the results of alanine substitution experiments [75] the R residue is mainly responsible for the stable anchoring of the peptide to the surface. In addition, we have found attachment of the positively charged K and the negatively charged D residues to facilitate equilibrium adsorption on Ti. In this context the presence of D on the surface generally causes a flat, tightly bound conformation, while the molecule assumes rather a vertical geometry when only the positive residues are attached. In both equilibrium and non-equilibrium SMD simulations the main barrier towards bulk solution is constituted by the detachment of R.

Employing metadynamics combined with additional sampling by the replica exchange with solute tempering (REST) technique, we have obtained an adsorption free energy of $\Delta G_{ads} = 0.4 \pm 0.04$ eV which agrees well with the experimental result determined for the similar titanium-binding-peptide (TBP) on titanium. The extension of metadynamics by the REST method indeed seemed to enhance phase space sampling considerably, as it facilitated the occurrence of the tightly bound conformations and accelerated the convergence of ΔG_{ads} considerably. The approximation of REST compared to conventional replica exchange is based on the concept that the tempering comprises only the solute's degrees of freedom and in part the interactions with its surrounding molecules, neglecting

most of the solvent's degrees of freedom. The implications of this approximation, particularly with respect to possible systematic errors could unfortunately not be investigated in detail, due to the lack of reference simulations with conventional RE. However, the excellent agreement with the experimental adsorption free energy is encouraging. Furthermore, given the fact that the REST method allowed simulation times larger than 100 ns for a solute temperature range between 300 and 450 K with reasonable exchange among all replicas, a situation which is outside the current possibilities of conventional RE simulations, the advantages of this method seem compelling. In fact, our free energy simulations show that such long times are crucial for the convergence of reliable adsorption free energies for medium-sized molecules.

In quantitative agreement with AFM force spectroscopy measurements, we have computed in extensive SMD simulations an average detachment force on Ti 1.5 times higher than on Si. On *both* substrates our simulations have revealed that only R and K contribute significantly to the maximum adhesion forces. This finding contradicts the experimental hypothesis that the electrostatically-driven selectivity of the surface towards specific residues is the reason for the different adhesion forces. Instead, by means of accurate calculations of adsorption free energy profiles, we have found a striking correlation between the adhesion forces and the nanoscale features of the water structuring at the solid/liquid interfaces. In fact, the interfacial water structuring has been found in previous studies to govern, for instance, the adhesion between silicon wafers [39] or the adsorption mode of a collagen fragment on hydrophobic surfaces [40]. A novel, yet crucial finding of this study is that the local solvent density variations near a heterogeneous, rough surface are sensed by the side chains of a peptide in a way that bear many features characteristic of the specific recognition in biomolecular aggregates. Our simulation highlight the importance not only of direct surface-molecule interactions at the anchoring points, but also of an alternation between hydrophilic and hydrophobic residues to optimize the matching with the solvent density oscillations. In this picture, electrostatic interactions still play an important role in driving the approach of charged residues towards surfaces with opposite charge density, but are, at least in this case, of secondary importance as far as adhesion forces are concerned.

Chapter 7

Contact Forces between Nanoparticles

In order to show that the range of possible applications of the force field model is not limited to biomaterials, I present in this chapter an example which is more related to the field of nano engineering. Agglomerates of nanoparticles are promising materials that can be used as catalysts, sensor films, or in hybrid materials. Titania particles in particular can be used as superhydrohilic surfaces, in photocatalysis, for water splitting, solar cells, and antibacterial agents [172, 196, 86]. Using flame spray pyrolysis, the chemical composition and also the general properties of the primary particles can be tailored in a controlled way by introducing dopant atoms, such as iron in the case of titanium oxide particles [171].

The contact forces between the aggregates of nanoparticles are a crucial aspect in this field, as they govern the mechanical properties of the aggregates. Cohesion forces within films of agglomerates can be investigated in AFM experiments, when the tip is repeatedly immersed into the nanoparticle agglomerate and retracted, gathering at the tip an increasing amount of aggregates, as shown in Fig. 7.1. These experiments however yield merely a superposition of force peaks, from which individual contributions and mechanisms can hardly be isolated. The average peak force that has been measured for aggregates of 10 nm sized primary particles is 3 nN [145].

One of the central quantities of interest is the interaction force between single primary particles. Contact forces and free energies can generally be obtained in molecular dynamics simulations, as reported for generic Lennard-Jones clusters [140]. Moreover, some MD studies have been published for TiO_2 nanoparticles, investigating the aggregation [5] and the sintering [96] of crystalline and amorphous nanoparticles. The underlying parti-

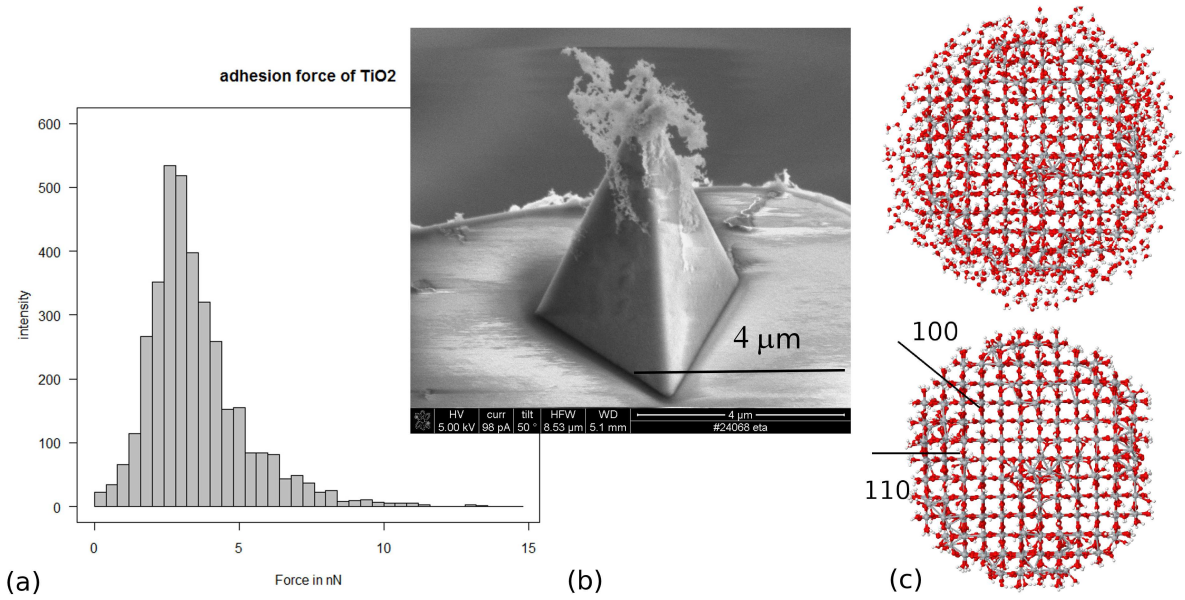

Figure 7.1: (*a*) Histogram of AFM force peaks obtained by repeated contact between tip and TiO_2 nanoparticle film [145]. (*b*) SEM picture of the tip covered with nanoparticle agglomerates after several contacts with the film [145]. (*c*) The two nanoparticle models with water coverages of 2 monolayers (*top*) and 1 ML (*bottom*). The investigated (110) and the (100) facets are marked with lines.

cle models feature dry surfaces without any physisorbed or chemisorbed water molecules which might be representative for very high temperatures. At room temperature and under atmospheric conditions however, one must always assume a certain amount of water molecules decorating the surface [128] which have significant effects on the interactions among the nanoparticles. In order to understand the distribution of the AFM force peaks, I perform simulations of the forces between two TiO_2 particles at different separations. In line with the general agenda of this dissertation, I use a realistic model of a rutile nanoparticle with different water coverages, corresponding to ambient conditions at different humidities.

7.1 Contact Forces between TiO_2 Nanoparticles

Microscopic analysis has revealed that the nanoparticles generated by flame spray pyrolysis possess a spherical shape. As even small amounts of iron have been found to favor rutile crystal structures [171], the nanoparticle model is generated by carving a sphere out of a rutile block, while preserving a TiO_2 stoichiometry. To keep the computational cost at a reasonable level, we have chosen to start with a diameter of $d = 4$ nm which is smaller than the primary particles of the common aggregates ($d \simeq 10$ nm), yet still in the range that can technically be produced. After generation, the dry particle is annealed at 800 K for 500 ps to facilitate structural reconstructions at the cutting edges, in particular healing the one-fold coordinated oxygen atoms. For the reasons discussed in Chap. 4 we use the force field of Matsui and Akaogi [119] with its original charge values at this stage. After a structural minimization, the charges are recalculated according to the EEM method. Subsequently the crystal is relaxed once more, now applying the EEM charges which represent the different oxidation states at the surface in a more accurate way.

From this point we keep the atomic structure of the nanoparticle fixed. The resulting particle is immersed into bulk water, using the force field described in Chap. 5 including the rescaled charges. After equilibration, the particle is found to be decorated with a layer of water molecules which adsorb at the undercoordinated surface Ti atoms. As the surface features a considerable number of defects which are known to facilitate water dissociation, we devise an *ad hoc* scheme to introduce such effects. In doing so, we focus on critically undercoordinated Ti atoms, i.e. atoms with less than five oxygen neighbors which we have found in our FPMD simulations to be particularly reactive (cf. Sec. 5.1). Water molecules adsorbed at these sites are identified and one proton is transferred to the nearest surface bridging oxygen atom. This way the overall charge of the particle remains neutral, avoiding additional technical challenges due to a charged surface at this stage which will be subject to future work.

Having relaxed and equilibrated the water and hydroxyl groups, two models with different water coverages are created. On the one hand, only the molecules that are directly bound to titanium are retained at the surface. On the other hand, all molecules beyond the first and the second water layer are removed and a coverage of 2 ML is obtained which corresponds to conditions of increased humidity. The final models are shown in Fig. 7.1. To simulate particle contacts, two identical replicas of each nanoparticle model are con-

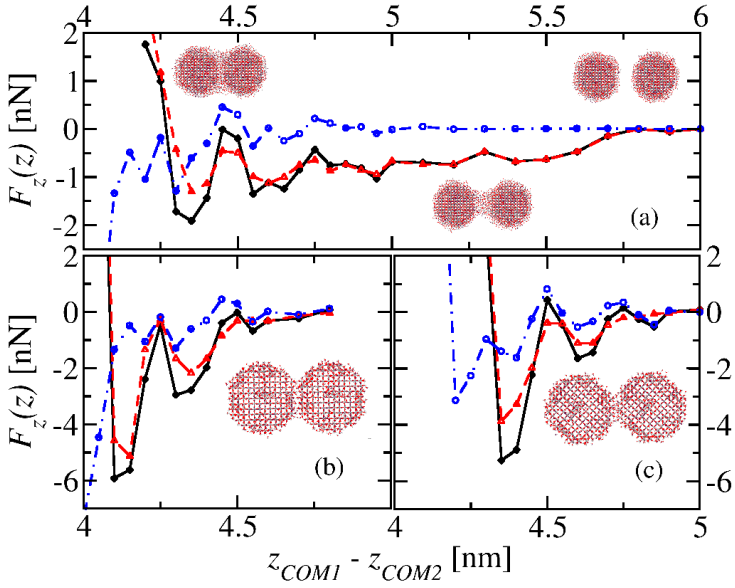

Figure 7.2: Force-distance curves between TiO_2 nanoparticles for different water coverages. High humidity (a) and dry conditions (b, c), where (b) displays particles approaching each other via their (110) surfaces and (c) refers to the (100) surfaces oriented towards each other.

sidered. In spite of its spherical construction the particle exhibits several facets which can be associated with the different crystal surfaces. To begin with, we have chosen to let the (110) surfaces face each other. Additionally, in order to assess the influence of the surface type we have considered the contact between the (100) surfaces for the particle with only one monolayer of water. Starting from a remote configuration, the particles are slowly approached by imposing a constant velocity to the otherwise fixed crystals, whereas the water and hydroxyl groups are allowed to move freely. At certain separations snapshots are taken to use them as initial configurations for the force calculations. These are carried out at fixed center of mass distances, while the total force acting on each crystal is averaged. Each simulation lasts for 2.5 ns, the first 500 ps are discarded. As expected according to Newton's third law, the forces on the two particles exhibit nearly same modulus but different signs, so that the average mutual force is calculated as $F_{av} = 1/2(F_1 - F_2)$.

The resulting force-distance curves for all three cases are shown in Fig. 7.2. Apparently, the particles with low water coverage reveal a considerably higher maximum force of

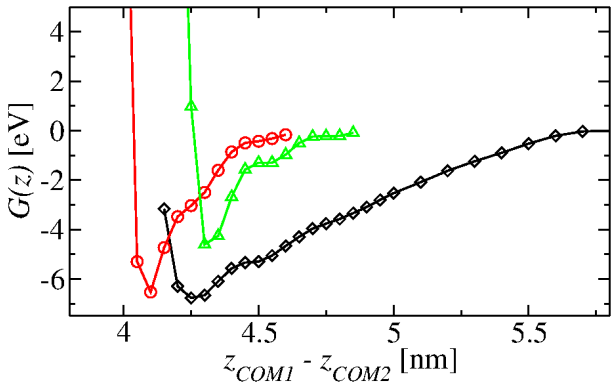

Figure 7.3: PMF obtained from the FD curves: 2 ML (*black*), 1 ML (110) (*red*), and 1 ML (10) (*green*).

about 6 nN, respectively 5 nN for the (100) facets, whereas for the particle with high coverage the forces only reach values of about 2 nN. On the contrary, while at low coverages the forces decay rapidly with increasing particle separation, the particles with 2 ML of water interact even at larger distances. This is reflected when considering the potentials of mean force (PMF), obtained by integrating the force-distance curves according to Eqs. 3.33 and 3.34, as shown in Fig.7.3. Remarkably, free energy minima for 2 ML and 1 ML possess nearly the same values of about 6 eV. Again, for the (100) surface a slightly lower value for the free energy minimum is found. The lower forces and free energies associated with this surface are most probably due to the smaller surface area that is involved in the contact.

To analyze the origin of the forces, each value is decomposed into the contributions arising from interactions between only the oxide crystal cores and from the interactions mediated by the water molecules. At small separations the total force-distance curves reveal pronounced oscillations, i.e. force maxima and minima which can be assigned clearly to the water mediated interactions. The oscillatory behavior arises from the interaction and interference of the water layers above the (110) respectively (100) facets. For the nanoparticles bearing 2 ML of water, we observe another type of interactions at intermediate separations. Beyond the oscillatory behavior a plateau with nearly constant force values is reached, stretching over 0.5 nanometers. The attractive interactions in this region are predominantly caused by capillary forces, accompanied by the formation

of a water neck between the nanoparticle surfaces (cf. Fig. 7.2). This behavior requires mobile water molecules which participate in the neck formation, hence, it hardly takes place at low coverages. The forces between the oxide crystal cores reveal large attractive contributions at very small separations, however, due to the steric repulsion of the water terminations, these regions are not accessible. In the accessible range oxide-oxide-iteractions play a minor role. Moreover, they decay quickly as the particles do not bear any net charge which involves only short-ranged, higher-order multipole moments.

In total, for both water coverages the resulting maximum force peaks agree quite well with the order of magnitude of the average experimental values, although the simulated particles are considerably smaller. This agreement might indicate that the AFM force peaks actually reflect the breaking of single nanoparticle contacts. For comparison, we have calculated the contact forces between two naked nanoparticles, i.e. without any adsorbed water molecules. In these simulations all atoms are allowed to move. The maxium force which occurs when the atoms of both surfaces directly interact with each other, reaches a value of about 50 nN. This is one order of magnitude larger than the forces obtained for the water covered particles and, importantly, than the force values measured in AFM experiments. Hence, the water termination of the nanoparticles must be assigned a crucial role in conveying the interparticle forces.

Similar observations have been reported in Ref. [39] for the cohesion forces between two oxidized silicon surfaces in the context of hydrophilic wafer bonding. These simulations reveal a pronounced dependence on the water coverage, in agreement with our results the maximum force has been obtained for a low water coverage.

Chapter 8

Conclusions and Perspectives

8.1 Summary of the Results

In this thesis I have developed a structural and interaction model for the interface between the natively oxidized titanium (0001) surface and a physiological environment which allows to study atomistic adsorption processes of biological molecules in a realistic way. Beyond the commonly used perfect crystal surfaces, the present approach includes topological and chemical heterogeneities, such as ridges formed by arrays of bridging oxygen atoms, different oxidation states of the titanium atoms and both charged and neutral surface terminations. The resulting model has been applied to investigate the specific adhesion of the titanium-binding motif (minTBP-1) RKLPDA onto the titanium surface. Moreover, I have studied the cohesion between TiO_2 nanoparticles with varying water coverage.

To obtain a structural model for the oxidized Ti surface, first-principles molecular dynamics simulations of the oxidation reactions of the metal surface were performed with subsequently introduced oxygen molecules, up to an oxygen coverage of 2 ML. In agreement with experimental data the oxidation reaction proceeded spontaneously up to a certain coverage where a saturation of of O_2 dissociation was found which, after all, could be overcome by annealing the substrate. The final structure featured an amorphous oxide network, with a stoichiometric composition corresponding to TiO, distinctly separated from the metallic phase, where the original hcp order of the Ti atoms was retained. Importantly, the spectrum of Ti oxidation states, as revealed by the Bader charges, could

be retrieved in a consistent way by charges obtained with the classical electronegativity-equalization method (EEM). This agreement provided the basic link to the development of a classical force field. The classical parametrization enabled to simulate the oxidized surface in room temperature MD simulations, preserving its structural details. Furthermore, a protocol to produce an artificial, large scale model of an oxidized titanium surface, whose properties are very similar compared to the DFT reference model, could be devised.

To model the interactions with adsorbates, in particular water, the potential was based on a picture where these molecules adsorb without dissociation, in agreement with FMPD simulations. Including only electrostatic and Lennard-Jones contributions, and rescaling the surface charges in an appropriate way, the interaction potential was designed to be fully compatible with the AMBER force field for the simulation of biological molecules. Indeed, although the adjustment was carried out for water adsorption on the crystalline TiO_2 rutile surface, the potential appeared to be transferable not only to the oxidized surface but also among various organic adsorbate molecules. The only exception in the transferability was revealed for the nitrogen-titanum interactions which to had be adjusted separately. The final force field was able to reproduce both DFT adsorption energies and experimental observables, such as the heat of immersion and the AFM detachment force of tyrosine molecules.

Having established its reliability, I investigated the potential of mean force of the RGD peptide upon adsorption on the oxidized titanium surface. The simulations gave rise to a free energy change upon adsorption that was considerably larger than the binding free energy of RDG to integrin receptors.

In the next step, I introduced charged surface terminations to account for the experimental surface charge density and IEP values. The charged surface was employed to simulate the adhesion behavior of the titanium-binding-motif RKLPDA. Remarkably, the simulations were able to reproduce both macroscopic (ΔG_{ads}) and microscopic (AFM forces) experimental observables in excellent quantitative agreement. Moreover, I have established the combination of metadynamics and replica exchange with solute tempering as a reliable, yet computationally feasible technique to obtain adsorption free energies for medium-sized molecules.

A careful analysis of the SMD trajectories allowed me to associate the adhesion forces with the underlying microscopic mechanisms on titanium and on silicon substrates. While on

titanium the aspartic acid residue could be assigned a significant role in the equilibrium adsorption structure, the adhesion forces were predominantly mediated by the positively charged arginine and lysine side chains on both surfaces. Considering the isolated free energy profiles of both relevant amino acid side chains, I have found clear indication that primarily the difference in the water structure above the surface produces the strong adhesion to titanium. In this context spatially restricted, local water density maxima, facilitated by the topological features of the oxidized surface, appeared to act as adsorption "hot spots", capturing the polar end groups, whereas regions of reduced water density accommodated hydrophobic parts of the peptide.

Finally, the force field was applied to calculate the cohesion forces between two TiO_2 rutile nanoparticles at different water coverage. The resulting peak forces were found to be in good consistency with experimental AFM force peaks obtained in films of nanoparticle agglomerates. For the lower water coverage the cohesion forces appeared to be considerably larger, with only little dependence on the orientation of the involved crystal facets, whereas the potential of mean force revealed very similar minimum values in all cases. Although the results are still subject to ongoing work, they suggest that the force peaks measured experimentally might indeed correspond to single particle contacts, mediated by the adsorbed water layer.

8.2 Perspectives

Since the force field for the interactions of the oxidized titanium surface in a wet or physiological environment gave reliable and promising results, it can be applied to investigate different kinds of systems.

The field of specific-binding-peptides still provides a variety of open questions regarding the origin of surface recognition which crucially requires accurate force fields and advanced sampling methods to compare to the experimental findings and ultimately to design novel molecules and surfaces. In particular the notion that the molecule primarily recognizes patterns in the water structure above the surface, might be extended into a generalized explanation for specific adsorption behavior. In the end, it may provide a basis for a rational design of material-binding peptide sequences, complementing "brute

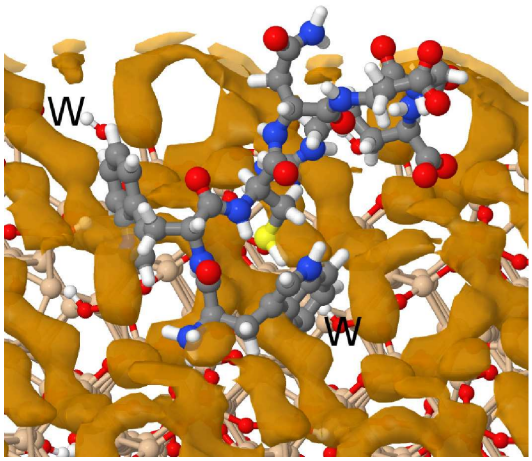

Figure 8.1: Simulation snapshot of the WWCNDGR peptide adsorbed on the oxidized silicon surface. The violet isosurface corresponding visualizes high water density regions ($\rho \geq 1.4$ g/cm^3). The binding tryptophan (W) residues are marked.

force" bioinformatics and combinatorial biochemistry approaches with atomic-scale details hardly accessible by experimental techniques. The models and methods applied and developed in this thesis set a good starting point for this challenge.
As an outlook, Fig. 8.1 displays the adsorbed geometry of the WWCNDGR peptide on the oxidized silicon surface which has been found in experiments to bind well to silica substrates [158]. Our preliminary simulations indicate that adsorption takes place primarily via tryptophan (W) and arginine (R). The interplay of the hydrophobic W and hydrophilic R residues with the regions of low, respectively high water density, as displayed by the isosurface, becomes clearly visible.

Apart from the adsorption of peptides, another field of application might be the investigation of enzyme-functionalized surfaces. Functionalization with entire, yet small proteins, such as lysozyme, is a promising approach to achieve e.g. anti-bacterial effects [143, 177]. Preliminary simulations have been carried out to study the adsorption of lysozyme on titanium as shown in Fig. 8.2. Interestingly, the molecule anchors via the same arginine residue, as found e.g. on silica [100], in a way which is similar to the minTBP-1 peptide. Though it is still unfeasible to obtain reliable adsorption free energy values for such a large molecule, yet, it might be possible to asses whether it retains its functionality even after adsorption. This important aspect could in principle be investigated by calculating the free energy of binding of polysaccharidic molecules to the reactive

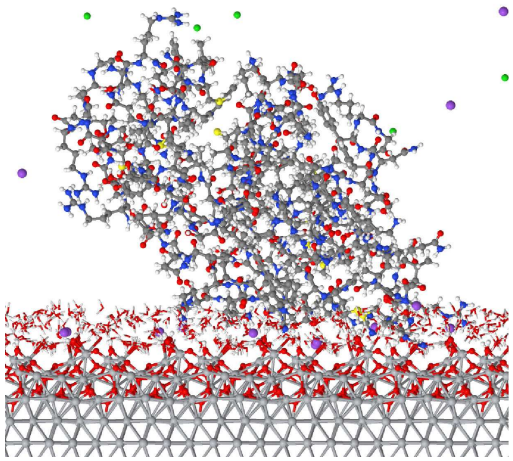

Figure 8.2: Lysozyme protein adsorbed on the oxidized titanium surface after 20 ns of equilibration.

site, before and after adsorption.

Beyond the particular case of the titanium surface the general scheme of potential development has appeared to be very robust and it has been successfully transferred to different substrates, e.g. to study the adsorption of glutathione disulfide (GSSG) on alumina surfaces [54]. For the future it appears promising to utilize this approach in order to create interaction potentials for other realistic oxidized surfaces, such as Al [44], TiN [198] and CoCr [197] for which atomistic models have recently been obtained in this group, thus taking the next step towards a more accurate description of biomaterials surfaces and interfaces.

When employing classical force field models, such as the one developed in this thesis, one has to be aware that chemical reactions are outside the scope of applicability, unless the model has been explicitly parametrized to account for such effects. In the present work this has been included with respect to the adsorption of oxygen or nitrogen containing molecules at undercoordinated Ti atoms. Apart from these situations, further expected reactions, e.g. de-/protonation events, can only be taken into account in a rigid, *ad hoc* way, by manually performing the reactions. However, this method is somewhat artificial and not very flexible. A better way to include chemical details is to use hybrid QM/MM schemes, combining empirical force fields and quantum mechanics in the same simulation [21]. The *Learn-on-the-fly* (LOTF) method [47, 21] has emerged as particularly promis-

ing for interface simulations, as it augments the classical Hamiltonian by an auxiliary set of springs to reproduce the quantum mechanical forces in the QM zone. This requires flexible force fields which can easily be adapted, for instance to changes in the structure of the surface. The interaction model developed in this thesis in principle fulfills this specification, as it does not impose any fixed topology within the oxide network and it automatically switches between metal substrate and oxide layer. Changes in the coordination can easily be taken into account by recalculating the EEM charges which we have found to be in very good consistency with DFT. Although various issues yet have to be solved regarding the application of the LOTF technique to solid/liquid interfaces in general, the simulation of the oxidized titanium surface within a QM/MM approach provides a challenging, but nevertheless promising task for the near future.

Acknowledgements

Above all, I am greatly indebted to my supervisor, Lucio Colombi, for his all advice, scientific and non-scientific. His enthusiasm about new ideas has always been an inspiration and motivation to me. At the same time Lucio has managed to create a really enjoyable working atmosphere within the group which continues even beyond work. I greatly appreciate the travel opportunities he has provided for everyone of us, in particular the Iran trip was more than memorable.
Of course, my present and former colleagues within the HMI group and the BCCMS have equally contributed to this atmosphere, in particular my officemate Mohammad, with whom I have shared many funny moments. Also Susi, Janina, Giulia, Meike, Sascha, Julian, Stefan, Kaibo and all other people at BCCMS have made my time in and out of the office a pleasant experience.
I am very thankful to Stefan and Mohammad for making all computers run smoothly and, most of all, fast. Apart from the local environment at BCCMS, I thankfully acknowledge allocation of computer time at HLRN (Hannover-Berlin) and the ZIH (Dresden).

I would like to thank my father for all his support during my entire time at university, as well as my sister Jana. My friends and roommates during all the time have been an invaluable help for me, cheering me up in times of frustration and keeping me from working when I really needed it. In particular I would like to thank Benjamin, Sebastian, Chris, Kai, Alex, and Lars.

But, most of all, I wish to thank Claudia.

Bibliography

[1] H. Acharya, S. Vembanur, S. N. Jamadagni, and S. Garde. Mapping hydrophobicity at the nanoscale: Applications to heterogeneous surfaces and proteins. *Faraday Discuss.*, 146:353–365, 2010.

[2] G. J. Ackland. Theoretical study of titanium surfaces and defects with a new many-body potential. *Phil. Mag. A*, 66(6):917–932, 1992.

[3] S. Aduru and J. W. Rabalais. Initial stage of titanium oxidation studied by direct recoil spectrometry. *Langmuir*, 3:543–547, 1987.

[4] T. Albaret, F. Finocchi, C. Noguera, and A. De Vita. First-principles study of the *tio*2(110) surface reduction upon na adsorption. *Phys. Rev. B*, 65(3):035402–035413, Dec 2001.

[5] M. Alimohammadi and K. A. Fichthorn. Molecular dynamics simulation of the aggregation of titanium dioxide nanocrystals: Preferential alignment. *Nano Lett.*, 9:4198–4203, 2009.

[6] M. P. Allen and D. J. Tildesley. *Computer Simulation of Liquids*. Clarendon Press, Oxford, 1987.

[7] H. C. Andersen. Molecular dynamics simulations at constant pressure and/or temperature. 72(4):2384–2393, 1980.

[8] T. Arlt, M. Bermejo, M. A. Blanco, L. G. J. Jiang, J. S. Olsen, and J. M. Recio. High-pressure polymorphs of anatase tio2. *Phys. Rev. B*, 61:14414–14419, 2000.

[9] M. Aziz-Kerrzo, K. G. Konroy, A. M. Fenelon, S. T. Farrell, and C. B. Breslin. Electrochemical studies on the stability and corrosion resistance of titanium-based implant materials. *Biomaterials*, 22:1531–1539, 2001.

[10] A. Azoulay, N. Shamir, E. Fromm, and M. H. Mintz. The initial interactions of oxygen with polycrystalline titanium surfaces. *Surf. Sci.*, 370:1–16, 1997.

[11] A. Azoulay, N. Shamir, V. Volterra, and M. H. Mintz. Water vapor interactions with polycrystalline titanium surfaces. *Surf. Sci.*, 422:141–153, 1999.

[12] R. F. W. Bader. *Atoms in Molecules: A Quantum Theory*, chapter 6, pages 169–247. Oxford University Press, Oxford, 1994.

[13] A. V. Bandura and J. D. Kubicki. Derivation of force field parameters for TiO_2-H_2O systems from ab initio calculations. *J. Phys. Chem. B*, 107:11072–11081, 2003.

[14] A. Barducci, G. Bussi, and M. Parrinello. Well-tempered metadynamics: A smoothly converging and tunable free-energy method. *Phys. Rev. Lett.*, 100:020603–020606, 2008.

[15] A. S. Barnard, P. Zapol, and L. A. Curtiss. Anatase and rutile surfaces with adsorbates representative of acidic and basic conditions. *Surf. Sci.*, 582:173–188, 2005.

[16] S. Bartkowski, M. Neumann, E. Z. Kurmaev, V. V. Fedorenko, S. N. Shamin, V. M. Cherkashenko, S. N. Nemnonov, A. Winiarski, and D. C. Rubie. Electronic structure of titanium monoxide. *Phys. Rev. B*, 56:10656–10667, 1997.

[17] C. I. . Bayly, P. .Cieplak, W. D. Cornell, and P. A. Kollman. A well-behaved electrostatic potential based method using charge restraints for deriving atomic charges: the resp model. *J. Phys. Chem.*, 97:10269–10280, 1993.

[18] A. D. Becke. A new mixing of hartreefock and local densityfunctional theories. *J. Chem. Phys.*, 98:1372–1377, 1993.

[19] H. J. C. Berendsen, J. P. M. Postma, W. van Gunsteren, A. DiNola, and J. R. Haak. Molecular dynamics with coupling to an external bath. *J. Chem. Phys.*, 81:3684–3690, 1984.

[20] R. Bernhardt, J. van den Dolder, S. Bierbaum, R. Beutner, D. Scharnweber, J. Jansen, F. Beckmann, and H. Worch. Osteoconductive modifications of ti-implants in a goat defect model: characterization of bone growth with sr μct and histology. *Biomater.*, 26:3009–3019, 2005.

[21] N. Bernstein, J. R. Kermode, and G. Csnyi. Hybrid atomistic simulation methods for materials systems. *Reports on Progress in Physics*, 72(2):026501–026525, 2009.

[22] J. B. Bignolas, M. Bujor, and J. Bardolle. A study of the early stages of the kinetics of titanium oxidation by auger electron spectroscopy and mirror electron microscopy. *Surf. Sci.*, 108:L453–L459, 1981.

[23] P. E. Blöchl. Projector augmented-wave method. *Phys. Rev. B*, 50(24):17953–17979, Dec 1994.

[24] E. M. Boczko and C. L. Brooks, III. Constant-temperature free energy surfaces for physical and chemical processes. *J. Chem. Phys.*, 97:4509–4513, 1993.

[25] M. Born and J. R. Oppenheimer. Zur quantentheorie der molekeln. *Ann. Phys.*, 84:457–484, 1927.

[26] R. Born, D. Scharnweber, S. Rößler, M. Stölzel, M. Thieme, C. Wolf, and H. Worch. Surface analysis of titanium based biomaterials. *Fresenius J. Anal. Chem.*, 361:697–700, 1998.

[27] S. Brunauer, P. H. Emmett, and E. Teller. Adsorption of gases on multimolecular layers. *J. Am. Chem. Soc.*, 60:309–319, 1938.

[28] M. C. Burrell. Stoichiometry and thickness of the initial oxide formed on clean titanium surfaces determined by quantitative auger electron spectroscopy, electron energy loss spectroscopy, and microgravimetry. *J. Vac. Sci. Techn. A*, 1:1831–1936, 1983.

[29] G. Bussi, D. Donadio, and M. Parrinello. Canonical sampling through velocity rescaling. *J. Chem. Phys.*, 126:014101–014107, 2007.

[30] G. Bussi, F. L. Gervasio, A. Laio, and M. Parrinello. Free-energy landscape for β hairpin folding from combined parallel tempering and metadynamics. *J. Am. Chem. Soc.*, 128:13435–13441, 2006.

[31] N. Cabrera and N. F. Mott. Theory of the oxidation of metals. *Rep. Prog. Phys.*, 12:163, 1949.

[32] L. Calzolai. Proteinnanoparticle interaction: Identification of the ubiquitingold nanoparticle interaction site. *Nano Lett.*, 10:3101–3105, 2010.

[33] C. Camilloni, D. Provasi, G. Tiana, and R. A. Broglia. Exploring the protein g helix free-energy surface by solute tempering metadynamics. *Proteins*, 71:1647–1654, 2008.

[34] R. Car and M. Parrinello. Unified approach for molecular dynamics and density-functional theory. *Phys. Rev. Lett.*, 55:2471–2474, 1985.

[35] R. Carr, J. Comer, M. D. Ginsberg, and A. Aksimentiev. Microscopic perspective on the adsorption isotherm of a heterogeneous surface. *J. Phys. Chem. Lett.*, 2(14):1804–1807, 2011.

[36] H. Cheng and A. Selloni. Surface and subsurface oxygen vacancies in anatase *tio*2 and differences with rutile. *Phys. Rev. B*, 79(9):092101–092104, Mar 2009.

[37] J. Cheng and M. Sprik. Acidity of the aqueous rutile tio2(110) surface from density functional theory based molecular dynamics. *J. Chem. Theory Comput.*, 6:880–889, 2010.

[38] Y. Choi, E. Kim, Y. Lee, M. H. Han, and I.-C. Kang. Site-specific inhibition of integrin avb3-vitronectin association by a ser-asp-val sequence through an arg-gly-asp-binding site of the integrin. *Proteomics*, 10:72–80, 2010.

[39] D. J. Cole, G. Csányi, M. C. Payne, S. M. Spearing, and L. Colombi Ciacchi. Development of a classical force field for the oxidised si surface: Application to hydrophilic wafer bonding. *J. Chem. Phys.*, 127:204704–204715, 2007.

[40] D. J. Cole, M. C. Payne, and L. C. Ciacchi. Water structuring and collagen adsorption at hydrophilic and hydrophobic silicon surfaces. *Phys. Chem. Chem. Phys.*, 11:11395–11399, 2009.

[41] L. Colombi Ciacchi. Modelling the onset of oxide formation on metal surfaces from first principles. *Int. J. Mater. Res.*, 98:708–716, 2007.

[42] L. Colombi Ciacchi, D. J. Cole, M. C. Payne, and P. Gumbsch. Stress-driven oxidation chemistry of wet silicon surfaces. *J. Phys. Chem. C*, 112:12077–12080, 2008.

[43] L. Colombi Ciacchi and M. C. Payne. Hot-atom o2 dissociation and oxide nucleation on al(111). *Phys. Rev. Lett.*, 92:176104–176107, 2004.

[44] L. Colombi Ciacchi and M. C. Payne. First-principles molecular-dynamics study of native oxide growth on si(001). *Phys. Rev. Lett.*, 96:196101–196104, 2005.

[45] W. D. Cornell, P. Cieplak, C. I. Bayly, I. R. Gould, K. M. Merz Jr., D. M. Ferguson, D. C. Spellmeyer, T. Fox, J. W. Caldwell, and P. A. Kollman. A second generation force field for the simulation of proteins, nucleic acids, and organic molecules. *J. Am. Chem. Soc.*, 117:5179–5197, 1995.

[46] S. R. Cox and D. E. Williams. Representation of the molecular electrostatic potential by a net atomic charge model. *J. Comp. Chem.*, 2:304–323, 1981.

[47] G. Csányi, T. Albaret, M. C. Payne, and A. D. Vita. "learn on the fly: A hybrid classical and quantum-mechanical molecular dynamics simulation. *Phys. Rev. Lett.*, 93:175503–175506, 2004.

[48] T. Darden, D. York, and L. Pedersen. Particle mesh ewald: An nlog(n) method for ewald sums in large systems. *J. Chem. Phys.*, 98:10089–10092, 1993.

[49] E. Darve. *Free Energy Calculations*, chapter 4, pages 119–170. Springer, Berlin, 2007.

[50] M. S. Daw and M. I. Baskes. Embedded-atom method: Derivation and application to impurities, surfaces, and other defects in metals. *Phys. Rev. B*, 29(12):6443–6453, Jun 1984.

[51] J. G. Dawber, L. B. Guest, and R. Lambourne. Heats of immersions of titanium dioxide pigments in aqueous solutions. *Thermochim. Acta*, 4:471–484, 1972.

[52] R. Di Felice and S. Corni. Simulation of Peptide-Surface Recognition. *J. Phys. Chem. Lett.*, 2(13):1510–1519, 2011.

[53] U. Diebold. The surface science of titanium dioxide. *Surf. Sci. Rep.*, 48:53–229, 2003.

[54] R. Dringen, Y. Koehler, L. Derr, G. Tomba, M. M. Schmidt, L. Treccani, L. C. Ciacchi, and K. Rezwan. Adsorption and reduction of glutathione disulfide on -al2o3 nanoparticles: experiments and modeling. *Langmuir*, 27:9449–9457, 2011.

[55] G. P. Drobny, J. R. Long, W. J. Shaw, M. Cotten, and P. S. Stayton. *Structure and Dynamics of Proteins Adsorbed to Biomaterial Interfaces*. John Wiley & Sons, Ltd, 2007.

[56] U. Essmann, L. Perera, M. L. Berkowitz, T. Darden, H. Lee, and L. G. Pedersen. A smooth particle mesh ewald method. *J. Chem. Phys.*, 103:8577–8593, 1995.

[57] Y. Fang, N. Poulsen, M. B. Dickerson, Y. Cai, S. E. Jones, R. R. Naik, N. Kroger, and K. H. Sandhage. Identification of peptides capable of inducing the formation of titania but not silica via a subtractive bacteriophage display approach. *J. Mater. Chem.*, 18:3871–3875, 2008.

[58] R. P. Feynman. Forces in molecules. *Phys. Rev.*, 56(4):340–343, Aug 1939.

[59] M. W. Finnis and J. E. Sinclair. A simple empirical n-body potential for transition metals. *Phil. Mag. A*, 50:45–55, 1984.

[60] H. Freundlich. Über die adsorption in lösungen. *Z. Phys. Chem.*, 57:385–470, 1907.

[61] J. D. Gale. Gulp - a computer program for the symmetry adapted simulation of solids. *J. Chem. Soc., Faraday Trans.*, 93(4):629–637, 1997.

[62] R. Godawat, S. N. Jamadagni, and S. Garde. Characterizing hydrophobicity of interfaces by using cavity formation, solute binding, and water correlations. *Proc. Natl. Acad. Sci. USA*, 106:15119–15124, 2009.

[63] H. Goldstein. *Classical Mechanics*. Addison-Wesley Pub. Co., 1980.

[64] G. K. Gomma and M. H. Wahdan. Effect of temperature on the acidic dissolution of copper in the presence of amino acids. *Mater. Chem. Phys.*, 39:142–148, 1994.

[65] X.-Q. Gong, A. Selloni, and A. Vittadini. Density functional theory study of formic acid adsorption on anatase tio2(001): Geometries, energetics, and effects of coverage, hydration, and reconstruction. *J. Phys. Chem. B*, 110:2804–2811, 2006.

[66] G. Goobes, P. S. Stayton, and G. P. Drobny. Solid state nmr studies of molecular recognition at protein-mineral interfaces. *Prog. Nuc. Magn. Reson.*, 50:71–85, 2007.

[67] A. Grossfield. Wham: The weighted histogram analysis method. `http://membrane.urmc.rochester.edu/content/wham`. (accessed, August 17, 2009).

[68] V. M. Gun'ko, J. P. Blitz, V. I. Zarko, V. V. Turov, E. M. Pakhlov, O. I. Oranska, E. V. Goncharuk, Y. I. Gornikov, V. S. Sergeev, T. V. Kulik, B. B. Palyanytsya, and R. K. Samala. Structural and adsorption characteristics and catalytic activity of titania and titania-containing nanomaterials. *J. Colloid Interface sci.*, 330:125–137, 2009.

[69] A. Hallil, R. Tétot, F. Berthier, I. Braems, and J. Creuze. Use of a variable-charge interatomic potential for atomistic simulations of bulk, oxygen vacancies, and surfaces of rutile tio2. *Phys. Rev. B*, 73:165406, 2006.

[70] W. R. Hamilton. On a general method in dynmaics. part i. *Phil. Trans. R. Soc.*, pages 247–308, 1834.

[71] W. R. Hamilton. On a general method in dynmaics. part ii. *Phil. Trans. R. Soc.*, pages 95–144, 1835.

[72] I. Han, B. Vagaska, B. J. Park, M. H. Lee, S. J. Lee, and J.-C. Park. Selective fibronectin adsorption against albumin and enhanced stem cell attachment on helium atmospheric pressure glow discharge treated titanium. *J. Appl. Phys.*, 109:124701–124710, 2011.

[73] X. J. Han, L. Bergqvist, H. Müller-Krumbhaar, J. K. Christie, S. Scandolo, and P. Tangney. Polarizable interatomic force field for tio2 parametrized using density functional theory. *Phys. Rev. B*, 81:134108–134116, 2010.

[74] T. Hanawa and M. Ota. Characterization of surface film formed on titanium in electrolyte using xps. *Appl. Surf. Sci.*, 55:269–276, 1992.

[75] T. Hayashi, K.-I. Sano, K. Shiba, K. Iwahori, I. Yamashita, and M. Hara. Critical amino acid residues for the specific binding of the ti-recognizing recombinant ferritin with oxide surfaces of titanium and silicon. *Langmuir*, 25:10901–10906, 2009.

[76] T. Hayashi, K.-I. Sano, K. Shiba, Y. Kumashiro, K. Iwahori, I. Yamashita, and M. Hara. Mechanism underlying specificity of proteins targeting inorganic materials. *Nano Lett.*, 6:515–519, 2006.

[77] M. A. Henderson. An hreels and tpd study of water on tio2(ll0): The extent of molecular versus dissociative adsorption. *Surf. Sci.*, 355:151–166, 1996.

[78] M. A. Henderson. Structural sensitivity in the dissociation of water on tio2 single-crystal surfaces. *Langmuir*, 12:5093–5098, 1996.

[79] V. V. Hoang. Structural properties of simulated liquid and amorphous TiO_2. *Phys. Stat. Sol. B*, 244(4):1280–1287, 2007.

[80] P. Hohenberg and W. Kohn. Inhomogeneous electron gas. *Phys. Rev.*, 136(3B):B864–B871, Nov 1964.

[81] W. G. Hoover. Canonical dynamics: Equilibrium phase-space distributions. *Phys. Rev. A*, 31:1695–1697, 1985.

[82] D. Horinek, A. Serr, M. Geisler, T. Pirzer, U. Slotta, S. Q. Lud, J. A. Garrido, T. Scheibel, T. Hugel, and R. R. Netz. Peptide adsorption on a hydrophobic surface results from an interplay of solvation, surface, and intrapeptide forces. *Proc. Natl. Acad. Sci. USA*, 105:284–2847, 2008.

[83] C. J. Howard, T. M. Sabine, and F. Dickson. Structural and thermal parameters for rutile and anatase. *Acta Crystallogr.,Sect. B: Struct. Sci.*, 47:462, 1991.

[84] A. Hozumi, H. Sugimura, Y. Yokogawa, T. Kameyama, and O. Takai. ζ-potentials of planar silicon plates covered with alkyl- and fluoroalkylsilane self-assembled monolayers. *Coll. Surf. A: Physicochem. Eng. Aspects*, 2001:257–261, 182.

[85] X. Huang, M. Hagen, B. Kim, R. A. Friesner, R. Zhou, and B. J. Berne. Replica exchange with solute tempering: Efficiency in large scale systems. *J. Phys. Chem. B*, 111:5405–5410, 2007.

[86] Y. K. Hwang, K. R. Patil, H.-K. Kim, S. D. Sathaye, J.-S. Hwang, S.-E. Park, and J.-S. Chang. Photoinduced superhydrophilicity in tio2 thin films modified with wo3. *Bull. Korean Chem. Soc.*, 26:1515–1519, 2005.

[87] D. G. Isaak, J. D. Cares, H. Cynn, and E. Hake. Elasticity of TiO_2 rutile to 1800k. *Phys. Chem. Min.*, 26(1):31–43, 1998.

[88] B. Isralewitz, M. Gao, and K. Schulten. Steered molecular dynamics and mechanical functions of proteins. *Curr. Opin. Struct. Biol*, 11:224–230, 2001.

[89] W. L. Jorgensen, J. Chandrasekhar, J. D. Madura, R. W. Impey, and M. L. Klein. Comparison of simple potential functions for simulating liquid water. *J. Chem. Phys.*, 79:926–935, 1983.

[90] W. L. Jorgensen and J. Tirado-Rives. The opls force field for proteins. energy minimizations for crystals of cyclic peptides and crambin. *J. Am. Chem. Soc.*, 110:1657–1666, 1988.

[91] B. Kasemo and J. Lausmaa. Material-tissue interfaces: The role of surface properties and processes. *Environ. Health Perspect.*, 102:41–45, 1994.

[92] X. Khoo, P. Hamilton, G. A. O'Toole, B. D. Snyder, D. J. Kenan, and M. W. Grinstaff. Directed assembly of pegylated-peptide coatings for infection-resistant titanium metal. *J. Am. Chem. Soc.*, 131:10992–10997, 2009.

[93] W. Kohn and L. J. Sham. Self-consistent equations including exchange and correlation effects. *Phys. Rev.*, 140(4A):A1133–A1138, Nov 1965.

[94] D. B. Kokh, S. Corni, P. J. Winn, M. Höfling, K. E. Gottschalk, and R. C. Wade. Prometcs: An atomistic force field for modeling proteinmetal surface interactions in a continuum aqueous solvent. *J. Chem. Theory Comput.*, 6:1753–1768, 2010.

[95] K. Kokubun, K. Kashiwagi, M. Yoshinari, T. Inoue, and K. Shiba. Motif-programmed artificial extracellular matrix. *Biomacromol.*, 9:3098–3105, 2008.

[96] V. N. Koparde and P. T. Cummings. Phase transformations during sintering of titania nanoparticles. *ACS Nano*, 2:1620–1624, 2008.

[97] S. Köppen and W. Langel. Simulation of the interface of (100) rutile with aqueous ionic solution. *Surf. Sci.*, 600:2040–2050, 2006.

[98] S. Köppen and W. Langel. Simulation of adhesion forces and energies of peptides on titanium dioxide surfaces. *Langmuir*, 26:15248–15256, 2010.

[99] M. Kosmulski. The significance of the difference in the point of zero charge between rutile and anatase. *Adv. Coll. Interf. Sci.*, 99:255–264, 2002.

[100] K. Kubiak-Ossowska and P. A. Mulheran. Mechanism of hen egg white lysozyme adsorption on a charged solid surface. *Langmuir*, 26:15954–15965, 2010.

[101] S. Kumar, D. Bouzida, R. H. Swendsen, P. A. Kollman, and J. M. Rosenberg. The weighted histogram analysis method for free-energy calculations on biomolecules. i. the method. *J. Comp. Chem.*, 13:1011–1021, 1992.

[102] F. Labat, P. Baranek, C. Domain, C. Minot, and C. Adamo. Density functional theory analysis of the structural and electronic properties of tio2 rutile and anatase polytypes: Performances of different exchange-correlation functionals. *J. Chem. Phys.*, 126:154703–154714, 2007.

[103] A. Laio and F. L. Gervasio. Metadynamics: a method to simulate rare events and reconstruct the free energy in biophysics, chemistry and material science. *Rep. Prog. Phys.*, 71:126601–126622, 2008.

[104] W. Langel. Car-parrinello simulation of h2o dissociation on rutile. *Surf. Sci.*, 496:141–150, 2002.

[105] I. Langmuir. The constitution and fundamental properties of solids and liquids. part i. solids. *J. Am. Chem. Soc.*, 38:2221–2295, 1916.

[106] J. Lausmaa, P. Loefgren, and B. Kasemo. Adsorption and coadsorption of water and glycine on tio2. *J. Biomed. Mater. Res.*, 44:227–242, 1999.

[107] M. Lazzeri and A. Selloni. Stress-driven reconstruction of an oxide surface: The anatase tio2(001)-(1 x 4) surface. *Phys. Rev. Lett.*, 87:266105–266108, 2001.

[108] H. Lee, N. F. Scherer, and P. B. Messersmith. Single-molecule mechanics of mussel adhesion. *Proc. Natl. Acad. Sci.*, 103:12999–13003, 2006.

[109] I. Lee and R. Marchant. Force measurements on the molecular interactions between ligand (rgd) and human platelet aiib b3 receptor system. *Surf. Sci.*, 491:433–443, 2001.

[110] S.-C. Li, J.-G. Wang, P. Jacobson, X.-Q. Gong, A. Selloni, and U. Diebold. Correlation between bonding geometry and band gap states at organic-inorganic interfaces: Catechol on rutile tio2(110). *J. Am. Chem. Soc.*, 131:980–984, 2009.

[111] X. Li and R. A. Latour. The temperature intervals with global exchange of replicas empirical accelerated sampling method: Parameter sensitivity and extension to a complex molecular system. *J. Comput. Chem.*, 32:1091–1100, 2010.

[112] Y.-C. Liang, D.-P. Song, M.-J. Chen, and Q.-S. Bai. Adsorption mechanism of arg-gly-asp on rutile tio2 (110) surface in aqueous solution. *J. Vac. Sci. Technol. B*, 27:1548–1554, 2009.

[113] P. J. D. Lindan and C. Zhang. Exothermic water dissociation on the rutile tio2(110) surface. *Phys. Rev. B*, 72:075439–075445, 2005.

[114] P. Liu, B. Kim, R. A. Friesner, and B. J. Berne. Replica exchange with solute tempering: A method for sampling biological systems in explicit water. *Proc. Natl. Acad. Sci. USA*, 102:13749–13754, 2005.

[115] S.-Y. Liu, F.-H. Wang, Yun-Song-Zhou, and J.-X. Shang. Ab initio study of oxygen adsorption on the ti(0001) surface. *J. Phys.: Cond. Mat.*, 19:226004–226015, 2007.

[116] A. MacKerel Jr., C. Brooks III, L. Nilsson, B. Roux, Y. Won, and M. Karplus. *CHARMM: The Energy Function and Its Parameterization with an Overview of the Program*, volume 1 of *The Encyclopedia of Computational Chemistry*, pages 271–277. John Wiley & Sons: Chichester, 1998.

[117] R. M. Martin. *Electronic Structure: Basic Theory and Practical Methods*. Cambridge University Press, Cambridge, 2004.

[118] D. Marx and J. Hutter. *Ab Initio Molecular Dynamics*. Cambridge University Press, Cambridge, 2009.

[119] M. Matsui and M. Akaogi. Molecular dynamics simulation of the structural and physical properties of the four polymorphs of TiO_2. *Mol. Sim.*, 6:239–244, 1991.

[120] Y. Matsushima, T. Yamazaki, K. Maeda, T. Noma, and T. Suzuki. Plasma oxidation of a titanium electrode in dc-plasma above the water surface. *J. Am. Ceram. Soc.*, 89:799, 2006.

[121] E. McCafferty, J. P. Wightman, and T. F. Cromer. Surface properties of hydroxyl groups in the air-formed oxide film on titanium. *J. Electrochem. Soc.*, 146:2849–2852, 1999.

[122] E. P. Meagher and G. A. Lager. Polyhedral thermal expansion in the tio 2 polymorphs; refinement of the crystal structures of rutile and brookite at high temperature. *Can. Mineral.*, 17:77–85, 1979.

[123] D. Mergel, D. Buschendorf, S. Eggert, R. Grammes, and B. Samset. Density and refractive index of TiO_2 films prepared by reactive evaporation. *Thin Solid Films*, 371:218–224, 2000.

[124] F. A. Momany. Determination of partial atomnic charges from ab initio molecular electrostatic potentials. application to formamide, methanol, and formic acid. *J. Phys. Chem.*, 82:592–601, 1978.

[125] H. J. Monkhorst and J. D. Pack. Special points for brillouin-zone integrations. *Phys. Rev. B*, 13(12):5188–5192, Jun 1976.

[126] S. Monti. Molecular dynamics simulations of collagen-like peptide adsorption on titanium-based material surfaces. *J. Phys. Chem. C*, 111:6086–6094, 2007.

[127] S. Monti and T. R. Walsh. Free energy calculations of the adsorption of amino acid analogues at the aqueous titania interface. *J. Phys. Chem. C*, 114:22197–22206, 2010.

[128] T. Morimoto, M. Nagao, and T. Omori. Heat of immersion of titanium dioxide in water. i. the effect of the hydration treatment of titanium dioxide. *Bull. Chem. Soc. Jpn.*, 42:943–946, 1969.

[129] W. J. Mortier, K. V. Genechten, and J. Gasteiger. Electronegativity equalization: Application and parametrization. *J. Am. Chem. Soc.*, 107:829–835, 1985.

[130] R. S. Mulliken. Electronic population analysis on lcao-mo molecular wave functions. i. *J. Chem. Phys.*, 23:1833–1840, 1955.

[131] J. Neugebauer and M. Scheffler. Adsorbate-substrate and adsorbate-adsorbate interactions of na and k adlayers on al(111). *Phys. Rev. B*, 46:16067–16080, 1992.

[132] R. Notman and T. R. Walsh. Molecular dynamics studies of the interactions of water and amino acid analogues with quartz surfaces. *Langmuir*, 25:1638–1644, 2009.

[133] C. P. O'Brien, S. J. Stuart, D. A. Bruce, and R. A. Latour. Modeling of peptide adsorption interactions with a poly(lactic acid) surface. *Langmuir*, 24:14115–14124, 2008.

[134] F. Ortmann, W. G. Schmidt, and F. Bechstedt. Attracted by long-range electron correlation: Adenine on graphite. *Phys. Rev. Lett.*, 95(18):186101–186104, 2005.

[135] C. Oviedo. Oxidation kinetics of pure titanium at low pressure. *J. Phys.: Cond. Mat.*, 5:153–154, 1993.

[136] R. G. Parr and W. Yang. *Density-Functional Theory of Atoms and Molecules*. Oxford University Press, New York, 1989.

[137] J. P. Perdew and Y. Wang. Accurate and simple analytic representation of the electron-gas correlation energy. *Phys. Rev. B*, 45(23):13244–13249, Jun 1992.

[138] S. J. Plimpton. Fast parallel algorithms for short-range molecular dynamics. *J. Comp. Phys.*, 117:1–19, 1995.

[139] M. Předota, A. V. Bandura, P. T. Cummings, J. D. K. D. J. Wesolowski, A. A. Chialvo, and M. L. Machesky. Electric double layer at the rutile (110) surface. 1. structure of surfaces and interfacial water from molecular dynamics by use of ab initio potentials. *J. Phys. Chem. B*, 108:12049–12060, 2004.

[140] Y. Qin and K. A. Fichthorn. Molecular-dynamics simulation of forces between nanoparticles in a lennard-jones liquid. *J. Chem. Phys.*, 119:9745–9754, 2003.

[141] S. Rammelt, T. Illert, S. Bierbaum, D. Scharnweber, H. Zwipp, and W. Schneiders. Coating of titanium implants with collagen, rgd peptide and chondroitin sulfate. *Biomaterials*, 27:5561–5571, 2006.

[142] J. E. Raynor, T. A. Petrie, K. P. Fears, R. A. Latour, A. J. García, and D. M. Collard. Saccharide polymer brushes to control protein and cell adhesion to titanium. *Biomacromol.*, 10(4):748–755, 2009.

[143] K. Rezwan, A. R. Studart, J. Vrs, and L. J. Gauckler. Change of potential of biocompatible colloidal oxide particles upon adsorption of bovine serum albumin and lysozyme. *The Journal of Physical Chemistry B*, 109(30):14469–14474, 2005.

[144] E. Ruoslahti and M. D. Pierschbacher. New perspectives in cell adhesion: Rgd and integrins. *Science*, 238:491–497, 1987.

[145] S. Salameh, J. Schneider, L. Colombi Ciacchi, and L. Mädler. 2011. In preparation.

[146] K.-I. Sano, H. Sasaki, and K. Shiba. Specificity and biomineralization activities of ti-binding peptide-1 (tbp-1). *Langmuir*, 21:3090–3095, 2005.

[147] K.-I. Sano and K. Shiba. A hexapeptide motif that electrostatically binds to the surface of titanium. *J. Am. Chem. Soc.*, 125:14234–14235, 2003.

[148] M. Sarikaya, C. Tamerler, A. K.-Y. Jen, K. Schulten, and F. Baneyx. Molecular biomimetics: Nanotechnology through biology. *Nature Mater.*, 2:577–585, 2003.

[149] J. Schneider and L. Colombi Ciacchi. First principles and classical modeling of the oxidized titanium (0001) surface. *Surf. Sci.*, 604:1105–1115, 2010.

[150] J. Schneider and L. Colombi Ciacchi. A classical potential to model the adsorption of biological molecules on oxidized titanium surface. *J. Chem. Theory Comp.*, 7:473–484, 2011.

[151] E. Schrödinger. Quantisierung als eigenwertproblem. *Ann. Phys.*, 79:361–376, 1926.

[152] K. Shiba. Exploitation of peptide motif sequences and their use in nanobiotechnology. *Curr. Op. Biotech.*, 21:412–425, 2010.

[153] U. C. Singh and P. A. Kollman. An approach to computing electrostatic charges for molecules. *J. Comp. Chem.*, 5:129–145, 1984.

[154] A. A. Skelton, T. Liang, and T. R. Walsh. Interplay of sequence, conformation, and binding at the peptide-titania interface as mediated by water. *ACS Appl. Mat. Interf.*, 1:1482–1491, 2009.

[155] A. A. Skelton and T. R. Walsh. Interaction of liquid water with the rutile tio_2 (110) surface. *Mol. Sim.*, 33:379–389, 2007.

[156] J. M. Slocik, A. O. Govorov, and R. R. Naik. Plasmonic circular dichroism of peptide-functionalized gold nanoparticles. *Nano Letters*, 11(2):701–705, 2011.

[157] D.-P. Song, M.-J. Chen, Y.-C. Liang, Q.-S. Bai, J.-X. Chen, and X.-F. Zheng. Adsorption of tripeptide rgd on rutile tio2 nanotopography surface in aqueous solution. *Acta Biomat.*, 6:684–694, 2010.

[158] S. Steckbeck and L. Colombi Ciacchi, 2011. In preparation.

[159] M. Stengel and A. D. Vita. First-principles molecular dynamics of metals: A lagrangian formulation. *Phys. Rev. B*, 62:15283–15286, 2000.

[160] Y. Sugita and Y. Okamoto. Replica-exchange molecular dynamics method for protein folding. *Chemical Physics Letters*, 314(1-2):141 – 151, 1999.

[161] C. Sun, L. Liu, A. Selloni, G. Q. Lu, and S. C. Smith. Titania-water interactions: a review of theoretical studies. *J. Mater. Chem.*, 20:10319–10334, 2010.

[162] V. Swamy and J. D. Gale. Transferable variable-charge interatomic potential for atomistic simulation of titanium oxides. *Phys. Rev. B*, 62:5406–5412, 2000.

[163] W. C. Swope, H. C. Andersen, P. H. Berens, and K. R. Wilson. A computer simulation method for the calculation of equilibrium constants for the formation of physical clusters of molecules: application to small water clusters. *J. Chem. Phys.*, 76:637–649, 1982.

[164] T. F. Tadros and J. Lyklema. Adsorption of potential-determining ions at the silica-aqueous electrolyte interfaceand the role of some cations. *J. Electroanal. Chem.*, 17:267–275, 1968.

[165] K. Takahashi and S. Fukuzaki. Cleanability of titanium and stainless steel particles in relation to surface charge aspects. *Biocontr. Sci.*, 13:9–16, 2008.

[166] Y. Takakuwa, S. Ishidzuka, A.Yoshigoe, Y. Teraoka, Y. Minzuno, H. Tomda, and T. Homma. Time-resolved photoelectron spectroscopy of oxidation on the ti (0001) surface. *Nuc. Instr. Meth. Phys. Res. B*, 200:376–381, 2003.

[167] Y. Takakuwa, S. Ishidzuka, A.Yoshigoe, Y. Teraoka, Y. Yamamauchi, Y. Minzuno, H. Tonda, and T. Homma. Real-time monitoring of oxidation on the ti (0001) surface by synchrotron radiation photoelectron spectroscopy and rheed-aes. *Appl. Surf. Sci.*, 216:395–401, 2003.

[168] S. Takemoto, M. Hattori, M. Yoshinari, E. Kawada, and Y. Oda. Corrosion behavior and surface characterization of titanium in solution containing fluoride and albumin. *Biomaterials*, 26:829–837, 2005.

[169] C. Tamerler, E. E. Oren, M. Duman, Eswaran, Venkatasubramanian, and M. Sarikaya. Adsorption kinetics of an engineered gold binding peptide by surface plasmon resonance spectroscopy and a quartz crystal microbalance. *Langmuir*, 22:7712–7718, 2006.

[170] M. I. Temkin. *Kinet. Catal.*, 8:1005, 1967.

[171] W. Y. Teoh, R. Amal, L. Mdler, and S. E. Pratsinis. Flame sprayed visible light-active fe-tio2 for photomineralisation of oxalic acid. *Catalysis Today*, 120(2):203 – 213, 2007.

[172] W. Y. Teoh, L. Mdler, and R. Amal. Inter-relationship between pt oxidation states on tio2 and the photocatalytic mineralisation of organic matters. *Journal of Catalysis*, 251(2):271 – 280, 2007.

[173] T. Terakawa, T. Kameda, and S. Takada. On easy implementation of a variant of the replica exchange with solute tempering in GROMACS. *J. Comput. Chem.*, 32:1228–1234, 2010.

[174] R. Tétot, A. Hallil, J. Creuze, and I. Braems. Tight-binding variable-charge model for insulating oxides: Application to tio2 and zro2 polymorphs. *Europhys. Lett.*, 83:40001–40005, 2008.

[175] B. S. Thomas, N. A. Marks, and B. D. Begg. Empirical variable-charge models for titanium oxides: A study in transferability. *Phys. Rev. B*, 60:144122–144129, 2004.

[176] I. T. Todorov and W. Smith. DL_POLY_3: The CCP5 national uk code for molecular-dynamics simulations. *Phil. Trans. R. Soc. A*, 362:1835–1852, 2004.

[177] L. Treccani, M. Maiwald, V. Zllmer, M. Busse, G. Grathwohl, and K. Rezwan. Antibacterial and abrasion-resistant alumina micropatterns. *Advanced Engineering Materials*, 11(7):B61–B66, 2009.

[178] D. Trzesniak, A.-P. E. Kunz, and W. F. van Gunsteren. A comparison of methods to compute the potential of mean force. *Chem. Phys. Chem.*, 8:162–169, 2007.

[179] W. F. van Gunsteren and H. J. C. Berendsen. Algorithms for brownian dynamics. *Mol. Phys.*, 45:637–647, 1982.

[180] J. VandeVondele and A. D. Vita. First-principles molecular dynamics of metallic systems. *Phys. Rev. B*, 60:13241–13244, 1999.

[181] I. Vaquila, M. C. G. Passeggi, and J. Ferron. Temperature effects in the early stages of titanium oxidation. *Appl. Surf. Sci.*, 93:247–253, 1996.

[182] L. Verlet. Computer 'experiments' on classical fluids. i. thermodynamical properties of lennard-jones molecules. *Phys. Rev.*, 159:1685–1699, 1967.

[183] A. D. Vita, A. Canning, G. Galli, F. Gygi, F. Mauri, and R. Car. Quantum molecular dynamics on massively parallel computers. *EPFL Supercomput. Rev.*, 6:22, 1994.

[184] A. Vittadini, M. Casarin, and A. Selloni. Chemistry of and on tio2-anatase surfaces by dft calculations: a partial review. *Theor. Chem. Acc.*, 117:663, 2007.

[185] C. Wagner. Beitrag zur theorie des anlaufvorgangs. *Z. Phys. Chem.*, B21:25, 1933.

[186] J. .Wang, R. M. Wolf, J. W. Caldwell, P. A. Kollman, and D. A. Case. Development and testing of a general amber force field. *J. Comp. Chem.*, 25:1157–1174, 2004.

[187] J. Weeks, D. Chandler, and H. Andersen. Role of repulsive forces in determining the equilibrium structure of simple liquids. *J. Chem. Phys.*, 54:5237–5247, 1971.

[188] Y. Wei and R. A. Latour. Determination of the adsorption free energy for peptidesurface interactions by spr spectroscopy. *Langmuir*, 24(13):6721–6729, 2008.

[189] Y. Wei and R. A. Latour. Benchmark experimental data set and assessment of adsorption free energy for peptide-surface interactions. *Langmuir*, 25:5637–5646, 2009.

[190] S. Wendt, J. Matthiesen, R. Schaub, E. K. Vestergaard, E. Lægsgaard, F. Besenbacher, and B. Hammer. Formation and splitting of paired hydroxyl groups on reduced tio_2(110). *Phys. Rev. Lett.*, 96(6):066107–066110, Feb 2006.

[191] R. J. Woods, M. Khalil, W. Pell, S. H. Moffat, and V. H. Smith Jr. Derivation of net atomic charges from molecular electrostatic potentials. *J. Comp. Chem.*, 11:297–310, 1990.

[192] C. Wu, M. Chen, C. Guo, X. Zhao, and C. Yuan. Peptide-tio2 interaction in aqueous solution: Conformational dynamics of rgd using different water models. *J. Phys. Chem. B*, 114:4692–4701, 2010.

[193] S.-J. Xiao, M. Textor, and N. D. Spencer. Covalent attachment of cell-adhesive, (arg-gly-asp)-containing peptides to titanium surfaces. *Langmuir*, 14:5507–5516, 2998.

[194] H. Yamamoto, Y. Shibata, and T. Miyazaki. Anode glow discharge plasma treatment of titanium plates facilitates adsorption of extracellular matrix proteins to the plates. *J. Dent. Res.*, 84:668–671, 2005.

[195] I. Yamashita, H. Kirimura, M. Okuda, K. Nishio, K.-I. Sano, K. Shiba, T. Hayashi, M. Hara, and Y. Mishima. Selective nanoscale positioning of ferritin and nanoparticles by means of target-specific peptides. *Small*, 2:1148–1152, 2006.

[196] W. Yuan, J. Ji, J. Fu, and J. Shen. A facile method to construct hybrid multilayered films as a strong and multifunctional antibacterial coating. *Journal of Biomedical Materials Research Part B: Applied Biomaterials*, 85B(2):556–563, 2008.

[197] J. Zimmermann and L. Colombi Ciaccchi. Origin of the selective cr oxidation in cocr alloy surfaces. *J. Chem. Phys. Lett.*, 1:2343–2348, 2010.

[198] J. Zimmermann, M. W. Finnis, and L. Colombi Ciacchi. Vacancy segregation in the initial oxidation stages of the tin(100) surface. *J. Chem. Phys.*, 130:134714–134725, 2009.

Erklärung

Hiermit erkläre ich, dass ich

- die Arbeit ohne unerlaubte fremde Hilfe angefertigt habe;
- keine anderen als die von mir angefertigten Quellen und Hilfsmittel benutzt habe;
- die den benutzten Werken wörtlich oder inhaltlich entnommenen Stellen als solche kenntlich gemacht habe.

Bremen, den 14. September 2011

Julian Schneider